UC Berkeley

UC Berkeley Electronic Theses and Dissertations

Title

Atmospheric Rivers: Genesis, Representation, and Structure

Permalink

https://escholarship.org/uc/item/25z985cj

Author

Kim, Sol

Publication Date

2023

Peer reviewed|Thesis/dissertation

Atmospheric Rivers: Genesis, Representation, and Structure

by

Sol Kim

A dissertation submitted in partial satisfaction of the

requirements for the degree of

Doctor of Philosophy

in

Geography

in the

Graduate Division

of the

University of California, Berkeley

Committee in charge:

Professor John C. H. Chiang, Chair
Doctor Karthik Kashinath
Professor Inez Fung
Associate Professor Laurel G. Larsen

Summer 2023

Atmospheric Rivers: Genesis, Representation, and Structure

Abstract

Atmospheric Rivers: Genesis, Representation, and Structure

by

Sol Kim

Doctor of Philosophy in Geography

University of California, Berkeley

Professor John C. H. Chiang, Chair

The goal of this dissertation is to advance atmospheric river (AR) research in 3 distinct areas: (i) genesis of ARs, (ii) model representation of ARs, and (iii) the impact of AR core structure on landfalling precipitation.

In Chapter 2, the range of synoptic patterns that north Pacific landfalling ARs form under are objectively identified using genesis day 500 hPa geopotential height anomalies in a self-organizing map (SOM). The SOM arranges the synoptic patterns to differentiate between two groups of climate modes - the first group with ENSO (El Niño Southern Oscillation), PDO (Pacific Decadal Oscillation), PNA (Pacific North American) and NP (North Pacific index) and the second group with AO (Arctic Oscillation), EPO (East Pacific Oscillation), and WPO (West Pacific Oscillation). These two groups have their positive and negative modes organized in opposite corners of the SOM. The ARs produced in each of the synoptic patterns have distinct lifecycle characteristics (such as genesis and landfall location, duration, velocity, meridional/zonal movement) and precipitation impacts (magnitude and spatial distribution). The conditions that favor AR trajectories closer to the tropics tend to produce higher amounts of precipitation. The large-scale circulation associated with AR genesis shows a close relationship between the genesis location and the location and intensity of the upper level jet in the west/central pacific as well as anomalous, low level southwesterly winds in the east pacific.

Chapter 3 focuses on evaluating The Energy Exascale Earth System Model (E3SM) version v1.0 for its ability to represent ARs, which play significant roles in water vapor transport and precipitation. The E3SM Project is an ongoing, state-of-the-science Earth system modeling, simulation, and prediction project developed by the U.S. Department of Energy (DOE). With an emphasis on supporting DOE's energy mission, understanding and quantifying how well the model simulates water cycle processes is of particular importance. The characteristics and precipitation associated with global ARs in E3SM at standard resolution (1° x 1°) are compared to the Modern-Era Retrospective analysis for Research and Applications, Version

2 (MERRA2). Global patterns of AR frequencies in E3SM show high degrees of correlation ($>=0.97$) with MERRA2 and low mean absolute errors (<1 %) annually, seasonally, and across different ensemble members. However, some large-scale condition biases exist leading to AR biases - most significant of which are: the double-ITCZ, a stronger and/or equatorward shifted subtropical jet during boreal and austral winter, and enhanced northern hemisphere westerlies during summer. By comparing atmosphere-only and fully-coupled simulations, we attribute the sources of the biases to the atmospheric component or to a coupling response. Using relationships revealed in Dong et al., 2021, we provide evidence showing the stronger north Pacific jet in winter and enhanced northern hemisphere westerlies during summer associated with E3SM's double-ITCZ and related weaker AMOC, respectively, are significant sources of the AR biases found in the coupled simulations.

In Chapter 4, we explore how the vertical structure of ARs - specifically the core (the area of the strongest moisture transport) of an AR - can influence precipitation on the west coast states of the U.S.. The relationship between moisture transport intensity and precipitation impacts for ARs is currently well established. While vertically integrated moisture transport (IVT) is the most significant predictor in the intensity of precipitation for landfalling ARs, other aspects remain understudied. In this chapter, we find that the height of the AR core - defined as the height of the moisture flux maximum - can cause significant differences in precipitation even when controlling for IVT strength. Depending on the AR core height and the landfall terrain height, precipitation influences are varied. We find ARs with low (1000 - 950 hPa) core heights have enhanced precipitation over all terrain heights, ARs with medium heights (950 - 900 hPa) generally have reduced precipitation but particularly so over elevated terrain, and high (< 900 hPa) core heights deliver more precipitation to elevated terrain and into the interior of the U.S.. Looking at trends over the last 4 decades, the AR core height means are shifting to slightly higher altitudes with greater variance - i.e. low and high AR core heights will become more frequent while medium core heights become less frequent. In order to carry out the analysis on the AR core, we developed a novel algorithm used to identify AR sectors (core, cold sector, and warm sector) using IVT and geometric constraints. We compare characteristics of these detected sectors in 41 years of reanalysis data to recent dropsonde observations and find agreement in key characteristics for all sectors although there are lower moisture flux and windspeed values in the cold and warm sector due to threshold differences and reanalysis biases.

To my family

Contents

List of Figures

List of Tables

Acknowledgments

First and foremost, a sincere and heartfelt thanks to my advisor John Chiang. I consider myself so fortunate and grateful to have had such a kind, supportive, patient, and encouraging advisor throughout my challenging and formative years as a scholar. Amidst my own ebbs and flows, academically and in life, I have always felt that he was in my corner ready to offer guidance and honesty without judgement. Because of this, I have had the courage to see this dissertation through and pursue my own novel ideas throughout my graduate studies. John has continuously pushed me to craft compelling stories, address meaningful issues, and to look in areas where others might not with my science. Above all, I thank him for being a tremendous role model to me - as a scholar and a human. His ability to take care of others quietly, in the background, without fanfare is the quality I most admire and appreciate. It certainly does go unnoticed - I, and countless others, feel so much gratitude towards John.

A huge thanks to my dissertation committee of Karthik Kashinath, Inez Fung, and Laurel Larsen. Karthik took me under his wing when I approached him at a Deep Learning workshop early in my program and he has so graciously involved me in his cutting-edge and always exciting science projects. Our conversations surrounding our roles as climate scientists and more broadly as inhabitants of Earth have informed and shaped my values throughout my time as a graduate student and now as I begin my career. Despite being a giant in the field of climate science, Inez has taught me to always be curious and to never shy away from asking questions. After she started her role on the President's Council of Advisors on Science and Technology, she challenged me to always ask myself and my work, "How does this serve the people?". Laurel graciously and earnestly joined my committee even though our interactions were limited prior to her joining - I thank her for taking a chance and for her support throughout the dissertation writing. I have been continuously inspired by Laurel's willingness to take on new challenges on top of her role as a professor - whether it be a Fulbright year in Finland or taking a position as a lead scientist in with the Delta Stewardship Council.

I also owe thanks to several other mentors and role models. Norman Miller and Michael Wehner encouraged me to pursue graduate studies as an undergraduate and showed me first hand what work-life balance looks like. Prabhat for taking me in for the ClimateNet project, support throughout my studies (especially during qualifying exams), and for the absolute best project management I have ever witnessed. Ruby L. Leung for being such a patient and supportive mentor during my very isolated, virtual/remote summer internship with the Pacific Northwest National Lab. Christine Lee for her continued mentorship since my time at NASA and for collaborating with me for the turbidity project in Belize. Christine Shields for her pioneering work with atmospheric rivers and her inclusive, collaborative approach to science. I really appreciated her support and encouragement for the ClimateNet project and whilst I looked for job opportunities.

I am so grateful to the entire Geography Department - from my friends and peers to the staff and faculty, I thank everyone for the collective energy to try and make each other and the department better, now and for the future. My peers helped keep me grounded

especially during the pandemic - providing me with companionship, laughter, and a reminder for self-care. Eron, Dan, Sarah, Marjorie, Ambrosia, Bobby, Clancy, Josh, and Sharad have helped me to navigate the program in various ways and answered all my technical/logistical questions. A special thanks to Wenwen and Yanlei - I really valued our honest and supportive conversations throughout good times and challenging times.

Lastly, a thank you to my friends and family for the constant and unconditional love and support. I have had moments of feeling scared, lost, insignificant, uninspired, and/or down throughout the past 6 years but have always managed to find my way because of you - thanks for believing in me and supporting me when I could not.

Chapter 1

Introduction

Atmospheric rivers (ARs) - sometimes called 'rivers in the sky' - are narrow, filamentary structures in the lower atmosphere responsible for transporting the majority of water vapor across the mid-latitudes towards the poles (Zhu and Newell, 1998). These features are critical in the global water cycle; they cover only about 10% of the Earth's circumference but transport more than 90% of the total poleward atmospheric water vapor transport in the midlatitudes. Today the term 'atmospheric river' is ubiquitous throughout the scientific community. Although ARs are a relatively recent concept, being first coined in the 1990's, they have been the subject of intense scientific activities in the past two decades owing to their importance in global and regional hydrology and due to advances in technology (e.g. satellites, reanalysis products, specialized aircraft equipment). This dissertation builds upon recent advances as opportunities to further our understanding of AR genesis, representation, and structure. Briefly described in this introduction: a background on ARs (Section 1.1), the connection between ARs and extreme precipitation/floods (Section 1.2), and recent advances (Section 1.3). The last section (Section 1.4) provides an overview of the following chapters.

1.1   Background

First, we describe the phenomena of ARs which has been difficult to define for the scientific community due to their connection to the related but distinct phenomena of tropical moisture exports and warm conveyor belts. Only in 2018, did the American Meteorological Society formally accept a definition of ARs into their glossary - around the same time this dissertation started (F. M. Ralph et al., 2018; F. M. Ralph, Dettinger, Rutz, et al., 2020a). An AR is formally defined as a "long, narrow, and transient corridor of strong horizontal water vapor transport that is typically associated with a low-level jet stream ahead of the cold front of an extratropical cyclone" (AMS, 2023). These lower tropospheric features can tap into tropical and/or extratropical moisture sources and frequently generate precipitation through orographic ascent when they encounter topography or ascent through the warm conveyor belt. ARs are considered the largest fresh water rivers on Earth - transporting, on average,

more than double the flow of the Amazon River.
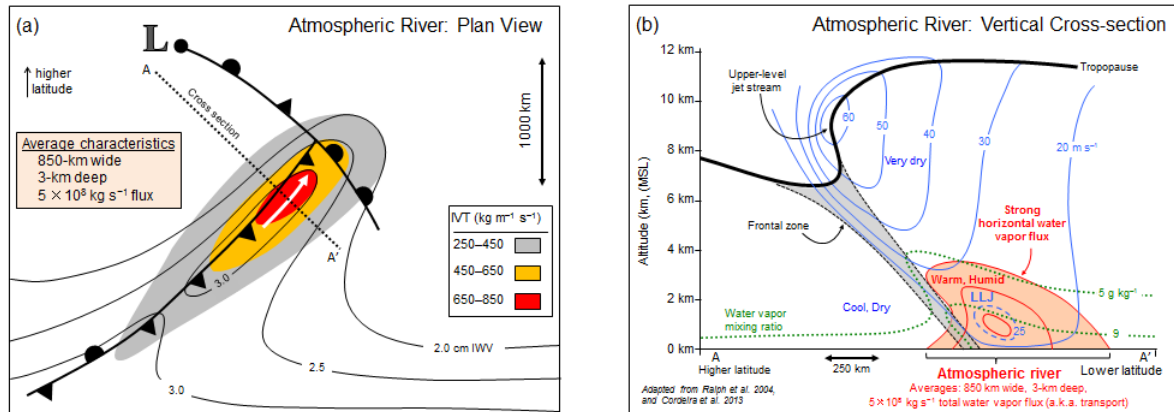
Figure 1.1: Schematic of an average midlatitude atmospheric river in a) a plan view and b) vertical cross-section. The figure comes from F. M. Ralph, Iacobellis, et al., 2017. The red area and yellow portions show areas of strong vertically integrated water vapor transport (IVT). This region represents the core of the AR.

Fig 1.1 shows in plan view and in vertical cross-section, the typical structure of ARs. The plan view allows us to see the position of ARs in relation to an extratropical cyclone fronts - the AR core is a pre-cold-frontal feature with the strongest moisture transport in the warm front. The cross-section shows where the sharp temperature gradient at the cold front encourages the development of the low-level jet and how warm, tropical/extratropical air provides the moisture. The typical strength of ARs - characterized by the vertically integrated water vapor transport (IVT) - is shown to range from 250 kg m^{-1} s^{-1} near the edges to 850 kg m^{-1} s^{-1} in the core of the AR.

1.2   Extreme precipitation and flooding

ARs and their impact on regional hydrology - namely extreme precipitation and flooding - are becoming well recognized, particularly on the west coast of the U.S. but also in other regions around the world (e.g. F. M. Ralph et al., 2006; Dettinger et al., 2011; F. M. Ralph, Iacobellis, et al., 2017). For the western U.S., ARs contribute 25-50% of the annual precipitation but are also responsible for over 90% of historical extreme precipitation events (F. Ralph and Dettinger, 2012; F. Ralph et al., 2013). When ARs make landfall on the U.S. west coast, they can yield precipitation totals comparable to landfalling hurricanes and tropical storms on the Gulf of Mexico coast (F. M. Ralph, Dettinger, et al., 2017). Strong ARs and the intense precipitation they cause have led to major floods historical floods. For example, the Russian River in California had 7 official floods events over an 8 year observation campaign and all of these were caused by significant AR events (F. M. Ralph et al., 2006).

This highlights the dual nature of ARs - on one hand, they are crucial for water resources, but on the other, they can pose serious hazards to property and lives. Understanding ARs and what affects their precipitation impacts is critical to distinguish hazardous ARs from beneficial ones.

In our warming climate, AR intensity and associated hazards are projected to increase significantly (e.g. Payne and Magnusdottir, 2015; Espinoza et al., 2018; T. A. O'Brien et al., 2021). This is due in large part to the well-understood thermodynamic response of the atmosphere - the Clausius Clapeyron relationship states that the water vapor content of saturated air increases exponentially with temperature (Payne et al., 2020). A recent study found that for each degree Celsius of warming from present conditions, we can expect annual average flood damages to increase by ∼\$1 billion for the western U.S. (Rhoades et al., 2021). We are already experiencing the growing intensities and hazards in our current climate with studies suggesting ARs are already becoming more hazardous. An attribution study on the two ARs that caused the Oroville Dam crises in 2017 found that present-day global warming was responsible for precipitation increases of 11% and 15% respectively compared to the same events in pre-industrial conditions (Michaelis et al., 2022).

The real possibility of a 'megastorm' comprised of consecutive extreme ARs - similar to the one that caused the Great Flood of 1862 - also threatens to cause upwards of a trillion dollars in damages (Porter et al., 2011; Huang and Swain, 2022; Wing et al., 2016). Historically a storm of this magnitude occurred once every 200-years. However, recent studies have found that under our warming climate, the probability of such event increases to approximately three times per century (H. Hu et al., 2017). A report by the United States Geological Survey found California does not have adequate infrastructure and flood-protection systems to handle the flooding from this event highlighting a need to update the state's disaster resilience and integrate more climate-aware strategies.

1.3 Recent Advances

In the first textbook dedicated to ARs, two significant uncertainties were identified that limit our current ability to forecast ARs and their precipitation beyond a few days - i) the strength and location of upstream low- and upper-level jets and ii) by where the nose of the moisture transport of ARs intersect topography (F. M. Ralph, Dettinger, et al., 2017). However, recent advances in AR research and observations have opened opportunities to gain further understanding in these areas. This dissertation utilizes recently developed tracking and identification algorithms, state-of-the-science climate models, and new observations from aerial campaigns to help address current uncertainties.

The work in Chapter 2 is possible due to the Atmospheric River Tracking Method Intercomparison Project (ARTMIP) which began in 2017. Due to growing interest in ARs, numerous methods have been developed to identify and track ARs. The goal of ARTMIP is to understand the differences and quantify uncertainties related to using the numerous tracking methods (Shields et al., 2018b). Detection algorithms range from simple identifica-

tion with IVT to newer machine learning techniques (Kashinath et al., 2021). One method developed in 2019 by Gonzales et al., 2019 was novel for introducing back-tracking of individual landfalling ARs so that an AR could be tracked from genesis to termination. Chapter 2 utilizes this method to gain understanding of AR genesis conditions at a synoptic scale.
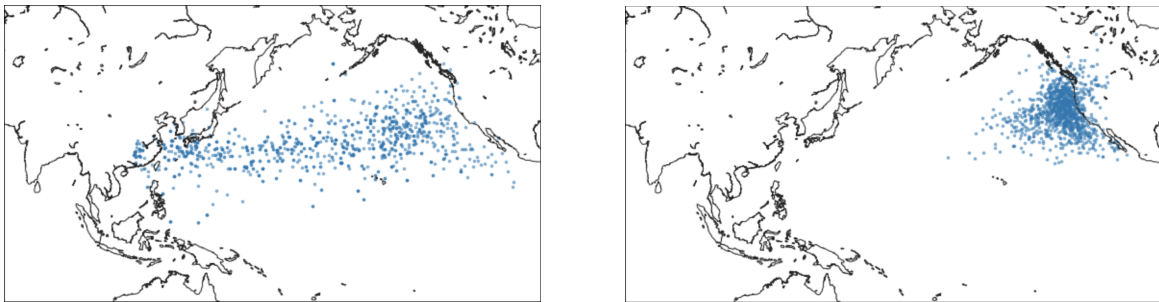
Figure 1.2: Locations of genesis and landfalls from the back-tracking algorithm used in Gonzales et al., 2019. The dots represent the IVT-weighted centroid of each AR.

Chapter 3 utilizes and evaluates a newly developed U.S. Department of Energy (DOE) climate model (the Energy Exascale Earth System Model - or E3SM) specifically for AR representation. This next generation model combines the latest in earth system modeling and exascale computing to address pressing DOE science questions - many of which require accurate representations of ARs. For example, it is of critical importance for the DOE to have projections of water availability, storms and heavy precipitation, and coastal flooding. However, before a model is trusted to make projections of the future, it must be evaluated to accurately represent our current climate accurately. This chapter aims to give researchers a comprehensive evaluation of ARs in E3SM and where biases may be present in order reduce uncertainties and to enable more AR research on this new model.

Observations of ARs first began in the late 1990s and have been focused mostly on the west coast of the U.S.. Until recent aerial campaigns, dropsonde observations revealing the vertical structure of ARs has been sparse (F. M. Ralph et al., 2016; F. M. Ralph, Cannon, et al., 2020). Chapter 4 uses new observations from the CalWater and AR Recon campaigns and work by Cobb, Michaelis, et al., 2021 to better understand how the vertical structure of ARs can impact precipitation when making landfall and to expand AR algorithm capabilities to identify various AR sectors.

1.4 An overview

As discussed above, the next chapters address three distinct gaps in AR science by building upon recent advances in AR algorithms, global climate models, and observations (Section 1.3). The goal of Chapter 2 is to investigate the different synoptic conditions that ARs form under in the north Pacific and how these different genesis conditions affect the characteristics
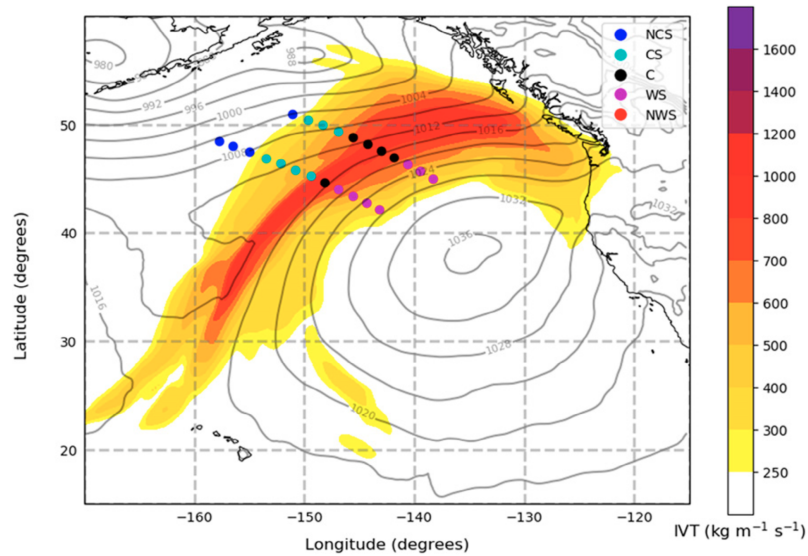
Figure 1.3: Dropsonde observations over an AR with the sectors identified. The legend refers to non-AR cold sector (NCS), cold sector (CS), core (C), warm sector (WS), and non-AR warm sector (NWS). Figure from Cobb, Michaelis, et al., 2021.

and precipitation impacts of ARs over their entire lifecycle. Chapter 3 evaluates E3SM, a newly developed, state-of-the-science global climate model for its ability to accurately represent ARs globally and identifies model biases. Chapter 4 investigates the influence of AR core vertical structure on landfalling precipitation. Chapter 5 provides a summary of the main findings and suggests opportunities for future related research.

Chapter 2

Atmospheric River Lifecycle Characteristics Shaped by Synoptic Conditions at Genesis

2.1 Introduction

Atmospheric rivers (ARs) are narrow, filamentary structures in the lower atmosphere responsible for transporting the majority of water vapor across the mid-latitudes towards the poles (Zhu and Newell, 1998). When these features make landfall, they can be associated with both beneficial and hazardous impacts (F. M. Ralph et al., 2006; F. Ralph and Dettinger, 2011;F. M. Ralph et al., 2019). In the state of California, ARs are responsible for 25-50% of the annual precipitation (Dettinger et al., 2011) while simultaneously being responsible for nearly all flood events (F. M. Ralph et al., 2006; Florsheim and Dettinger, 2015). As ARs affect a wide-range of sectors, advancing understanding of the modulating dynamics of ARs throughout their lifecycle offers immense potential socioeconomic benefits.

The large-scale dynamics of ARs are an area of active research (F. M. Ralph, Dettinger, et al., 2017; Gimeno et al., 2014). Many earlier studies on ARs and large-scale dynamics have tied AR impacts, such as total rainfall or snow water equivalent, to climate indices as opposed to direct detection and tracking of ARs (Payne and Magnusdottir, 2014; Ryoo et al., 2013). However, with the recent rise in AR detection and tracking algorithms, studies have begun examining dynamics with direct tracking (Shields et al., 2018b; Rutz et al., 2019). One well-established study by Payne and Magnusdottir, 2014 investigated the dynamics of North Pacific ARs making landfall along the west coast of North America from Alaska to Mexico. They showed a close relationship in the eastward progression of ARs and the location of the jet as well as Rossby wave breaking. Although they analyzed the lifecycle characteristics of landfalling ARs, it was focused primarily on the landfalling and pre-landfall characteristics and dynamics over the eastern half of the Pacific. Other studies examining landfall and pre-landfall characteristics have focused on relatively short periods (24-72 hrs) around landfall

(e.g. Neiman, Ralph, et al., 2013; Rutz et al., 2014; Waliser and Guan, 2017; Zhou and Kim, 2019).

In the context of large-scale dynamics, the formation of ARs and their maintenance are particularly understudied aspects in the AR lifecycle and warrants further research (Gimeno et al., 2014; Benedict et al., 2019; Zhou and Kim, 2019). There are currently only a few very recent studies that have incorporated genesis as part of their study (Payne and Magnusdottir, 2014; Gonzales et al., 2019; Sellars et al., 2017; Guan and Waliser, 2019; Zhou et al., 2018; Zhou and Kim, 2019). The three studies characterizing genesis locations (Sellars et al., 2017; Guan and Waliser, 2019; Zhou et al., 2018) are all largely consistent with a few differences; AR genesis in the north Pacific preferentially occurs near the western boundary of the Pacific basin (near ∼30N,140E). As for differences, Zhou et al., 2018 finds another area of high genesis near 150W in the subtropics related to 'Pineapple Express' events and Sellars et al., 2017 finds high genesis occurring along the Intertropical Convergence Zone (ITCZ) near the equator. These differences are likely a result of differences in detection and tracking (Shields et al., 2018b; Guan and Waliser, 2019). For example, Sellars et al., 2017 did not explicitly search for ARs but rather high IVT features and thus captured features such as tropical moisture exports which produce strong IVT signatures.

As for characteristics, Payne and Magnusdottir, 2014 found stronger ARs to have genesis in the western Pacific while weaker ARs to have genesis in the east Pacific. Zhou et al., 2018 found longer lived, farther traveling, and stronger ARs to originate in primarily in the west Pacific while shorter, weaker ARs can originate throughout the Pacific basin. Zhou and Kim, 2019 extended their analysis from this study to specifically investigate the impact of genesis location on lifecycle characteristics. The landfalling ARs in their study are separated based east and west Pacific genesis location and the AR characteristics associated with each genesis region agree with previous studies (Zhou et al., 2018; Guan and Waliser, 2019). They additionally composite geopotential height anomalies and find significant differences for the two origin locations. The Guan and Waliser, 2019 analysis was global but for north Pacific ARs, they found genesis location to impact a variety of characteristics such as lifetime, distance traveled, net displacement, speed, and direction consistent with Zhou et al., 2018. Guan and Waliser, 2019 specifically notes the processes determining AR lifecycle characteristics needs further investigation. Gonzales et al., 2019 investigated AR temperature trends by generating genesis to landfall AR tracks for individual ARs that impacts the west coast of the US. They found variable influences on AR temperatures in along-track temperatures, coastal SSTs, and background regional temperatures. This study revealed the importance of understanding AR lifetime characteristics as these translate into important hydrological impacts. We employ the AR track catalogue used in Gonzales et al., 2019 along with Guan and Waliser, 2019's catalogue for this study and look to identify what large-scale atmospheric patterns AR genesis occurs under.

Fig. 2.1 displays a composite of 500mb geopotential height anomalies occurring on the genesis day of all U.S. west coast landfalling ARs (November - February,1980-2015) from the Gonzalez AR catalogue. A deepened Aleutian low with positive height anomalies to the west over the higher latitudes of the central Pacific can be seen but the supposed signal
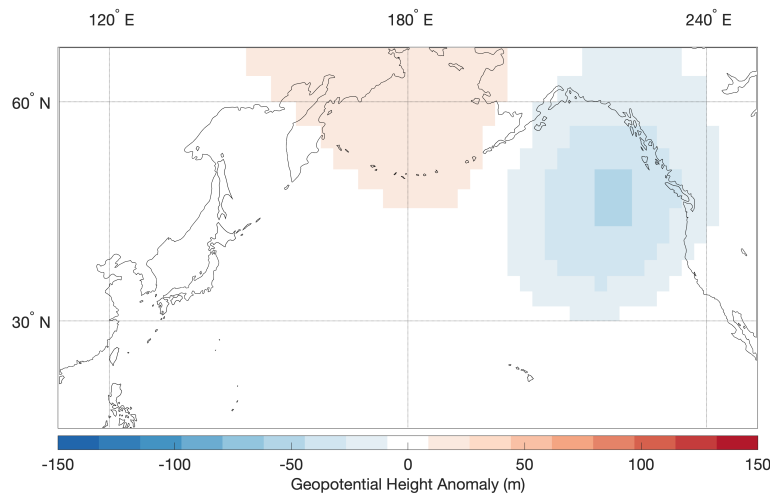
Figure 2.1: Composite of 500mb geopotential height anomalies occurring on the genesis day
of all U.S. west coast landfalling ARs (November - February,1980-2015). Fails to reveal the
range of synoptic conditions AR genesis can occur.

from this composite view does not reveal the wide range of conditions AR genesis can occur
under. Differences in large-scale circulation at and just prior to landfall have been shown to
produce varied ARs and hydrological impacts (Payne and Magnusdottir, 2014; Guirguis et
al., 2019; Neiman et al., 2008; W. Zhang and Villarini, 2018; Swales et al., 2016; Ryoo et al.,
2015; Ryoo et al., 2013; H. Hu et al., 2017). These studies show that there are significant
differences in the types of ARs that make landfall and the large-scale circulation associated
with them. This highlights a present challenge of studying the large-scale dynamics of ARs;
for example, subsetting ARs based on the strength of ARs alone or taking subsets of ARs
making landfall over a specific region/latitude can contain ARs that are very dynamically
different.

As the formation and maintenance of ARs remains understudied and given that ARs are
heterogenous in their controls, the objectives of this study are to explore: i) What is the
range of synoptic conditions that lead to AR genesis? ii) Do these large-scale circulation
patterns generate ARs with different lifecycle characteristics? and iii) How do these charac-
teristics translate into variable precipitation impacts at landfall? We investigate the range
of synoptic conditions, and their associated climate modes, that ARs form under by utilizing
self-organizing maps (SOM) (Kohonen, 1982a; Kohonen, 1982b) trained on AR genesis days
for 500 mb geopotential heights. We show how these synoptic differences affect AR lifecycle
characteristics from genesis to landfall and how these characteristics translate into precipita-
tion impacts downstream. This study follows the SOM methodology used in Guirguis et al.,
2019 to categorize distinct types of ARs by their circulation pattern at landfall for 40° N in
northern California.

The structure of this paper is as follows. In Section 2.2, the reanalysis data set, climate

indices, AR track catalogues, and the SOM method are described. The organization of the SOM map and the differentiated AR characteristics and impacts associated with the synoptic patterns are presented in Section 2.3. Discussion and conclusions are presented in Section 2.4. Finally, the Appendix is contained in Section A.

2.2 Data and Methods

2.2.1 Reanalysis Data Set

In this study, reanalysis data from MERRA-2 (Modern Era Retrospective analysis for Research and Applications, version 2) (Gelaro et al., 2017) is analyzed from 1980 to 2015 at a spatial resolution of ∼50km (0.5°x0.625°) and a daily temporal resolution. The 500mb geopotential height field is used for the SOM analysis with resolution coarsened to ∼250km (2.5°x2.5°) for the SOM training as performance is sped up without meaningful differences in the resulting SOM. The daily temporal resolution and the coarser grid are appropriate for this SOM analysis considering the synoptic scale; we are interested in investigating which large-scale patterns are conducive for AR genesis over many years. The 6 variables used in this study are: geopotential height (zg) at 500 mb, integrated vapor transport (IVT), precipitation (pr), zonal wind (U) at 250mb, potential vorticity (PV) at 200mb, and wind (U and V) at 825mb. IVT is integrated from 1000mb to 200mb. IVT was processed and obtained from the ARTMIP project (Shields et al., 2018b) and is calculated using equation 2.1:

$$IVT = -\frac{1}{g} \int_{P_b}^{P_t} (q(p)\mathbf{V}_h(p)) dp, \tag{2.1}$$

where q is the specific humidity ($kg kg^{-1}$), $\mathbf{V}_h$ is the horizontal wind vector (ms^{-1}), P_b is 1000hPa, P_t is 200hPa, and g is the acceleration due to gravity. For the 500mb geopotential height field used for the SOM, we remove the seasonal cycle for each grid point to generate anomalies and then standardize (center to 0 with a standard deviation of 1). The composite geopotential heights shown in Fig. 2.2 are generated with the anomalies without standardization. We use a spatial domain from 10N-65N, 110E-255E for our SOM analysis and most of our composites. This domain sufficiently captures the AR genesis and termination locations along with the dynamics affecting ARs.

2.2.2 AR Track Catalogue

To examine the genesis of ARs, both landfalling and non-landfalling, we utilize two different AR catalogues. The primary AR catalogue utilized in this study was generated by Kyle Nardi in Gonzales et al., 2019. This catalogue is based on an adapted Mundhenk AR algorithm (Mundhenk et al., 2016; Shields et al., 2018b) which tracks only landfalling ARs for the US west coast (California to Washington) from landfall back to genesis. The Mundhenk algorithm uses a relative threshold (94th percentile) for IVT values for detection and a

Lagrangian approach to track AR objects across consecutive time steps. There are additional geometric constraints to filter out cyclone-like features (>1400km length, aspect ratio 1:4). It should be emphasized non-landfalling ARs and ARs making landfall poleward of Washington and equatorward of California are not considered in this study. This catalogue begins in Jan 1980. We analyze from 1980 to 2015 during the core wet season months of Nov-Feb when ARs peak seasonally for the US west coast (Mundhenk et al., 2016). For this time period, the catalogue records landfalling ARs for the west coast of the U.S. Each of these ARs has an associated track, recording date and time, latitude, and longitude from landfall back to genesis. The latitude and longitude coordinate is based on the IVT-weighted centroid associated with the AR. We further filter the ARs to consider only those that exist 12 or more hours and end up with 1027 total landfalling ARs for our 36 year period (∼28.5 ARs per wet season). This dataset clearly identifies the landfall days associated with each event and thus allows us to investigate landfall impacts. We henceforth refer to this dataset as the 'Gonzalez' dataset and for all the results in Section 2.2.1, unless specifically noted, will refer to the Gonzalez dataset.

The second AR data used is the widely used AR algorithm developed by Guan and Waliser. The details of this algorithm are discussed in Guan and Waliser, 2015 and Guan and Waliser, 2019. This algorithm catalogues ARs globally using a relative threshold and additional geometric criteria. It tracks all ARs regardless of the AR making landfall or not and includes ARs making landfall outside of the U.S. west coast (California to Washington). We include an analysis of this dataset in Section A to examine how a purely landfalling AR dataset compares to a dataset that considers all ARs - landfalling or not. We do not perform landfalling analysis on this dataset as the location and date of landfalling can be ambiguous for a given event. The ambiguity comes from the catalogue allowing the same AR to make landfall more than once, at various locations, across several timesteps. We subset the catalogue for ARs with genesis in the north Pacific domain of 10N-52.5N,110E-250E. The total number events associated with the total for the Guan and Waliser dataset is 2806. We henceforth refer to this dataset as the 'GW19' dataset.

To reiterate, the two key differences between the GW19 dataset and the Gonzalez dataset are that the GW19 dataset, considers all ARs, landfalling and non-landfalling, and considers all north Pacific ARs, regardless of where they make landfall (as opposed to strictly U.S. west coast landfalling ARs).

2.2.3 Climate Indices

As we are interested in the synoptic patterns associated with AR genesis we use a variety of tropical and extratropical large-scale climate modes that affect the Pacific atmosphere: El Niño Southern Oscillation (ENSO), Pacific Decadal Oscillation (PDO), Pacific North American pattern (PNA), North Pacific index (NP), Arctic Oscillation (AO), West Pacific Oscillation (WPO), and East Pacific Oscillation (EPO). These are the large-scale modes, with the addition of the NP index, that are examined in Guirguis et al., 2019. We additionally include the distribution of Madden-Julian Oscillation (MJO) phases in A. For ENSO, we

use the Oceanic Niño Index (ONI). The temporal resolution of the indices is either daily or monthly. In the monthly cases, daily indices were generated simply by using the monthly value for each day within the month. The temporal resolution of each mode and the sources of data are summarized in the Table 2.1. We standardize the indices to be centered at 0 and have a standard deviation of 1.

Climate Index	Temporal Resolution	Data Source
ONI	*monthly*	NOAA, 2020b
PDO	*monthly*	JISAO, 2020
NP	*monthly*	UCAR, 2020
PNA	*daily*	NOAA, 2020a
AO	*daily*	NOAA, 2020a
WPO	*daily*	NOAA, 2020d
EPO	*daily*	NOAA, 2020c

Table 2.1: Climate indices evaluated with the SOM along with their temporal resolution and data source.

2.2.4 Self-Organizing Maps

SOM analysis (Kohonen, 1982a; Kohonen et al., 2001) is a popular, unsupervised learning technique based on artificial neural network models that has received considerable attention and demonstrated applications in meteorology and climatology including extreme events (Hewitson and Crane, 2002; Sheridan and Lee, 2011; Skific and Francis, 2012; Gibson et al., 2017; Y. Liu and Weisberg, 2011). In many respects, SOMs are analogous to more traditional forms of cluster analysis. A SOM arranges nodes into a 2-dimensional array where similar nodes are located close together in the array and dissimilar nodes are further apart. Thus, in opposite corners, the nodes with the largest differences will be mapped (Sheridan and Lee, 2011).

There are several AR studies that have incorporated SOM analysis. Swales et al., 2016 and Radić et al., 2015 used SOMs trained on IVT to determine the different moisture pathways on the US west coast and to examine the future changes, as projected by CMIP5 models, in ARs making landfall over British Columbia respectively. In contrast to IVT, SOMs trained on geopotential heights were used to study the synoptic scale patterns associated with both landfalling ARs near the Russian River in California (Guirguis et al., 2019) and flood events throughout the U.S. (Schlef et al., 2019). In this study, we employ SOM analysis to similarly examine the synoptic patterns and climate modes associated with AR genesis in the north Pacific.

We include an overview of how the SOM is trained as well as parameter choices in Section A.1.

2.3 Results

2.3.1 Synoptic Patterns of AR Genesis

The synoptic patterns associated with the genesis of U.S. west coast landfalling ARs (Gonzalez dataset) are shown in Fig. 2.2. The various climate indices associated with each node are shown in Fig. 2.3. By examining the indices in Fig. 2.3, the organization of the nodes becomes apparent. Additionally, the synoptic patterns at landfall are shown in Fig. A.4 Section A. The synoptic patterns and associated climate indices for the GW19 dataset are included in Section A (Fig. A.2 and Fig. A.3).

Generally, for ONI, PDO, PNA, and NP, the nodes are organized with a positive to negative phase gradient going from the top left (Node 1) to bottom right (Node 9). These 4 indices are generally in phase and the top left corner nodes (Nodes 1,2,4) are all positive/neutral while the bottom right corner nodes (Nodes 6,8,9) are all negative. For conciseness, we will refer to these collective modes as the 'ENSO modes' throughout the rest of the paper as they generally organize on the SOM map similarly and these modes are known to have strong associations with ENSO. ONI, PDO, and NP (PNA) have their most positive values at Node 1 (Node 4). ONI and PDO (PNA and NP) exhibit strongest negative phasing at Node 6 (Node 9). The synoptic pattern for Node 1 captures familiar boreal winter geopotential height anomalies associated with positive ENSO, PDO, and NP phases; the Aleutian low is deepened with low anomalies extending westward and northward over Siberia and high anomaly heights over Japan, south of the Aleutian low, and over the western U.S. Node 4, which represent positive phases of PNA, has a low anomaly similar to Node 1 but the secondary low is shifted toward the western Pacific over Japan. High anomalies are seen over western North America and in the polar latitudes over Siberia. The negative phase for all 4 of these modes are characterized by high pressure anomalies over the central Pacific as can be seen in Node 9 and 6; node 9's high pressure anomaly has a greater extent and magnitude. For both of these nodes, the high pressure anomaly is surrounded by weaker, low pressure anomalies.

Meanwhile, the AO, WPO, and EPO are generally in phase with the positive to negative phase gradient going from top right (Node 3) to bottom left (Node 7). These 3 indices are all positive/neutral in the top right corner (Node 2,3,6) while the bottom left corner nodes (Nodes 4,7,8) are all negative/neutral. As with the ENSO modes, we will group these modes together and refer to them as 'jet modes' as they organize similarly and for their strong influence on the jet over the Pacific; the jet has been shown to have a strong relationship with landfalling ARs (Payne and Magnusdottir, 2014; Ryoo et al., 2013). WPO has its highest (lowest) value at Node 3 (Node 7), EPO has its highest (lowest) value at Node 2 (Node 7), and AO has its highest (lowest) value at Node 3 (Node 7). The respective most positive nodes for these three indices reflect differences in typical anomalies associated with the indices. Node 3 (WPO and AO's most positive) and Node 2 (EPO's most positive) show the low anomaly center in the western/central and eastern regions of the north Pacific respectively. When these modes are positive, the jet tends to be shifted northward. The
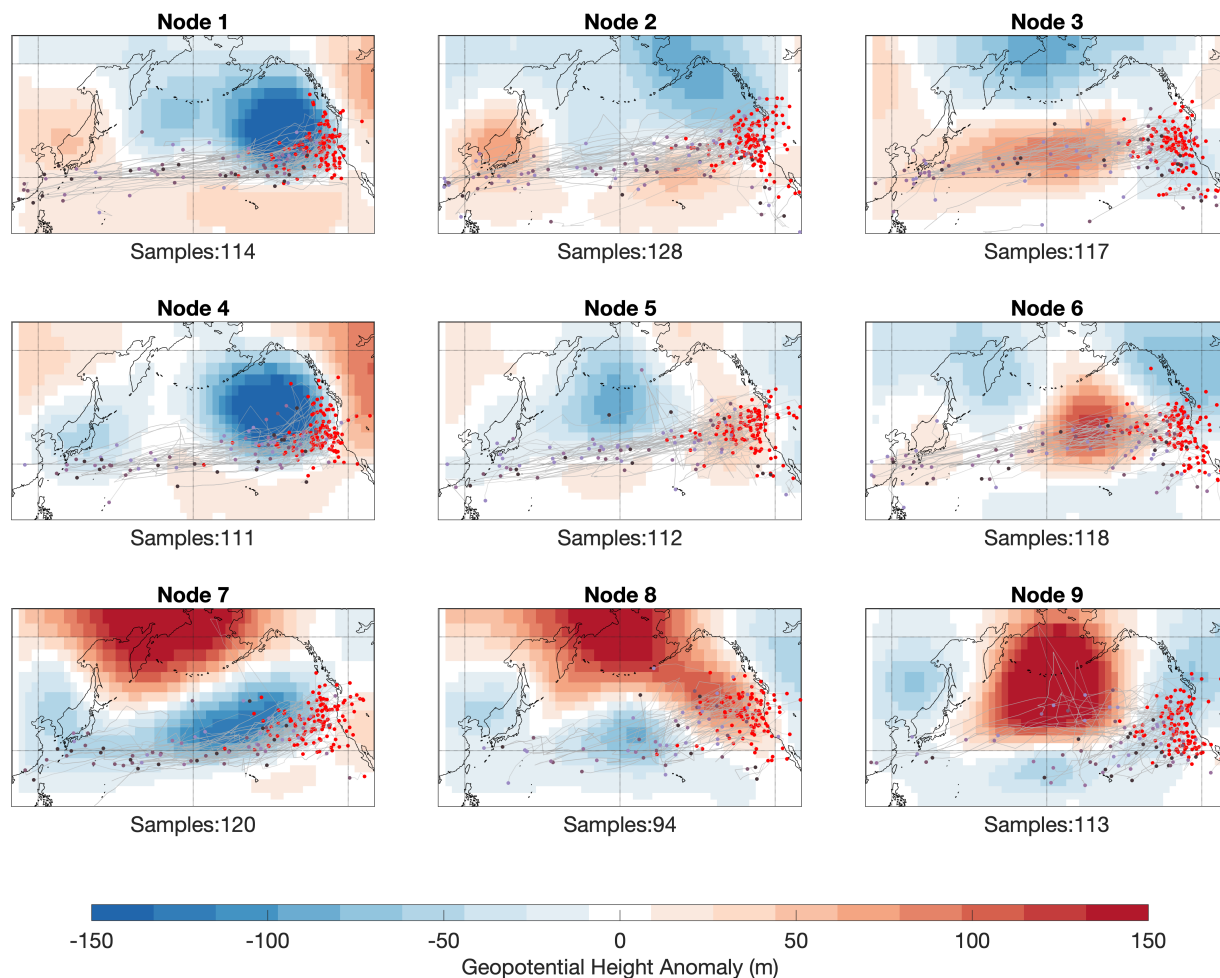
Figure 2.2: The SOM trained on AR genesis day 500mb geopotential height anomalies. The nodes are composites of the genesis day geopotential heights of all the ARs that are assigned to a given node. The AR tracks are also displayed with the genesis points in purple and the landfall points in red. The landfall points do not fall precisely on the coast because the track points represent the IVT weighted centroid of the AR object at a given timestep. Thus, when a zonally long AR's leading edge makes landfall, the IVT weighted centroid may be located far off coast.

most negative node for these modes (Node 7) combines features from Node 2 and 3 but with the sign of the anomaly reversed. The high pressure ridge is characteristic of the negative phases of these modes and is associated with an equatorward shifted jet stream. The center node (Node 5) of the SOM has a weaker overall anomaly composite relative to the other nodes. Additionally, the climate indices do not respond strongly to this node with perhaps the exception of NP. This is not unexpected due to the small size of the SOM map; at the
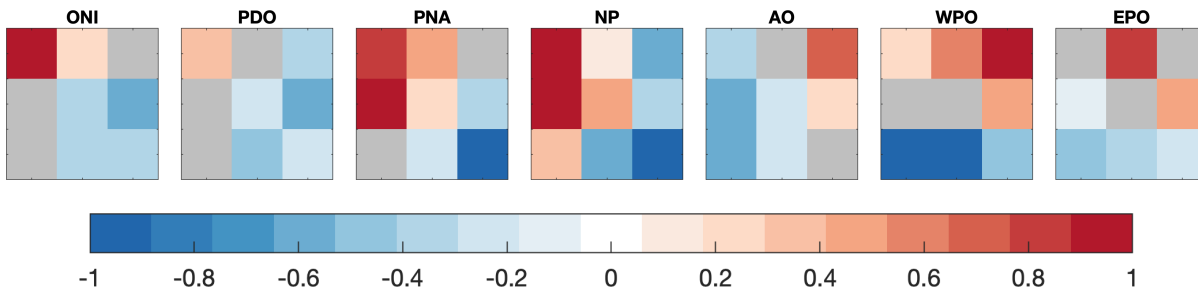
Figure 2.3: The various climate indices' average values for each node corresponding with the SOM in Fig. 2.2 (Node 1 on the top left corner, Node 9 on the bottom right). The averages were calculated from the value of the index on all the AR genesis days associated with a node. Red (blue) values indicate positive (negative) phases of the respective indices. White values indicate neutral conditions or not statistically different from climatology (t-test for unequal means, 95% confidence

beginning of the ordering phase training, any update to any of the 9 nodes will affect the center node due to the neighborhood radius and thus, there may be several different and competing synoptic patterns grouped to form Node 5's composite. However, this was the tradeoff for ease of interpretation and analysis versus increasing the SOM order. While the focus of this study is on US west coast landfalling ARs, we note similarities and differences in the SOMs produced by the Gonzalez dataset and the GW19 dataset. Examining the SOMs generated by the two AR catalogues (Gonzalez et al in Fig. 2.2 and GW19 in Fig. A.2), similar and consistent geopotential height composites and organization are apparent.

There are however notable differences. Given that the GW19 dataset contains a substantial number of ARs that do not make landfall as well as landfalling ARs in Canada and Alaska, the synoptic conditions in the GW19 nodes, as can be expected, are not as conducive for moisture transport specifically to the west coast of the U.S. In general, most of the GW19 synoptic conditions are associated with jets that do not extend as far eastward and support moisture transport to higher latitudes compared to the Gonzalez synoptic conditions. More detail found in Section A.2.

How often do the Gonzalez SOM synoptic conditions show up during the cool season (defined here as Nov-Feb)? We match each cool season day's geopotential height field to the best matching node in Fig. 2.4a. Frequency analysis of all the cool season days reveals that Node 5 is most similar to climatology as it has the highest frequency of cool season days that match (12.8%). As previously stated, Node 5's anomalies are the weakest compared to other nodes. In fact, Nodes 2, 3, 5, and 6 all generally have weaker anomalies relative to the other nodes and have a higher frequency of cool season days that match. Node 1 has the lowest frequency at 8.8% which means it is the most uncommon synoptic pattern out of all the nodes. Overall, the left column and bottom row nodes (Nodes 1, 4, 7, 8, and 9) have lower occurrences during the cool season while the top right and center nodes (Nodes 2, 3, 5, and

(a)   (b)
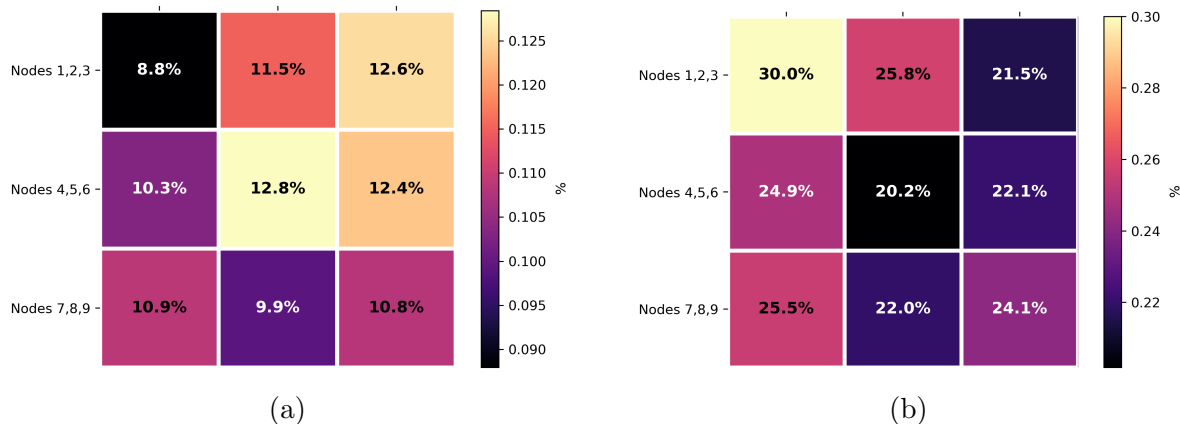
Figure 2.4: a) Percentage of all cool season (Nov-Feb) days that best match the synoptic conditions of each node. b) Percentage of AR genesis days occurring during the cool season days that match the synoptic conditions of each node. This shows how often certain synoptic conditions generate ARs.

6) occur more commonly. However, if we examine the frequency of AR genesis occurring on the cool season days that match each respective node (Fig. 2.4b), Node 1's frequency has by far the largest at 30.0% while Node 5's frequency is the lowest at 20.2%. This means that, while the synoptic conditions associated with Node 1 occur the least frequently throughout the cool season, when it does happen to occur, 30.0% of the time, it produces an AR.

2.3.2   AR Characteristics

In the following section, the different AR characteristics associated with the nodes of the SOM are presented. We focus primarily on the corners of the SOM for their ability to represent positive and negative phases of the ENSO modes and the jet modes. These corners also represent the most dissimilar nodes within the SOM. Various average AR metrics were extracted from the AR tracks which can be seen in Table 2.2: genesis coordinate (Col 2), landfall coordinate (Col 3), AR lifecycle duration in hrs (Col 4), distance traveled in km (Col 5), average velocity in km/hr (Col 6), AR track latitude (Col 7), AR track longitude (Col 8), AR meridional movement in degrees (Col 9), AR zonal movement in degrees (Col 10), and the ratio between zonal movement and meridional movement (Col 11). The genesis and landfall coordinates are based on the IVT weighted centroids of the AR object. This explains why the landfall coordinates do not lie precisely on the coast.

Node	Genesis	Landfall	Dur(hr)	Dist(km)	Vel(km/hr)	Lat	Lon	Merid	Zonal	Aspect
1	32.3N,177.0E	39.2N,228.7E	103.8	7413	71.4	34.3N	196.6E	6.9	51.7	7.5
2	32.4N,175.3E	40.8N,230.0E	99.3	6627	66.7	36.2N	192.5E	8.4	54.7	6.5
3	32.4N,182.6E	39.0N,230.6E	92.2	5720	62.0	36.2N	195.6E	6.6	48.0	7.3
4	32.9N,185.8E	39.7N,228.6E	85.4	5892	69.0	34.7N	199.1E	6.7	42.9	6.4
5	33.7N,176.8E	40.6N,229.3E	97.6	6718	68.9	36.3N	195.8E	7.0	52.5	7.5
6	32.8N,181.5E	39.8N,229.8E	66.4	6012	66.4	36.9N	195.3E	6.9	48.4	7.0
7	30.4N,179.0E	39.4N,227.6E	98.4	6226	63.3	33.3N	197.8E	9.1	48.6	5.3
8	33.7N,191.3E	40.7N,229.5E	83.7	5098	60.9	35.9N	202.3E	6.9	38.2	5.5
9	31.1N,199.1E	37.3N,230.9E	77.2	4430	57.4	35.2N	206.0E	6.2	31.9	5.1

Table 2.2: Summary of various AR characteristics associated with each node of the SOM.

The representative nodes of the ENSO modes (Node 1 for positive, Node 9 for negative)
produce ARs with several significant differences. The average genesis longitude for Node 1
compared to Node 9 is further west by 22°. In fact, Node 9 has genesis occurring closest to the
west coast compared to all other nodes. Node 2, another strongly positive large-scale mode
node, is 24° further west and has the most western genesis longitude. The genesis latitude
is varies by about 1° between the positive (32.3N) and negative (31.1N) phases. Landfalls
occur 2° more poleward and 2.2° more westward when ENSO modes are positive. Landfall
longitudes further off-coast can suggest ARs of larger size as the coordinate is determined by
the IVT weighted centroid of the AR object. If we compare the most positive (Node 1) and
negative (Node 6) ONI nodes, landfall is further south during El Niño compared to La Niña
which is expected (Payne and Magnusdottir, 2014). The duration, distance traveled, and AR
speed are significantly longer (>24 hrs), farther (>1.5x), and faster (14km/hr) under positive
ENSO modes. The negative phase node (Node 9) has the lowest duration, shortest distance,
and slowest speed compared to all other nodes. The average latitude of the AR tracks do
not vary significantly but the average longitude of the AR tracks is significantly further east
(9.4°) when the ENSO modes are negative owing to the genesis occurring much closer to the
west coast of the U.S. In addition, the zonal displacement is more than x1.5 larger between
the positive (Node 1) and negative (Node 9) nodes while meridional displacement is similar.
This causes these two nodes to have the most zonal (Node 1) and meridional (Node 9) ratios
amongst all nodes.

The representative nodes of the jet modes (Node 3 for positive, Node 7 for negative)
also produce ARs with different characteristics. Genesis occurs at the lowest latitude for the
negative jet mode node compared to all the other nodes and is 2° equatorward compared
to positive jet mode node. The genesis longitudes are both located quite far west with
the positive mode 3.6° further east. Landfall longitude is 3° eastward and closer to the
coastline for the positive phase suggesting smaller ARs. Duration, distance, and velocity
are not significantly affected between positive and negative phase nodes. These two nodes
however, have the most poleward (positive phase Node 3) and equatorward (negative phase
node 7) average track latitudes producing the greatest difference in track latitudes (2.9°)
compared to any other node pair. The positive and negative modes have similar zonal
displacements but differ in the meridional displacement; the positive phase has much less
meridional displacement (2.5°). This leads to pronounced differences in their ratios with
the positive phase producing more zonal ARs trajectories and the negative phase producing
more meridional trajectories.

While the Gonzalez and GW19 datasets catalogue different sets of north Pacific ARs,
interestingly, much of the characteristics associated with the nodes is consistent between
both datasets. More details are included in Section A.2.

To summarize the AR characteristics, the ENSO phases strongly affect the longitudinal
position of genesis, lifecycle duration, distance traveled, velocity of the AR, and the zonal
displacement of trajectories. When positive versus negative, ARs tend to originate from the
central or west Pacific, last longer, travel further, move faster, and tend to have zonal trajec-
tories. The jet mode phases strongly affect genesis latitude, track latitude, and meridional

displacement. When the jet modes are positive versus negative, ARs tend to have genesis at higher latitudes, travel at higher latitudes, and tend to have zonal trajectories. How do these different characteristics translate to hydrological impacts when the ARs eventually make landfall? Latitude, orientation, and local topography at landfall are all important factors that determine how much precipitation will rain out (Hughes et al., 2014; H. Hu et al., 2017; Hecht and Cordeira, 2017; Neiman et al., 2011).

2.3.3 Hydrological Impacts

We examine the IVT and precipitation magnitude and distribution using the landfall days of every AR event associated with each node. For instance, if an AR has genesis on Dec. 1 and makes landfall on Dec. 3, then the Dec. 3 date is used for the landfall composites. The IVT and precipitation associated with each node is shown in Fig. 2.5 and Fig. 2.6. The IVT shown in Fig. 2.5 is the raw IVT, not the anomaly, on the day of landfall. The precipitation shown in Fig. 2.6 is the anomaly over 2 days; the landfall day and the following day. This was done to capture the precipitation from ARs that may have landfall durations that span across more than 1 day. For the following results, note that the Gonzalez dataset only includes ARs making landfall from California to Washington.

Generally, the top right nodes (Nodes 2, 3, and 6) and the center node (Node 5) produce smaller amounts of precipitation while the left (Nodes 1, 4, 7) and bottom (Nodes 7, 8, 9) edge nodes produce more precipitation. The spatial distribution of precipitation also varies amongst the nodes. Nodes 1, 4, and 9 tend to produce more precipitation over California and just off-shore over the Pacific compared to the other nodes which have the biggest precipitation anomalies over the Oregon and Washington. The weaker precipitation nodes in the top right accordingly have the weakest IVT signatures just off coast. The IVT signature of these nodes also tends to be quite zonal; the other nodes, which produce stronger precipitation on the west coast, have a relatively southerly or southwesterly IVT orientation at landfall. Lastly and importantly, the weak precipitation nodes have the most poleward average latitude for their trajectories. Nodes with synoptic patterns conducive for AR trajectories to reach further equatorward are favorable for stronger precipitation to the west coast.

In Fig. 2.7a, we take a difference with the positive phase node (Node 1) and negative phase node (Node 9) for the ENSO modes. ARs that form when ENSO modes are positive deliver more precipitation to northern California, Washington and poleward of Washington (Canada to Alaska). Southern/central California and parts of the US interior experience precipitation deficits. Both of these nodes deliver relatively large amounts of precipitation compared to the other nodes. The precipitation anomalies poleward of Washington are higher or of comparable magnitude to the anomalies over the U.S. even though the AR dataset is for landfalling ARs over California, Oregon, and Washington. This may be a signal coming from North American west coast ARs generally being more prevalent during positive phase ENSO modes (Payne and Magnusdottir, 2014). The precipitation anomaly for Node 9 is negative over Canada and Alaska.
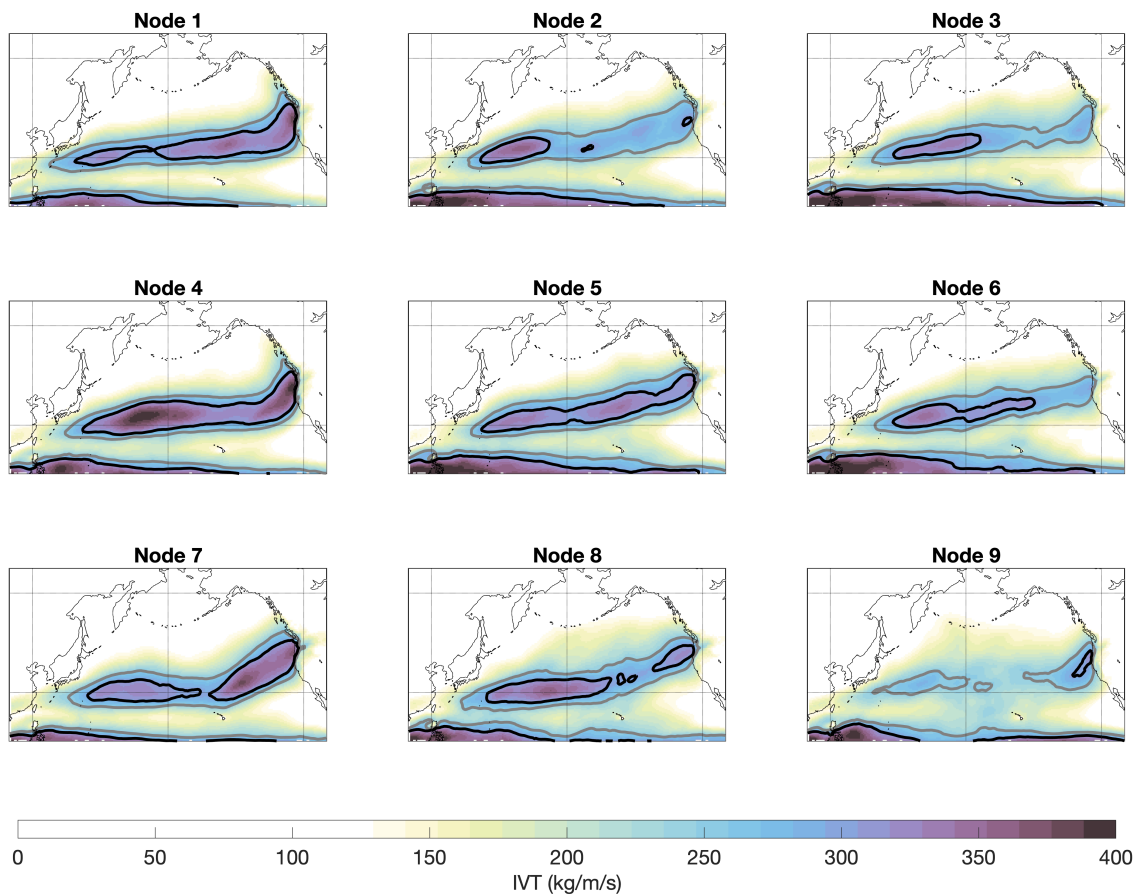
Figure 2.5: Composites of IVT on the landfall day of all the ARs associated with each node of the SOM.

The expectation of El Niño precipitation compared to La Niña is for most of California to be wetter while Oregon and Washington are drier. Although this pattern is not represented using the corner nodes (Nodes 1 and 9), it emerges if we subtract the most El Niño node (Node 1) and the most La Niña node (Node 6) as seen in Fig. A.5 in Section A.

Taking the difference for the positive (Node 3) and negative (Node 7) phase nodes for the jet modes produces Fig. 2.7b. When the jet modes are positive, precipitation is weakly enhanced for southern California while in northern California and the PNW, precipitation shows negative anomalies. Examining the IVT associated with these nodes (Fig. 2.5), we can see similar structures and magnitudes in the IVT band over the western Pacific. However, over the central Pacific, the negative phase node (Node 7) IVT curves towards the equator while the positive phase node curves poleward which leads to much stronger IVT values over the eastern Pacific for the negative mode. Examining the IVT at Hawaii's longitude, Node 7's IVT signature nearly overlaps Hawaii at its southern flank while for Node 3, the IVT
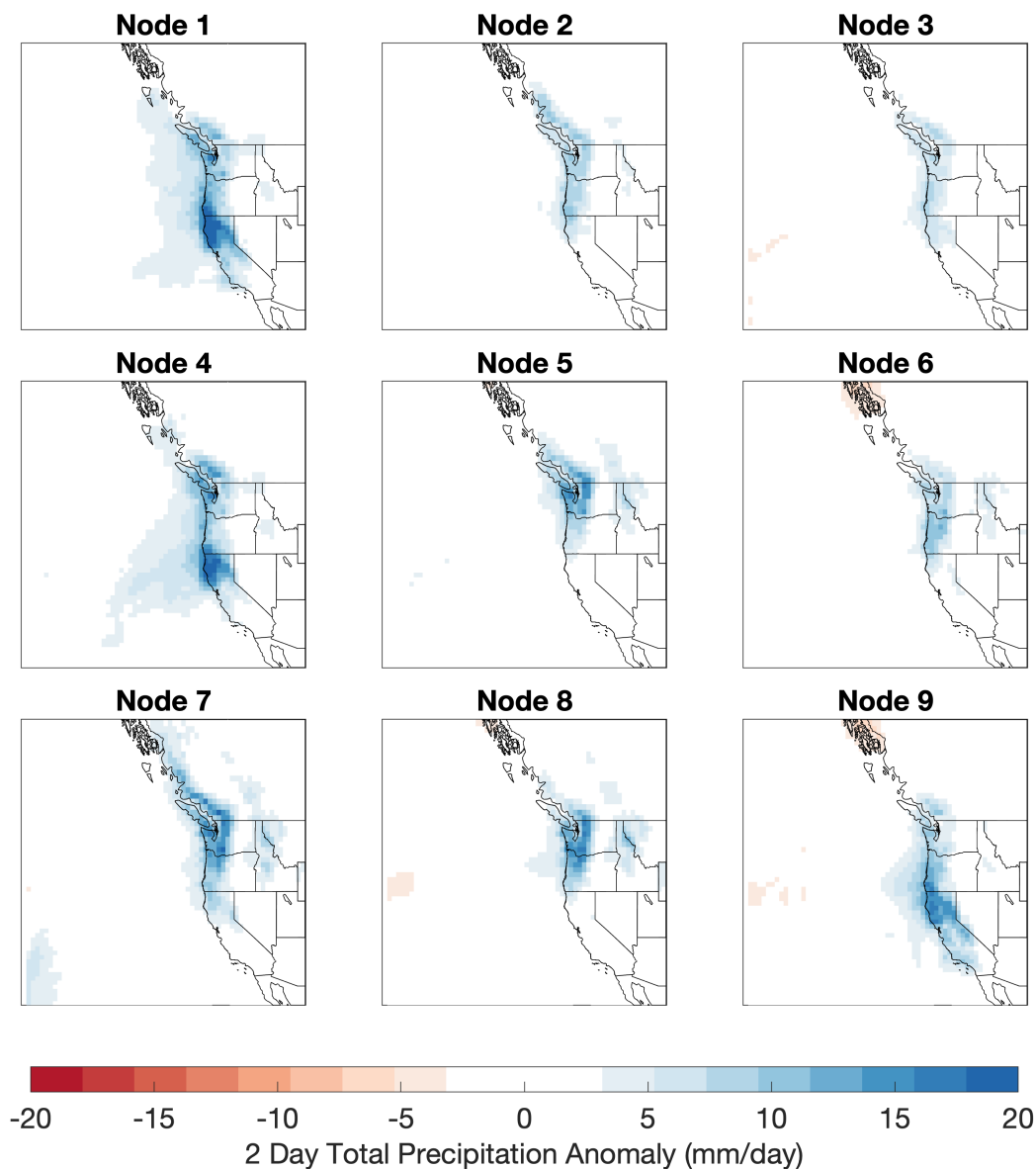
Figure 2.6: Composites of precipitation anomaly over 2 days (landfall day and the following day) of all the ARs associated with each node of the SOM.

signature is north of Hawaii by ∼15°.

2.3.4   Large-scale circulation

In this section, we examine the large-scale circulation associated with the nodes in the SOM. Fig. 2.8, Fig. 2.9, Fig. 2.10, and Fig. 2.11 show the genesis day composites of upper level 250
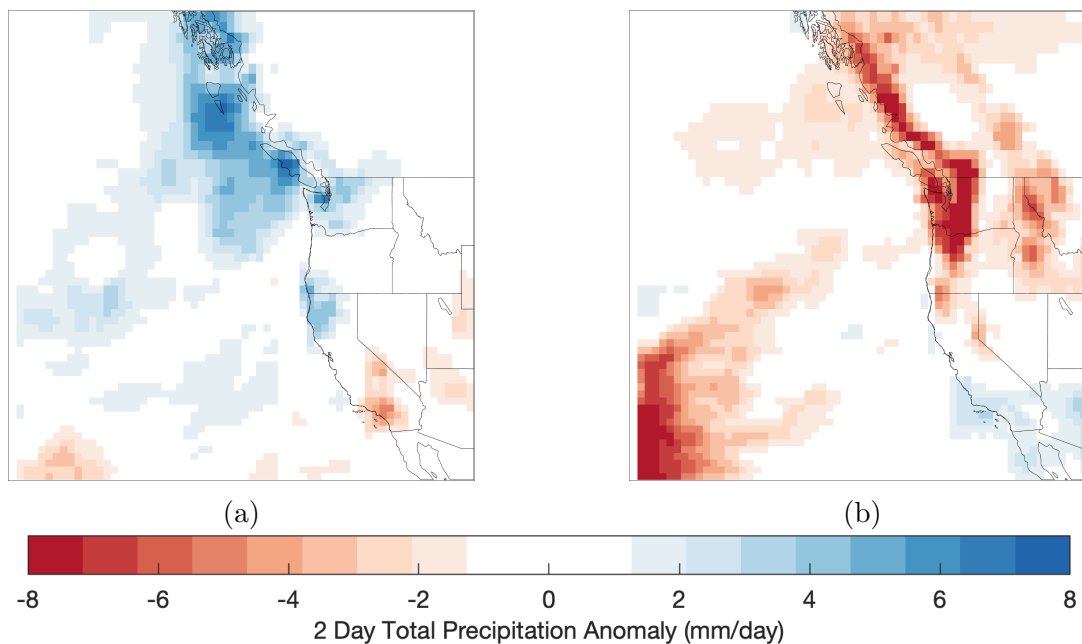
Figure 2.7: a) Positive phase node (Node 1) of the ENSO modes minus the negative phase
node (Node 9). Precipitation anomaly over 2 days on and the following day of landfall. b)
Positive phase node (Node 3) of the jet modes minus the negative phase node (Node 7).
Precipitation anomaly over 2 days on and the following day of landfall.

hPa zonal winds, anomalous 850 hPa wind vectors, IVT, and 200hPa PV respectively. From
Fig. 2.10, areas corresponding to the genesis locations for each node have enhanced IVT
values. Fig. 2.9 anomalies reflects the lower level circulation changes due to the geopotential
height anomalies. From Fig. 2.8, clear differences in the strength and position of upper level
jet can be seen amongst the various nodes. The organization of these winds correspond to
the typical jet patterns associated with the ENSO modes and jet modes. Generally moving
from top to bottom on the SOM, the jet tends to retract westward and become weaker while
moving from left to right on the SOM, the jet becomes more variable. Node 1 shows a clear
example of a strong, zonal jet and Node 9 shows a weak, variable jet. Along with these jet
changes, the PV gradient in the central Pacific goes from strong to weak moving from the
left to the right nodes. The PV field at landfall is included in Section A.

   A deepened Aleutian low and strong PV gradient aloft during the positive ENSO modes
supports a strong and zonal jet while the negative phase is characterized with a weaker, less
zonal jet due to high pressure anomalies over the central Pacific and the PV intrusions into
the subtropics. The PV gradient is much weaker in the negative ENSO mode. The jet and
upper level PV conditions between positive and negative ENSO modes are consistent with
Ryoo et al., 2013. When the jet modes are positive, the jet is aimed slightly northward with
a poleward curve while during negative jet modes, the jet is curved towards the equator
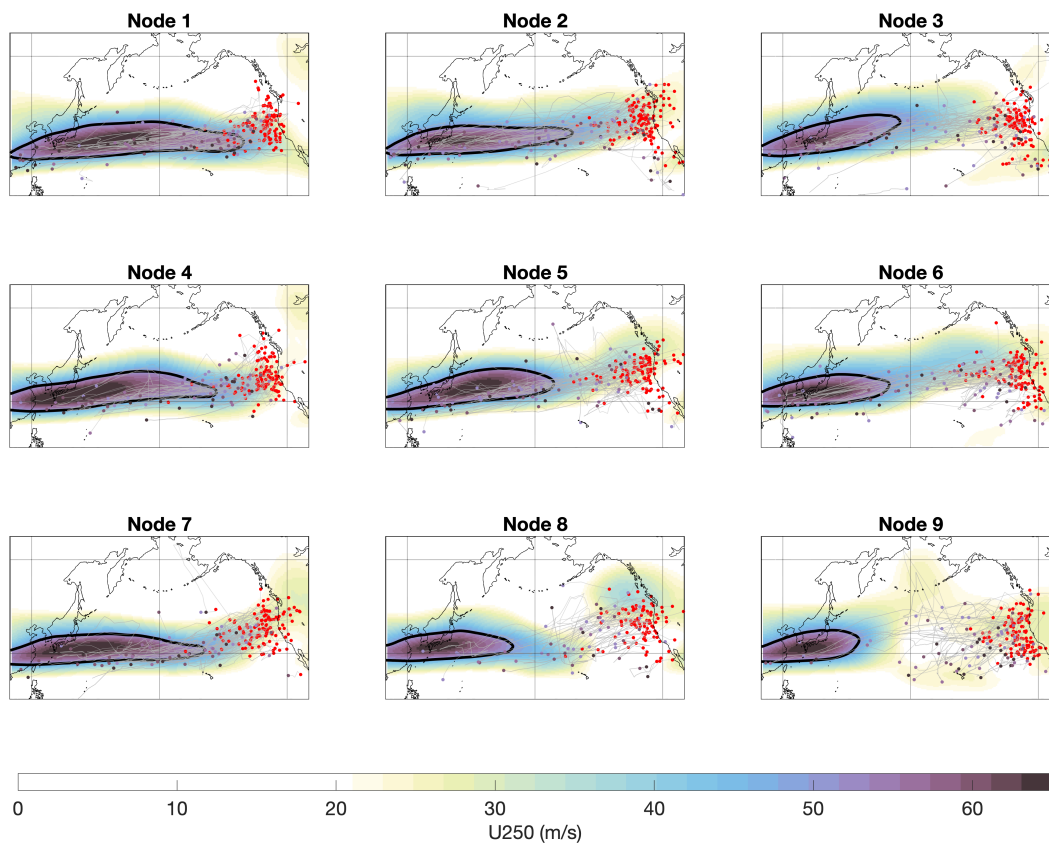
Figure 2.8: Composites of the 250 hPa zonal wind on genesis day. AR track information is overlaid.

due to the high pressure over the central Pacific. Focusing on Hawaii, the difference in jet position becomes obvious for the positive (Node 3) and negative (Node 7) jet modes. During the negative jet modes, the jet is typically more variable and tends to curve much closer to the tropics, allowing the jet stream to penetrate to lower latitudes where moisture is more abundantly available.

During positive ENSO modes (Node 1), genesis occurs along the core of the strong upper level jet over the west and central Pacific. Genesis also occurs on the equatorward flank of the enhanced Aleutian low in the eastern Pacific which corresponds with lower level westerly or southwesterly winds. This suggests west Pacific AR genesis may depend more on the upper level jet activity while east Pacific AR genesis could be more related to lower level dynamics. During negative ENSO modes (Node 9), genesis locations are less constrained, especially latitudinally, with very few ARs forming with the weak, retracted jet over west Pacific and the vast majority forming in the central Pacific and close to the coastline. The upper level jet is overall weak and variable (suppressed over the central Pacific by the high
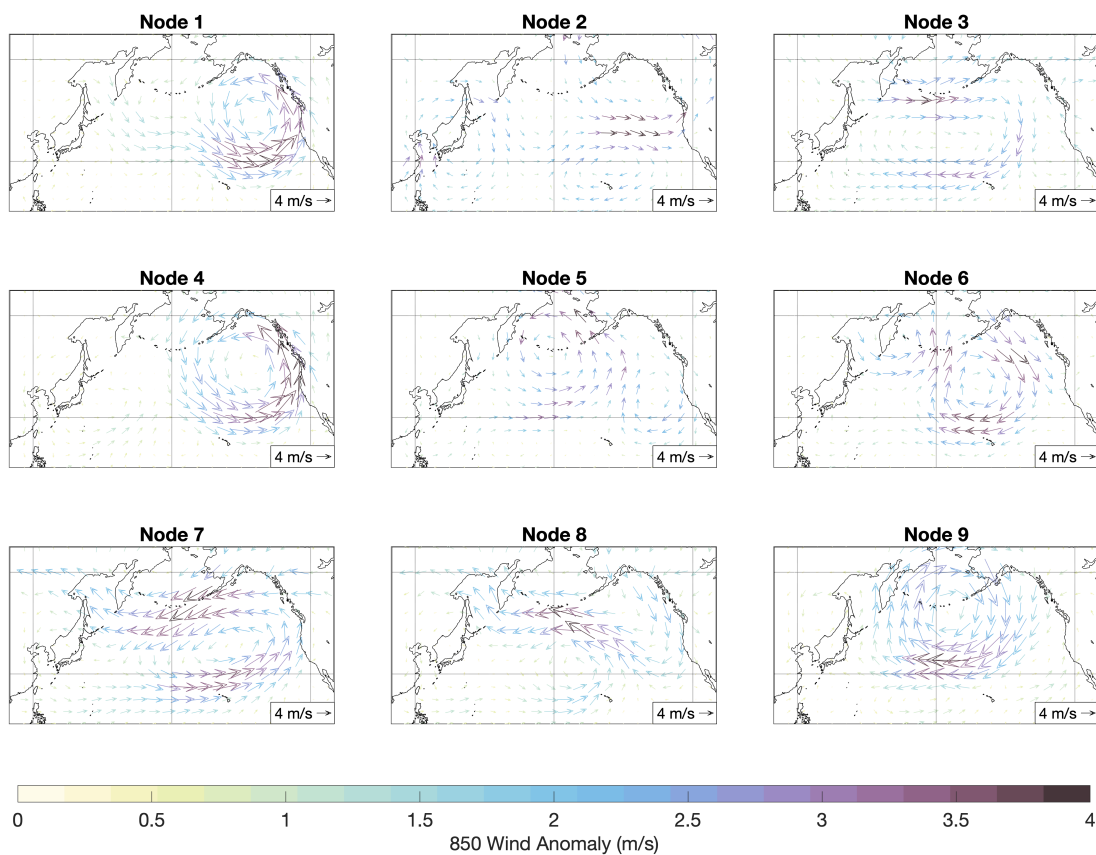
Figure 2.9: Composites of the 850 hPa wind anomaly on genesis day.

pressure anomaly) over the central and east Pacific compared to the positive mode. The
genesis locations in the eastern Pacific correspond to relatively weak southwesterly winds
near the moist tropics in the negative modes.

During positive jet modes, genesis occurs all along the straight and slightly poleward
tilted jet core. On the southern flank of the jet there are strong, anomalous lower level
easterlies that suppress the formation of ARs closer to the tropics. The handful of genesis
points near the Baja California peninsula are associated with relatively weak southwesterly
lower level winds near the tropics. When the jet modes are negative, genesis locations
similarly are co-located where the jet is strong in the west and central Pacific - which again
is significantly further equatorward compared to the positive jet mode. The lower level winds
associated with the low pressure anomaly south of the high pressure polar ridge support AR
formation in the central and east Pacific. The orientation and location of the jet and the
lower level wind anomalies generate strong IVT ARs as AR genesis occurs in warmer and
moister latitudes. Landfalling ARs in all of the nodes tend to form along the core location
of the upper level jet. However, east Pacific ARs can also form along anomalous southerly
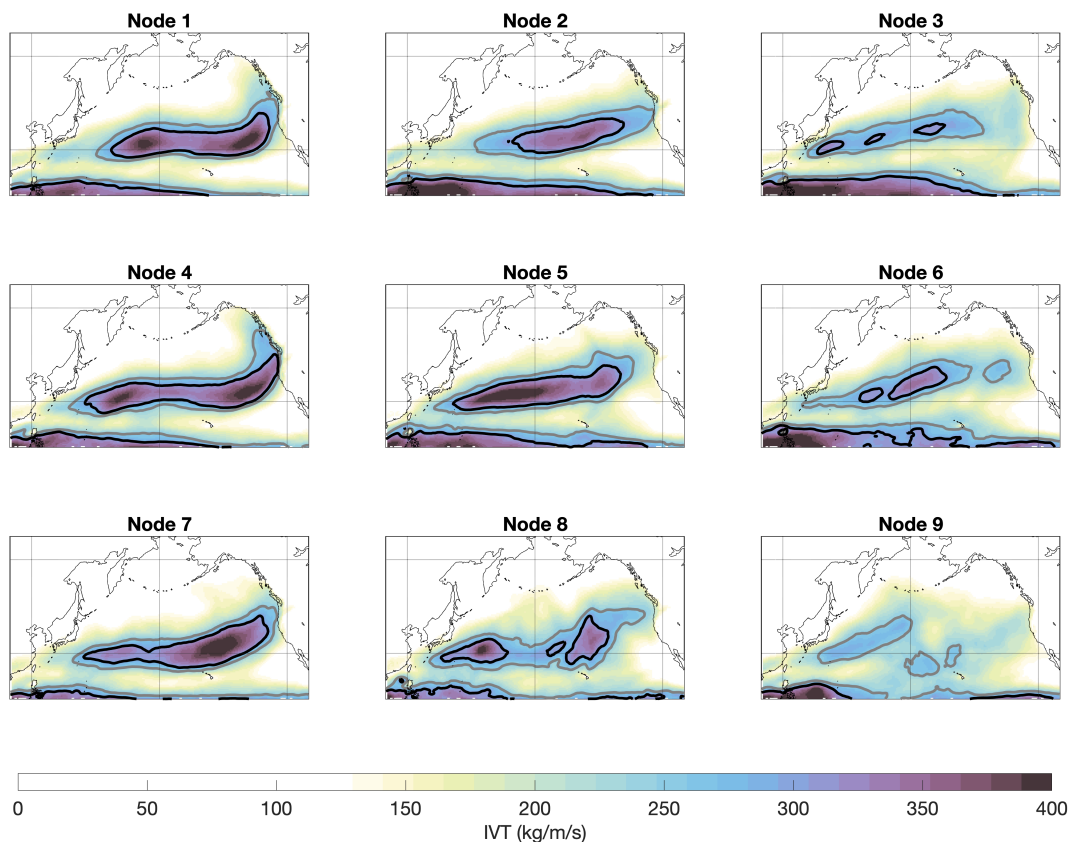
Figure 2.10: Composites of IVT on genesis day.

or southwesterly low-level winds. The jet and low-level wind location and can influence the intensity of IVT associated with the ARs; if the jet position is closer to warmer, moister latitudes near the tropics and subtropics, then higher IVT values will be associated with the ARs. The opposite is true if these features are at higher latitudes.

2.4   Conclusions

This study objectively identified 9 unique synoptic patterns associated with landfalling atmospheric river genesis using a 3x3 order SOM. These patterns are largely organized with positive and negative ENSO modes (ENSO, PDO, PNA, NP) in opposite corners and positive and negative jet modes (AO, WPO, EPO) in the other opposite corners. These synoptic conditions have differing frequencies throughout the cool season and produce ARs at different frequencies when they do occur. The variety of synoptic conditions produce and support landfalling ARs with largely unique lifecycle characteristics. The positive ENSO mode ARs compared to the negative mode ARs form farther west in the Pacific basin, last longer, travel
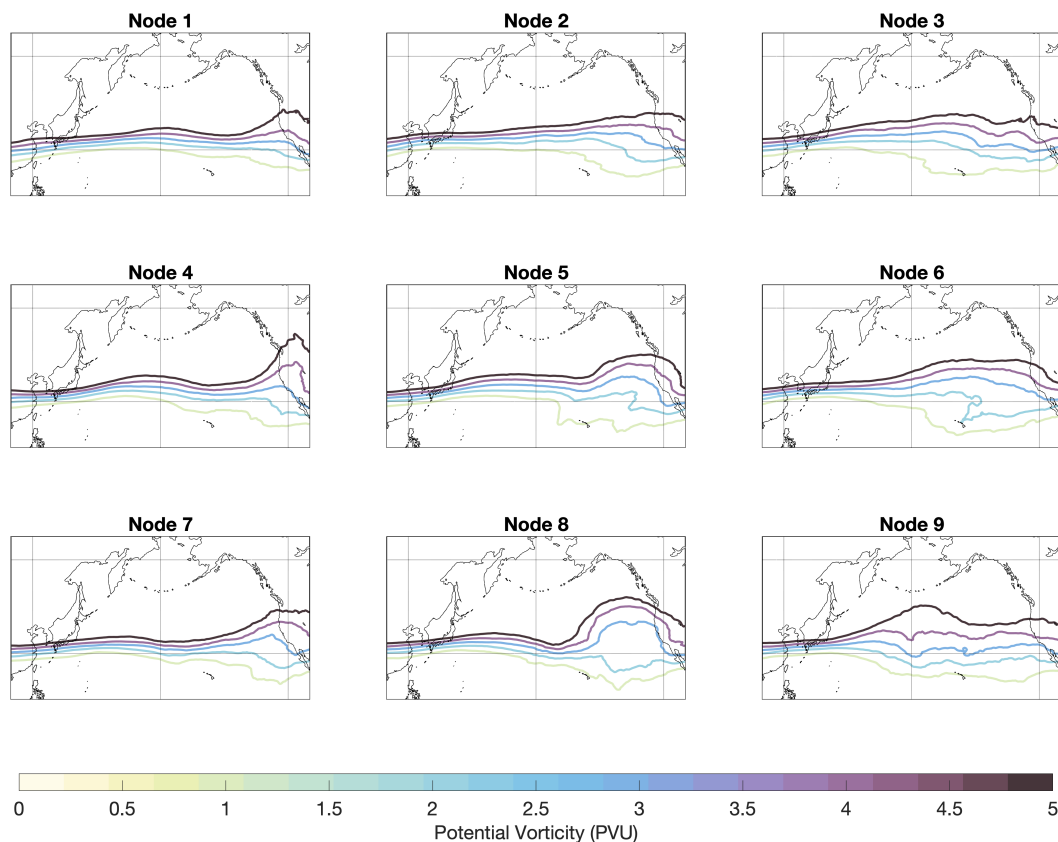
Figure 2.11: Composites of upper level (200hPa) PV on AR genesis day.

further, move faster, and have more zonal trajectories for most of their lifecycle. These ARs also tend to produce more precipitation in northern California and Washington; the negative mode ARs tend to produce more precipitation in southern California and in the interior of the US.

For the jet mode ARs, the speed, duration, and distance traveled does not vary strongly between positive and negative phases. However, the genesis latitude, average track latitude, and meridional displacement of ARs is strongly affected. The positive phase has more poleward genesis and average track latitude and tend to have more zonal trajectories. These characteristics have important consequences for the strength of the AR and the resulting precipitation. The positive phase jet mode ARs generally bring the least amount of precipitation to the much of the west coast while the negative phase is associated with enhanced precipitation in northern California, Oregon, and Washington. Parts of southern California, and the south west interior receive more precipitation when positive. For all nodes, the synoptic patterns that support AR trajectories closer to the moist tropics tend to produce higher precipitation.

Although the focus of this paper is on U.S. west coast landfalling ARs, we also analyze the GW19 AR dataset which considers all north Pacific ARs irrespective of the AR landfall location or the AR terminating over the ocean. The synoptic conditions and their organization with respect to the climate modes considered is, to a large degree, consistent with the Gonzalez dataset as are the lifecycle characteristics.

We additionally examine the large-scale associated with landfalling AR genesis in each node. The position and strength of the upper level jet has a close relationship with AR activity and particularly, AR genesis in the west and central Pacific. In the east Pacific, AR activity and genesis can be tied to southerly or southwesterly lower level wind anomalies which suggests these ARs may be related to tropical moisture. Although Rossby wave breaking was not analyzed in this study, we note that the corner nodes 1 and 7 are associated with more cyclonic Rossby wave breaking events (rather than anticyclonic Rossby wave breaking events) as El Ninos and negative WPO are known to be associated with higher cyclonic breaks (Ryoo et al., 2013,Rivière, 2010). Nodes 3 and 9 are associated with higher anticyclonic breaking events as they are related to La Ninas and positive WPO.

We have shown here that the different synoptic patterns ARs form under are an effective way of understanding an AR's lifecycle characteristics and impacts. The results indicate, for instance, that all strong ARs are not tied to a single type of synoptic condition but rather are possible under a range of conditions (such as both El Niño and La Niña). The same could be said of landfall location. Thus, compositing of AR events given some criteria such as IVT intensity or landfall latitude, as have been done in previous studies, can actually mix a variety of synoptic conditions together. Here, we let the background synoptic condition dictate our grouping of ARs and these groupings reveal their own unique AR characteristics.

2.5 Acknowledgements

Chapter 3

Atmospheric River Representation in the Energy Exascale Earth System Model (E3SM) Version 1.0

3.1 Introduction

Atmospheric rivers (ARs) are central actors in the global water cycle and have significant human impacts. These features are narrow, filamentary structures of concentrated water vapor transport in the lower atmosphere responsible for transporting the majority of water vapor across the mid-latitudes towards the poles (Zhu and Newell, 1998). Recently, ARs have received a categorization similar to hurricanes which describes the wide range of possible AR impacts - both beneficial and destructive (F. M. Ralph et al., 2019). Weaker ARs, with integrated vapor transport (IVT) values of around 250 kg m^{-1} s^{-1}, can provide regions such as the west coast of the U.S. with critical sources of precipitation, while exceptional ARs, with IVT values well over 1250 kg m^{-1} s^{-1}, can be associated with widespread flooding and hazards to both human life and infrastructure. A recent study examining the last 40 years of floods in the western U.S. found ARs pose a \$1 billion-a-year flood risk (Corringham et al., 2019). Many studies indicate that ARs will increase in frequency and/or intensity and will deliver more precipitation under global warming (e.g. Payne and Magnusdottir, 2015; Espinoza et al., 2018; Payne et al., 2020; T. A. O'Brien et al., 2021). On the west coast of the U.S. for example, ARs are expected to increase the occurrence of extreme precipitation and associated flood risk, including via their contribution to snow/ice melt (Swain et al., 2018; Chen et al., 2019). With such important socioeconomic impacts, increasing our understanding of ARs in past, present, and future climates is critical to mitigate damage and protect life and property.

Although ARs have been directly observed since the late 1990s with aircraft and drop-sondes (e.g. the California Land-falling Jets Experiment (CALJET) (F. M. Ralph et al., 2005) and via satellites with passive microwave radiometers (F. M. Ralph et al., 2004; F. M. Ralph et al., 2006), there still exists gaps and challenges to direct observations of ARs due to

both the scale and the extreme environments associated with ARs. While efforts to directly observe ARs continues to be improved, much of these efforts to date have been regionally specific to the western U.S., where ARs play a critical role in water resources. Thus, many researchers have instead relied on the use of gridded reanalysis products - which incorporate a variety of observations - to study ARs in historical, regional, and global perspectives (F. M. Ralph, Dettinger, Rutz, et al., 2020a). Given the socioeconomic impacts of ARs, there is also wide and increasing interest on the behavior of ARs in future climates which typically require the use of global climate models (GCMs) (e.g. Dettinger et al., 2011; Payne and Magnusdottir, 2015; Warner et al., 2015; Shields and Kiehl, 2016). A critical step in using these GCMs, which are used to simulate ARs in a variety of climates, is to first establish confidence in the model's ability to simulate ARs in the current climate.

Many efforts have already evaluated a large array of different models. For example, Guan and Waliser, 2017 evaluated 22 GCMs that participated in the Global Energy and Water Cycle Experiment (GEWEX) Atmospheric System Study (GASS)-Year of Tropical Convection (YoTC) Multimodel Experiment which included both atmosphere-only and ocean-atmosphere-coupled models for the period of 1991-2010. They used reanalysis products to quantify model errors in the context of reanalysis uncertainty and found large errors across all models. Another study by Espinoza et al., 2018 evaluated 21 GCMs in the Coupled Model Intercomparison Project Phase 5 (CMIP5) for their representation of ARs in historical and two future climates (Representative Concentration Pathway, or RCP, 4.5 and 8.5). The multimodel mean (MMM) was a good representation of their reference dataset, ERA-Interim, but tended to have a general underestimation of AR frequencies in the midlatitudes. Additionally, intermodel differences showed significant disagreement for AR frequencies in the subtropics. Payne and Magnusdottir, 2015 performed a similar analysis on landfalling ARs to understand responses to warming in RCP8.5 and compared CMIP5 historical runs to both ERA-Interim and the Modern-Era Retrospective Analysis for Research and Applications (MERRA) as an initial step. Most models were able to resolve the general shape of wintertime landfalling AR frequencies but only a few could resolve other characteristics such as interannual variability in amplitude of moisture flux and median landfalling latitude. A strong relationship between model biases in the North Pacific subtropical jet and landfalling AR frequency on the west coast of North America has been identified based on analysis of large ensemble simulations from Community Earth System Model (CESM) (Hagos et al., 2016). More recently, T. A. O'Brien et al., 2021 evaluated several CMIP5 and CMIP6 models' historical simulations (prior to evaluating a projection scenario) against MERRA2 and found frequency distributions to be remarkably consistent.

The United States Department of Energy (DOE) recently released the Exascale Energy Earth System Model version 1 (E3SMv1) which is a state-of-the-science Earth system model. The model was developed to support the DOE's energy mission, with an emphasis on modeling the long-term changes in air and water temperatures, water availability, storms and heavy precipitation, coastal flooding and sea-level rise on high performance computers (Leung et al., 2020). The standard resolution model (1° x 1°) has been shown to credibly simulate earth's climate when evaluated by means of a standard set of Coupled Model

Intercomparison Project Phase 6 (CMIP6) Diagnosis, Evaluation, and Characterization of Klima (DECK) simulations which include a preindustrial control, historical simulations, and idealized CO_2 forcing simulations (Golaz et al., 2019). A suite of atmospheric fields (e.g. net top-of-the-atmosphere radiation, surface air temperature, zonal winds, and precipitation) in the historical E3SMv1 simulations were compared against observations to calculate root-mean-square-errors (RMSEs). When compared to an ensemble of 45 CMIP Phase 5 (CMIP5) models, E3SMv1's RMSEs were generally found to have lower errors than the median of the CMIP5 ensemble, and for many fields and seasons, in the lowest (best) quantile. There are however, known biases in E3SMv1 which are common to other GCMs, such as a reduction in cloudiness over the subtropical stratocumulus regions and the well-known double Intertropical Convergence Zone (double-ITCZ) issue where there is excessive southern central Pacific precipitation (X. Zhang et al., 2007; Golaz et al., 2019).

Evaluating E3SMv1 for ARs, which has not yet been done, is necessary given our need to understand issues surrounding the water cycle and its interactions with humans and other Earth systems. This paper aims to provide an overview of ARs simulated in E3SMv1 by: i) comparing against historical ARs detected in MERRA-2 (Modern Era Retrospective analysis for Research and Applications, version 2) to identify AR biases, ii) evaluating internal model AR variability using individual ensemble members, and iii) determining the large-scale and model sources of AR biases. ARs in this study are detected using the AR algorithm developed by Guan and Waliser, 2019 which is a widely used algorithm and has been demonstrated to closely match key AR characteristics from direct airborne observations (Guan et al., 2018). The structure of this paper is as follows. In Section 3.2, E3SMv1, the reanalysis data set, and the AR detection algorithm are described. AR frequency, characteristics, precipitation, and large-scale conditions in E3SMv1 are compared to MERRA2 in Section 3.3. Discussion and conclusions are presented in Section 3.4. Appendix material are contained in Section B.

3.2 Data and Methods

3.2.1 Exascale Energy Earth System Model

E3SMv1 was developed from the Community Earth System Model (CESM1) (Leung et al., 2020). This study uses global, daily mean data from the standard 1° x 1° resolution (also referred to as the 'low' resolution), fully-coupled E3SMv1 model (Golaz et al., 2019). We use 35 years (1980-2014) from the historical simulation which incorporates several historical, observed forcings including atmospheric composition changes. Five ensemble members of historical simulations are available from E3SMv1 in the CMIP6 archive; these five members use initial conditions from the preindustrial control run, branched out at 50 year intervals, beginning with January 1st of year 101. The ensemble members are used in this study to examine internal variability related to ARs and to generate ensemble mean frequencies of ARs. The E3SM Atmosphere Model (EAM) (Rasch et al., 2019), which was developed from the Community Atmosphere Model version 5 (CAM5), uses a spectral element dynamical

core and is applied at a horizontal resolution of approximately 110 km (or 1° x 1°; 180 latitude grids x 360 longitude grids) and has 72 vertical levels. The historical runs follow the CMIP6 protocols outlined in Eyring et al., 2016. To understand the sources of model biases in simulating ARs, we also analyze atmosphere-only simulations for comparison with the fully-coupled historical simulations as has been done in previous studies to identify sources of errors (e.g. Li and Xie, 2012; Li and Xie, 2014). The atmosphere-only simulations follow the Atmospheric Model Intercomparison Project (AMIP) protocol and are part of the CMIP6 DECK simulations. All three available AMIP ensemble members are used in this study and atmosphere and land initial conditions for these ensemble members were taken at year 1870 from the first three historical ensemble members. The AMIP simulations have prescribed SSTs and sea ice concentrations from observations. A full overview of E3SMv1 and EAM can be found in Golaz et al., 2019 and Rasch et al., 2019 respectively. We will henceforth refer to E3SMv1 as E3SM. The fields obtained from E3SM are: total (vertically integrated) zonal/meridional water flux, total (convective and large-scale) precipitation rate (liquid + ice), total (vertically integrated) precipitable water, zonal wind at 200 hPa, and geopotential height at 500 hPa.

3.2.2 Reanalysis Data Set

In this study, daily mean reanalysis data from MERRA2 (Gelaro et al., 2017) is analyzed for the same 35 year period as E3SM (1980-2014). The native spatial resolution is ∼50 km (or 0.5° x 0.625°; 361 latitude grids x 576 longitude grids) but was re-gridded to match E3SM to facilitate comparison. MERRA2 is an updated version of MERRA (version 1) which was developed to improve representations of the global water cycle. Good agreement between MERRA2 against airborne and satellite observations has been previously demonstrated for ARs (F. Ralph et al., 2012; Guan et al., 2018). In additon, MERRA2 has been used extensively in previous AR studies (e.g. Shields et al., 2018a; Rutz et al., 2019). The fields obtained from MERRA2 are the same as those obtained from E3SM but can correspond to different long names: eastward/northward flux of atmospheric water vapor, total precipitation, atmosphere water vapor content, eastward wind at 200 hPa, and geopotential height at 500 hPa.

3.2.3 AR Detection Algorithm

ARs are detected using tARget v3 - the latest version of a widely used algorithm developed for global studies. Details of the detection algorithm can be found in Guan and Waliser, 2015, Guan et al., 2018, and Guan and Waliser, 2019. This algorithm is part of the Atmospheric River Tracking Method Intercomparison Project (ARTMIP) (Shields et al., 2018a) and is among the relatively 'permissive' algorithms compared to other algorithms to facilitate global analyses including inland-penetrating ARs as well as polar ARs, but meanwhile effective in filtering out non-AR features in the tropics. While there is significant uncertainty associated with the choice of detection algorithm (Shields et al., 2018a; Shields et al.,

2019; T. A. O'Brien et al., 2020; Rutz et al., 2019), we choose to use this algorithm for its global applicability and make no attempt in this study to quantify the uncertainty as this is a primary goal of ARTMIP. The algorithm, when applied to contemporary reanalysis products, detected ARs that were found to closely match airborne observations in terms of key characteristics such as AR width and total IVT across AR width (Guan et al., 2018). Various refinements and improvements have been made to the algorithm since it was first introduced in Guan and Waliser, 2015 to its current version. As a brief summary, the algorithm extracts contiguous areas of connected gridpoints based on IVT exceeding location- and season-specific IVT thresholds set at the 85th percentile of the dataset analyzed but cannot go below 100 kg m^{-1} s^{-1}. Geometric and directional requirements are then applied to the identified objects, with considerations on: direction of object-mean IVT (poleward component >50 kg m^{-1} s^{-1}), coherence of IVT directions (more than half of the area having an IVT direction within 45° from the object-mean IVT), length (>2000 km) and length/width ratio (>2) (Guan and Waliser, 2019). The IVT threshold is calculated separately for MERRA2 and the E3SM simulations. We include the annual mean 85th percentile IVT of both along with the differences in Section B Fig. B.2. In general, E3SM has higher threshold IVT values than MERRA2 with some regional biases up to 100 kg m^{-1} s^{-1}. Notably, these high positive IVT bias regions are over the subtropical jet in the northern hemisphere (which we discuss throughout the paper) and the midlatitude jet in the southern hemisphere where there are known warm sea surface temperature biases (Golaz et al., 2019) and associated enhanced atmospheric moisture (not shown).

3.3 Results

3.3.1 AR Frequency

We begin with the global distribution of AR frequencies shown in Fig. 3.1. These frequencies represent the ensemble mean from 5 historical simulations for E3SM compared to MERRA2; the AR detection algorithm was applied to each ensemble member individually to calculate the ensemble mean. For each grid cell, the frequency shown represents the number of timesteps the grid cell was part of an AR divided by the total number of timesteps in the time period. This is done for the annual, extended boreal winter (NDJFM), and extended boreal summer (MJJAS). The distribution of the annual frequency of ARs in E3SM closely matches MERRA2's distribution as seen in Fig. 3.1a and 3.1b. In E3SM, as in MERRA2, frequency maxima are found in the extratropics over the Pacific, Atlantic, and south Indian ocean basins while minima can be seen along the equator, at high polar latitudes, and over both Greenland and the Tibetan Plateau. The difference of E3SM minus MERRA2 annual frequencies is shown in Fig. 3.1c. To note, in the annual (seasonal), one percent of absolute difference translates to 3.65 (∼1.5) timesteps of AR difference out of 365 (151-153) timesteps in a year (extended season). All percentage differences mentioned below, unless otherwise noted, are absolute differences, not relative differences. We include the relative differences

of regions with absolute AR frequencies of at least 3 % in Section B Fig. B.2. Overall in E3SM, there are no to weak biases ($<$1 % absolute differences) over the AR frequency maxima regions which translate to correspondingly low relative biases. Positive biases of higher magnitudes (1-3 %) are seen near the edge of the tropics and subtropics in both northern and southern hemispheres. E3SM also has positive biases in polar areas, specifically over Alaska, Siberia, and just offshore of Antarctica. These absolute AR frequency differences translate to relative differences of up to 60 % along the subtropical edge of the Pacific, over India, over the polar areas near Alaska, and off the Antarctic coast (Fig. B.2c). These relative differences, while large, are over regions with annual AR frequencies of 5 % or less (with the exception of Alaska) where AR activity is expected to be particularly sensitive to large-scale conditions and we explore contributing factors to these biases, particularly to the Pacific storm track region, in Section 3.3.4. Negative biases (1-2 %) are seen in the southern hemisphere subtropics (southwestern region of Australia and over the south Atlantic east of Brazil). Between E3SM (ensemble mean) and MERRA2, the annual frequency mean absolute error (MAE) is 0.60 % and the correlation is 0.98 showing strong agreement in the distribution and magnitude of global AR frequencies.

For the NDJFM, E3SM (Fig. 3.1d) has AR frequency maxima and minima over regions matching MERRA2 (Fig. 3.1e) but there are areas with seasonal biases (Fig. 3.1f). ARs are most frequent over the subtropics and midlatitudes over the north and south Pacific and Atlantic where the storm tracks are located. One of the biggest sources of positive biases comes from north Pacific ARs affecting the entire west coast of North America with frequencies around 3-4 % higher than in MERRA2. The relative differences in this region can reach up to 30-50 % (Fig. B.2a) and lead us to investigate biases of the north Pacific subtropical jet in E3SM compared to MERRA2 in Section 3.3.4. These positive biases stretch from Mexico to Alaska nearly uninterrupted as well as nearly all the way across the subtropical north Pacific basin. Other positive biases exist over South America (originating from the Amazon Rainforest) and over India near the Himalayas with high relative differences ($>$50 %). Negative anomalies of $\sim$1-2 % are seen throughout the southern hemisphere ocean basins as well as over northern Africa and east of Japan. The NDJFM frequency MAE is 0.72 % and the correlation is 0.98.

The MJJAS frequencies in E3SM (Fig. 3.1g), similar to NDJFM frequencies, have maxima and minima co-located with MERRA2's MJJAS frequencies (Fig. 3.1h) but, again, with some biases (Fig. 3.1i). Frequency maxima can be seen in both E3SM and MERRA2 over the western areas of the north Pacific and north Atlantic basins and over the south Pacific and south Atlantic in the subtropics and midlatitudes. Positive biases are seen for E3SM in the following areas: the southern edge of the tropics near 15° S with the exception of the negative frequency bias over South America, the Middle East, the western boundary of the north Pacific, windward side of the Andes, and offshore of the Antarctic. The regions where these absolute differences translate to large relative differences are around 15° S (exceeding 100 % at the tropical edges), over the Arabian Sea (25-60 %), and off the shore of Antarctica (exceeding 100 % closer to shore). Negative biases are overall weaker and are found over South America on the leeward side of the Andes (between $\sim$10-20° S), the Caribbean Sea,
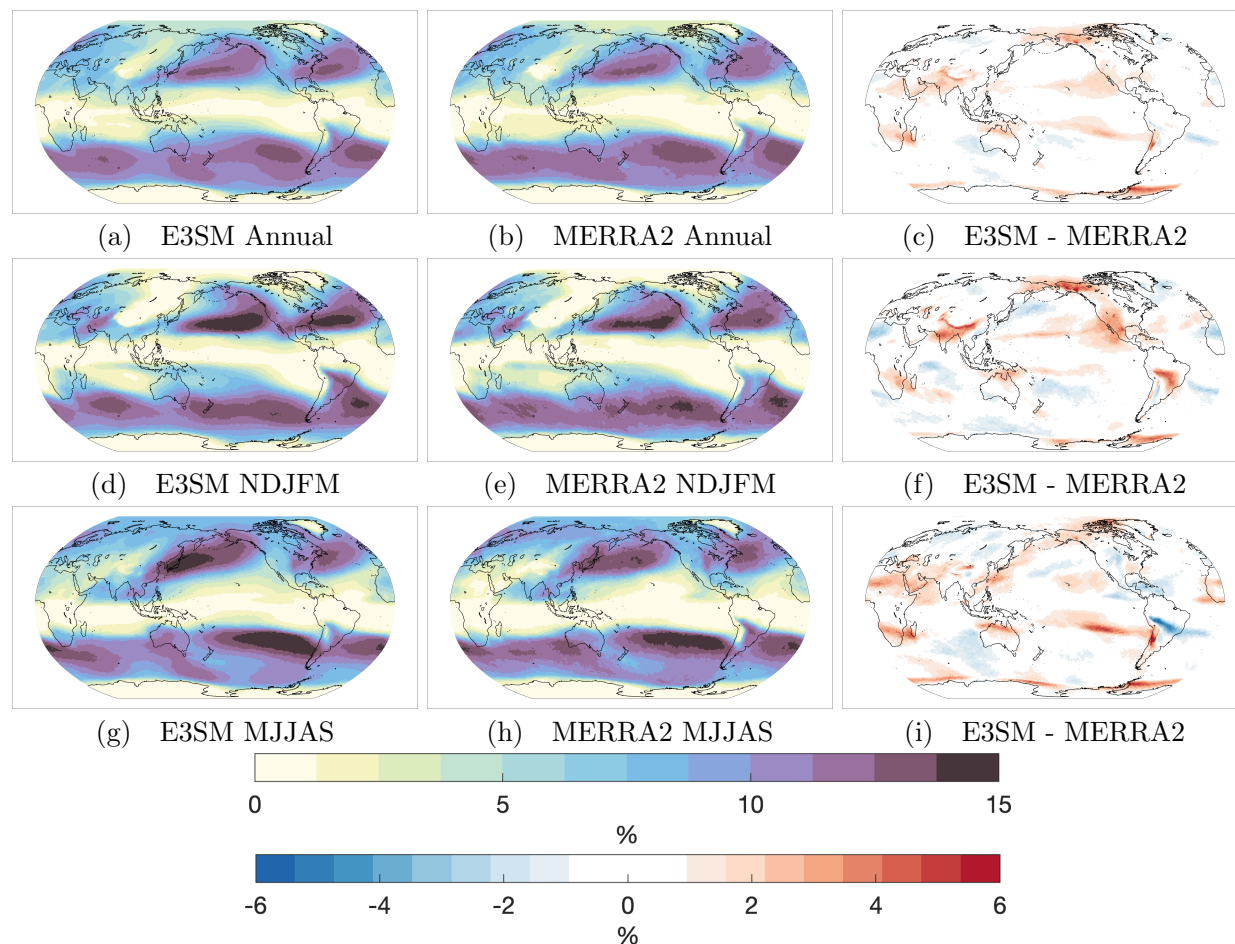
Figure 3.1: The AR frequency at each grid point globally for the annual (top row), extended winter NDJFM (middle row), and extended summer MJJAS (bottom row). E3SMv1 frequencies (left column), MERRA2 frequencies (middle column), and the difference in frequencies between E3SMv1 and MERRA2 (right column). The colorbar on the top (bottom) corresponds to the absolute (difference in) frequencies.

south Indian Ocean, and at mid and polar latitudes over Eurasia. The MJJAS frequency MAE is 0.82 % and the correlation is 0.97.

To summarize, E3SM and MERRA2 AR frequencies show very high correlation (>=0.97) and low mean absolute errors (<1 %) annually and seasonally. The magnitude and distribution of annual and seasonal AR frequencies are consistent with previous studies examining ARs in reanalyses (e.g. Guan and Waliser, 2015; DeFlorio et al., 2019). However, in E3SM, the hemisphere experiencing winter (especially the northern hemisphere) tends to produce positive frequency biases, and corresponding large relative differences, throughout the border of the tropics and subtropics (∼25° N and ∼15° S). The northern hemisphere summer

features notable positive anomalies throughout the tropics/subtropics over the Middle East and along the western boundary of the north Pacific. Additionally, AR frequencies are higher near some elevated topography (such as the Himalayas, the Alaska range, and Antarctica).

While the previous results are based on the 5-member ensemble mean, we next determine how well the individual historical E3SM ensemble members are able to match MERRA2's AR frequencies using Taylor diagrams (Fig. 3.2). Taylor diagrams provide a graphical summary of similarity between two patterns using pattern correlation, centered root-mean-square difference (RMSD), and standard deviation (SD). The Taylor diagrams confirm E3SM's ability to accurately simulate present day AR frequencies globally, across ensemble members, in the annual and seasonal with a high degree of similarity to MERRA2. Correlations are above 0.95 for all ensemble members and for the three periods analyzed (NDJFM, MJJAS, and annual) with the annual having the highest correlation. E3SM SDs are consistent with MERRA2's SD; all ensemble members, for all periods, are within 0.18 % of MERRA2. RMSDs in the annual are under 1.0 % while in the seasonal periods, are under 1.5 %. The diagrams also suggest that the internal variability of E3SM historical simulations is small - particularly in the annual - as the 5 ensemble members are tightly clustered.

As a measure of ensemble spread, the 5-member ensemble SD (different than the Taylor Diagram SD) of AR frequency - i.e. how much variance there is between the individual simulations and the ensemble mean - is shown in Fig. 3.3. For the annual (Fig. 3.3c), much of the global SDs are below 0.5 %. A few regions, such as over east and southeast Asia, the Arabian Sea, and the Hudson Bay, have SDs that fall between 0.5 % and 1.0 %. Analysis of the coefficient of variation (not shown), calculated at each grid globally as the ratio between ensemble AR frequency SD and mean ensemble frequency, shows that the annual SDs are well below 10 % of the ensemble mean AR frequencies for virtually all grid points barring a few grid points over the equator and Antarctica where ARs are very rare (annual frequencies are <1.0 %).

During NDJFM (Fig. 3.3a), SDs are generally higher in the northern hemisphere and have notable peaks of ∼1.5 % over east Asia (which is a jet entrance region) and the north Pacific storm track region. These regional peaks suggest that differences in subtropical jet behavior during NDJFM between the 5 historical simulations may be responsible for some of the internal AR frequency variability. MJJAS SDs (Fig. 3.3b) have maxima of ∼1.5 % over various regions of the Asia summer monsoon - the Arabian Sea, over the Philippines, and east Asia. This suggests that during MJJAS, differences in monsoon, MJO, or subtropical jet behavior may drive AR frequency variability between various E3SM ensemble members. In general, the northern hemisphere shows more internal variability; likely due to both internal interannual and interdecadal variability of the midlatitude circulation in the region and especially in the north Pacific.

3.3.2 AR Characteristics

Next, we examine several AR characteristics in E3SM (using a single historical simulation) and MERRA2. These characteristics are provided by the AR detection algorithm's output
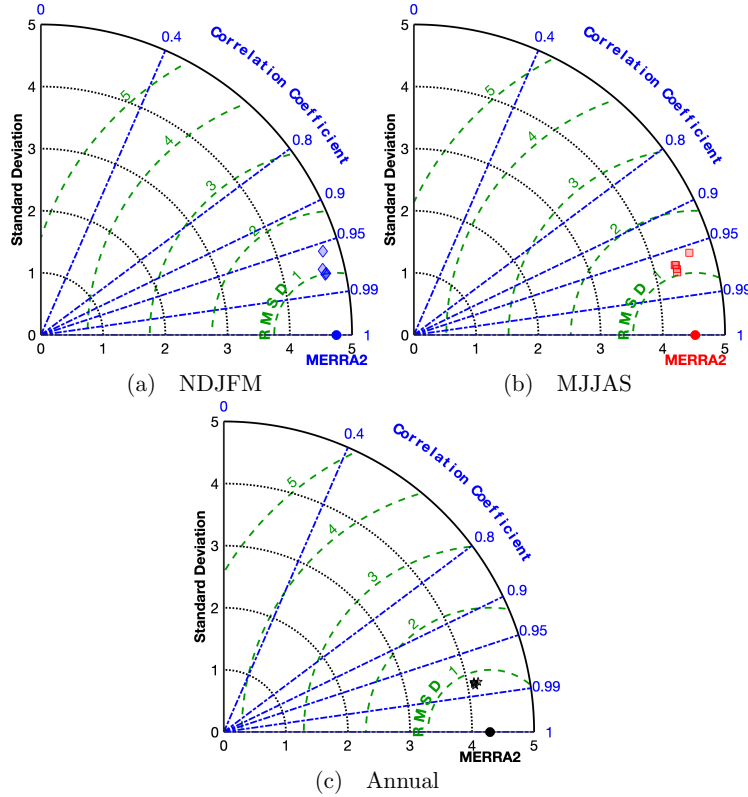
Figure 3.2: Taylor diagrams of AR frequency for the 5-ensemble historical E3SM members against MERRA2 for (a) NDJFM, (b) MJJAS, and (c) annual. The MERRA2 point is labeled in each graph.

for each individual AR. The distributions for the various AR characteristics are shown in Fig. 3.4. All characteristics show strong similarities in the distribution shape and peak in probability at the same bin values aside from magnitude of mean IVT (Fig. 3.4e).

The length (Fig. 3.4a) and width (Fig. 3.4b) distributions of ARs in E3SM are generally consistent with MERRA2 as well as with previous characterizations of AR geometry (e.g. Guan and Waliser, 2015; Guan et al., 2018). The median length and width of ARs in E3SM are ~3 % longer (3501 km compared to 3397 km) and wider (658 km compared to 639 km) than in MERRA2. The E3SM AR length/width ratio distribution and median (Fig. 3.4c) are in good agreement with MERRA2.

The hemispheric median centroid latitude of ARs is consistent, but the distributions reveal that E3SM produces more ARs with centroid latitudes in the tropics, subtropics, and southern polar latitudes while producing fewer ARs in the midlatitudes compared to MERRA2 (Fig. 3.4d). These results are supported by the frequency differences in Fig.3.1.

The median magnitude of mean IVT of ARs in E3SM is 10.6 % larger than MERRA2 (Fig. 3.4e). The distribution of ARs peaks at 500 kg m^{-1} s^{-1} for E3SM but peaks at weaker

(a)   NDJFM   (b)   MJJAS
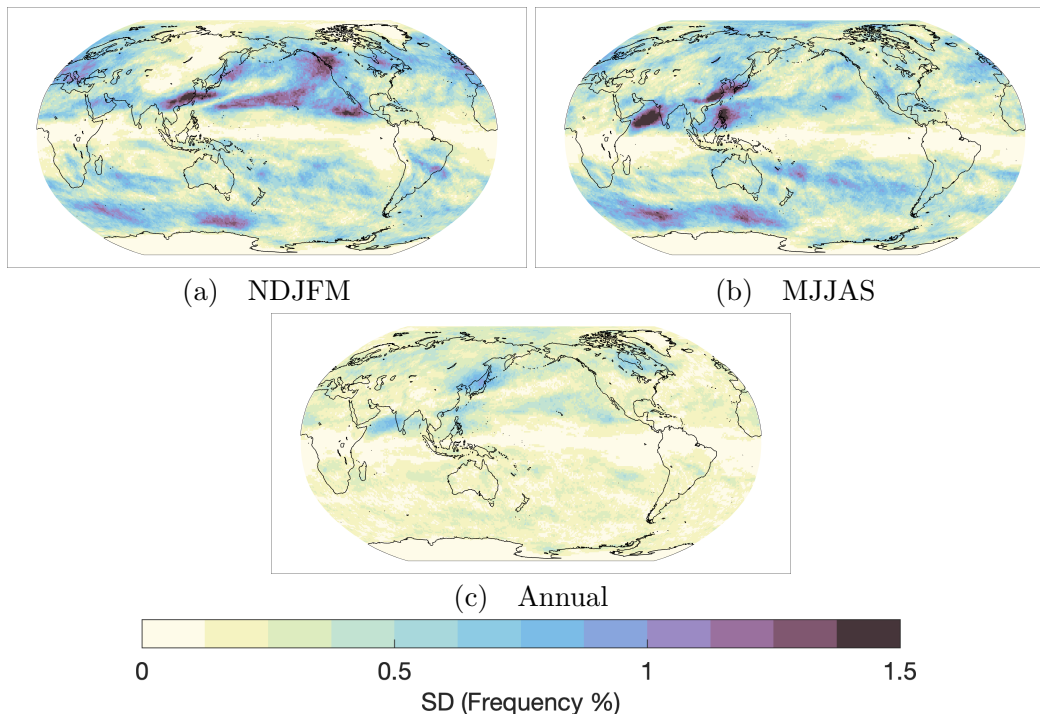
(c)   Annual

Figure 3.3: The historical E3SM 5-member ensemble standard deviation of AR frequencies
for (a) winter, (b) summer, and (c) annual.

magnitudes around $350 \, \text{kg m}^{-1} \, \text{s}^{-1}$ for MERRA2. These distribution differences reflect E3SM's
positive IVT biases (Fig. B.1c) in regions of high AR activity.

The direction of mean IVT ($0°$ for IVT directed to the north) in the northern hemisphere
is directed towards the northeast (median angle of $65°$ and $62°$ for E3SM and MERRA2
respectively) and in the southern hemisphere, is directed towards the southeast (median
angle of $120°$ and $123°$ for E3SM and MERRA2 respectively) (Fig. 3.4f). E3SM ARs have
higher probabilities around $90°$ (indicating a mean IVT direction directed to the east) and
around $270°$ (indicated a mean IVT direction directed to the west). These median values,
along with the distributions, indicate that E3SM ARs tend to have mean IVTs directed
slightly more zonally compared to MERRA2. Coherence of IVT directions within an AR
is calculated as the fraction of AR grid cells with IVT directed within $45°$ of the mean AR
IVT (Guan and Waliser, 2015). Model and reanalysis show similarly high coherences of 0.99
(E3SM) and 0.98 (MERRA2) (Fig. 3.4g).

3.3.3   AR Precipitation

We now compare a variety of metrics related to AR precipitation. For reference, annual
precipitation - not just from ARs - is included (Fig. 3.5a-c) for both models and reanalysis
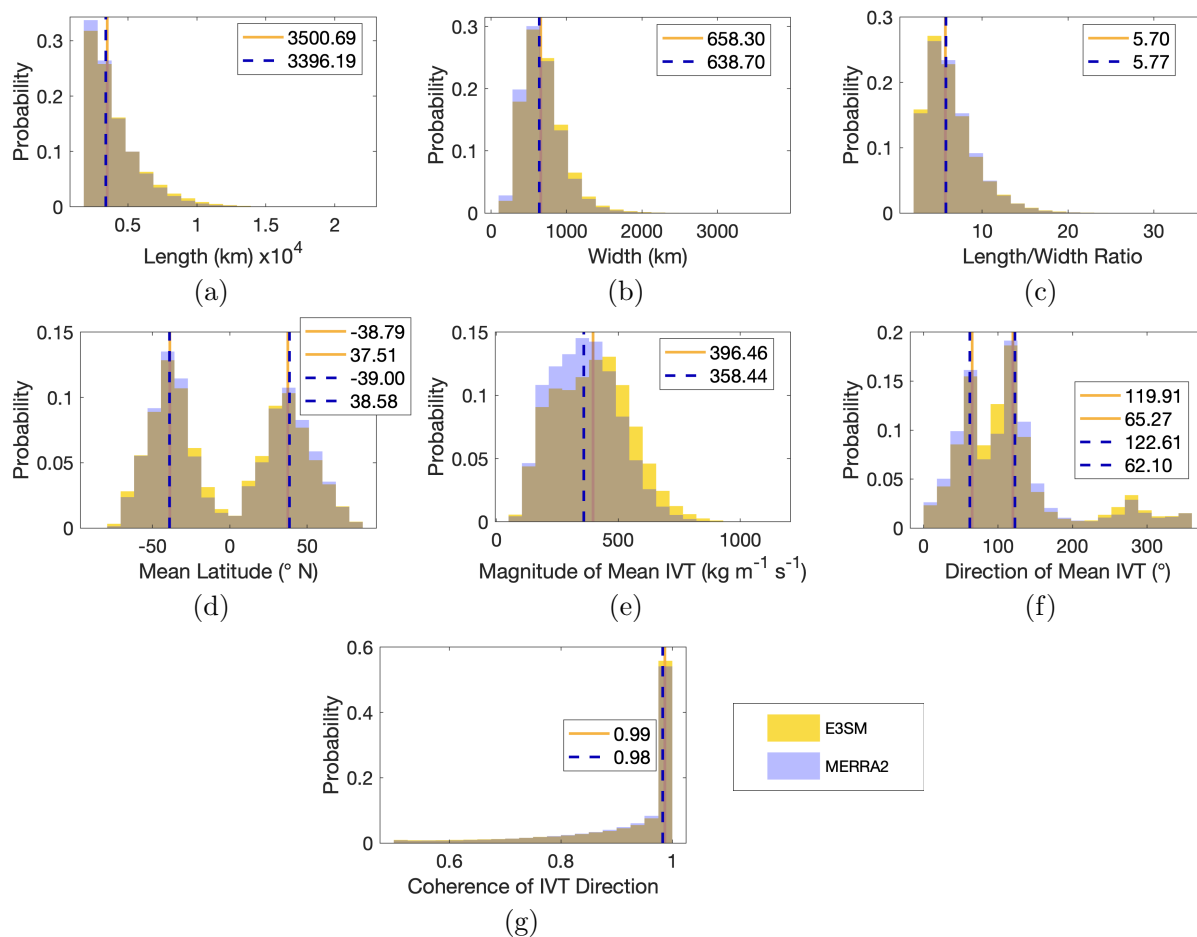
Figure 3.4: Distributions of a variety of AR characteristics in E3SM and MERRA2. The yellow bars and solid line (median) are for E3SM and the blue bars and dotted line (median) are for MERRA2. Two sets of lines indicate hemispheric median values.

along with the differences. In this study, AR precipitation is defined as the precipitation that falls within an AR boundary.

For annual AR precipitation rates (Fig. 3.5d-f), E3SM is able to simulate the general global distribution and magnitude of AR precipitation characterized in previous studies using Global Precipitation Climatology Project version 1.2, (e.g. Guan and Waliser, 2015; F. M. Ralph, Dettinger, Rutz, et al., 2020a) as well as with MERRA2, but with some differences. E3SM has higher AR precipitation estimates over significant portions of the tropics and subtropics but lower estimates along the equator (Fig. 3.5f) largely reflecting the pattern of general precipitation biases (Fig. 3.5c). The western coasts of North and South America also have higher rates of AR precipitation in E3SM. The seasonal differences in AR precipitation for the NDJFM and MJJAS are largely consistent to the annual differences. We also

include mean annual total precipitation (mm/yr) for E3SM, MERRA2, and their difference (Fig. B.3) to show how AR precipitation rate biases translate into yearly quantities. AR precipitation rate biases are important contributors to precipitation totals for regions outside of the tropics where ARs occur more frequently.

Next, we examine the percentage of precipitation attributed to ARs in both datasets annually (Fig. 3.6). ARs can be responsible for over 30 % of the annual precipitation in the expected extratropical areas such as the west coast of North and South America. Some other areas of note with high AR precipitation fractions include east Asia, the Middle East, southeastern U.S., Greenland, and Australia. These areas of high AR precipitation fractions have been characterized in previous studies (Guan and Waliser, 2015; F. M. Ralph, Dettinger, Rutz, et al., 2020a). The precipitation fraction differences, shown in Fig. 3.6c, reveal that E3SM does, however, attribute a higher fraction of precipitation to ARs (up to 20 %) off the coast of southwestern U.S./Mexico and Chile. There is also a strong band of higher AR fractions (exceeding 20 %) extending from the Sahel/Sahara region of Africa eastward to India. In addition, the polar regions exhibit higher AR fractions. Some midlatitude regions attribute less precipitation to ARs in E3SM, particularly over the southern hemisphere oceans. As expected, areas of higher AR precipitation fraction tend to be co-located with areas of positive AR frequency biases. Exceptions are northeast Africa, the Arctic, and over the Amazon - all regions with low annual AR frequency biases; this suggests a small number of AR events are shifting the AR fractions in these locations.

Globally and annually, ARs are responsible for 17.84 % and 17.95 % of precipitation in E3SM and MERRA2 respectively. Interestingly, while the overall precipitation percentage is very consistent, the fraction of AR precipitation that falls over ocean and land vary between the two datasets. In E3SM, 17.38 % (82.62 %) of the AR precipitation falls over land (oceans) while in MERRA2, only 14.81 % (85.19 %) falls over land (oceans). Topographic features seem to be able to extract precipitation from AR events more effectively in E3SM compared to MERRA2 - also evidenced by Fig. 3.5f.

3.3.4 Large-scale AR Conditions

In this section, we look into the sources of the E3SM AR frequency and precipitation biases by examining the large-scale conditions relevant to ARs. We begin with the AR precipitation biases in the fully-coupled E3SM simulations. The E3SM AR precipitation biases (Fig. 3.5f) are mostly well co-located and of similar magnitude with the general precipitation biases present in E3SM (Fig. 3.5c). While this reflects the important contributions of AR precipitation to the total precipitation in some regions, it also suggests that the AR precipitation and total precipitation biases can share similar sources of large-scale circulation biases. For example, model biases in the subtropical jet could affect precipitation produced by AR and non-AR storms, as both are influenced by the jet and storm tracks (Shields and Kiehl, 2016; W. Zhang and Villarini, 2018; Wahl et al., 2019; F. M. Ralph, Dettinger, Rutz, et al., 2020a). Two notable exceptions where there are positive AR precipitation biases but no equivalent general precipitation biases are i) off the coast of the U.S. southwest and ii) the
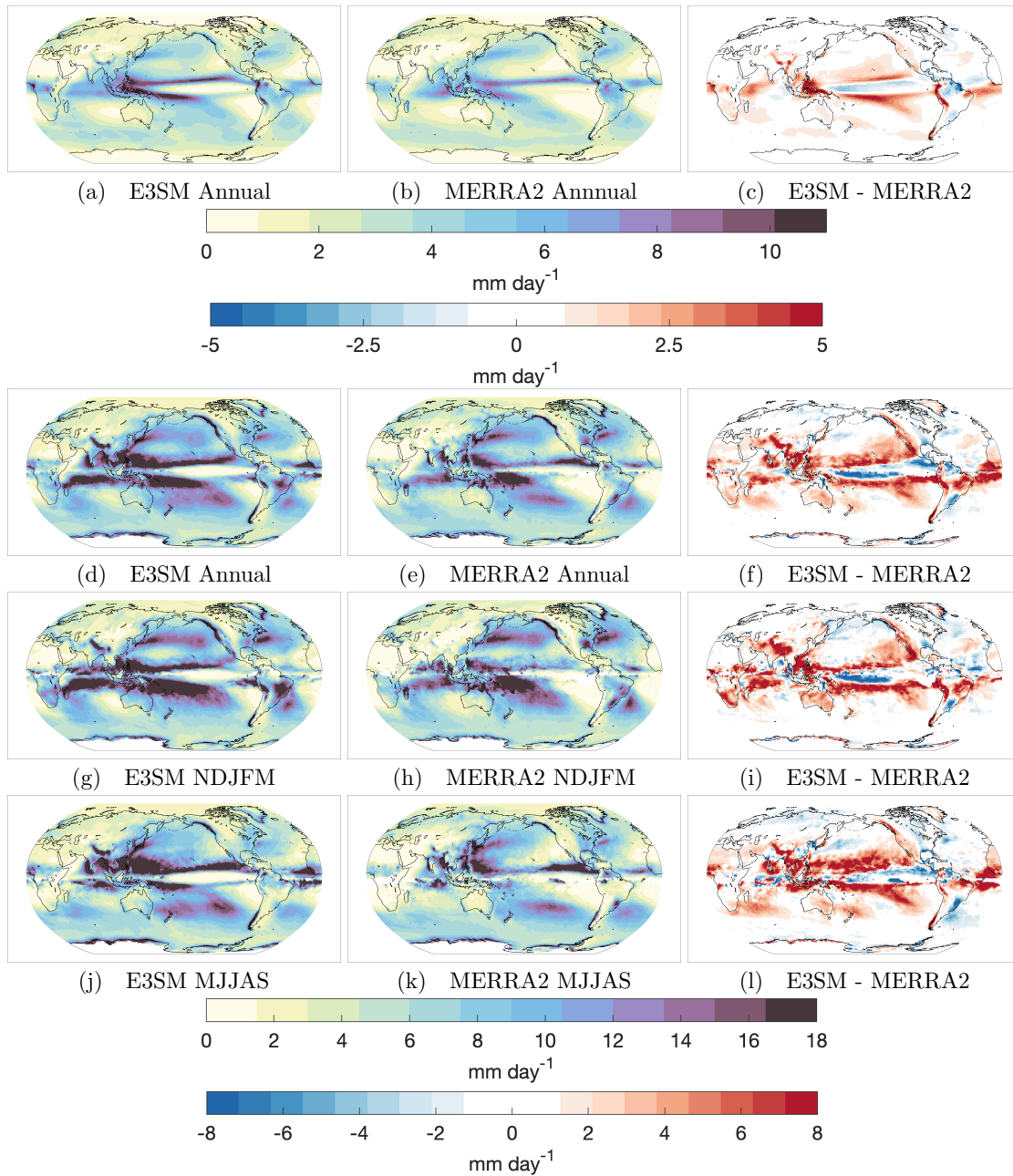
Figure 3.5: Top row shows annual precipitation in E3SM, MERRA2, and the difference. The next three rows are organized as in Fig. 3.1 but for AR precipitation instead of AR frequency. The colorbar on the top (bottom) corresponds to the absolute (difference in) precipitation or AR precipitation.

(a)   E3SM AR Precipitation %   (b)   MERRA2 AR Precipitation %
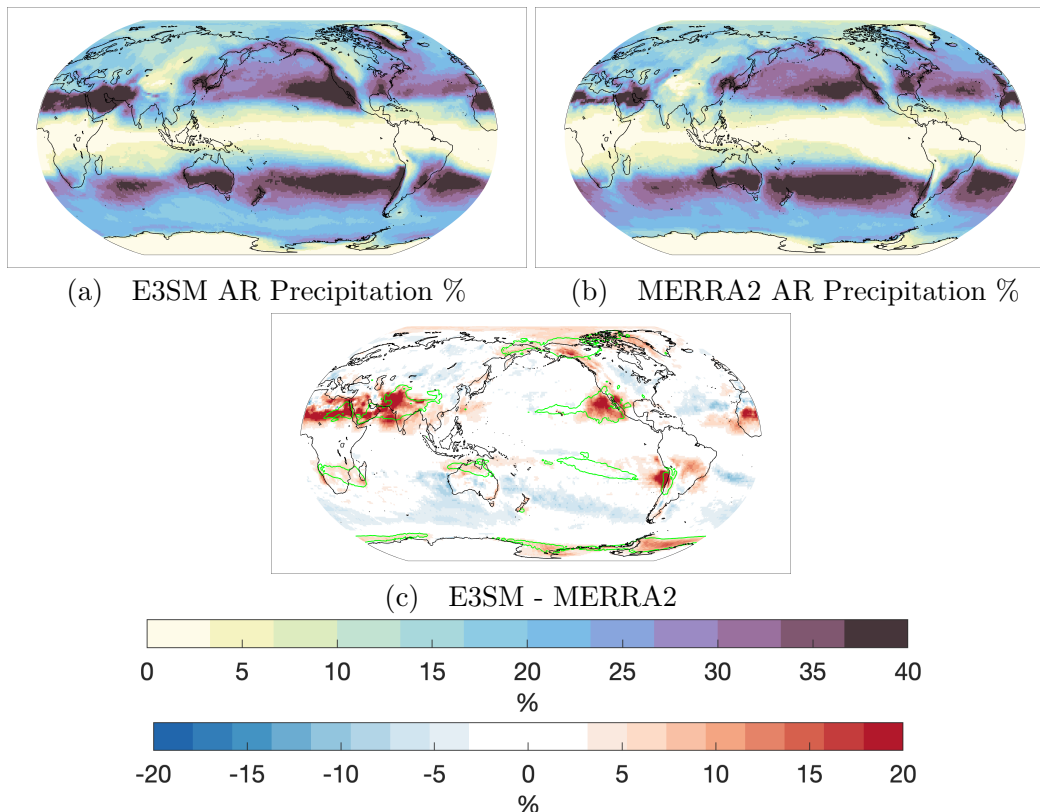
(c)   E3SM - MERRA2

Figure 3.6: The fraction of annual precipitation attributed to ARs for each grid cell for (a) E3SM and (b) MERRA2. The difference (E3SM minus MERRA2) is shown in (c). The colorbar on the top (bottom) corresponds to the absolute (difference) percentages. Contour lines in (c) indicate the 1.5 % positive AR frequency biases from Fig. 3.1c.

region around Pakistan/India. These are the same regions in E3SM, compared to MERRA2, that attribute a higher fraction of the annual precipitation to ARs (Fig. 3.6), partly due to positive AR frequency biases. This suggests certain large-scale circulation biases in these regions have a larger influence on AR frequency and intensity than the frequency/intensity of non-AR storms leading to a larger fraction of annual precipitation being delivered in the form of AR events rather than non-AR storms.

A large source of general E3SM precipitation biases come from known and common biases in fully-coupled simulations - the double-ITCZ bias and excessive precipitation over the maritime continent (Golaz et al., 2019). Related to the double-ITCZ, Dong et al., 2021 investigated models with this bias and found that models which feature a present-day double-ITCZ bias tend to exhibit an excessively wet U.S. southwest and understate the drying over the Mediterranean basin in global warming projections. The former on the U.S. southwest wetting is due to these interconnected relationships: under global warming, models with
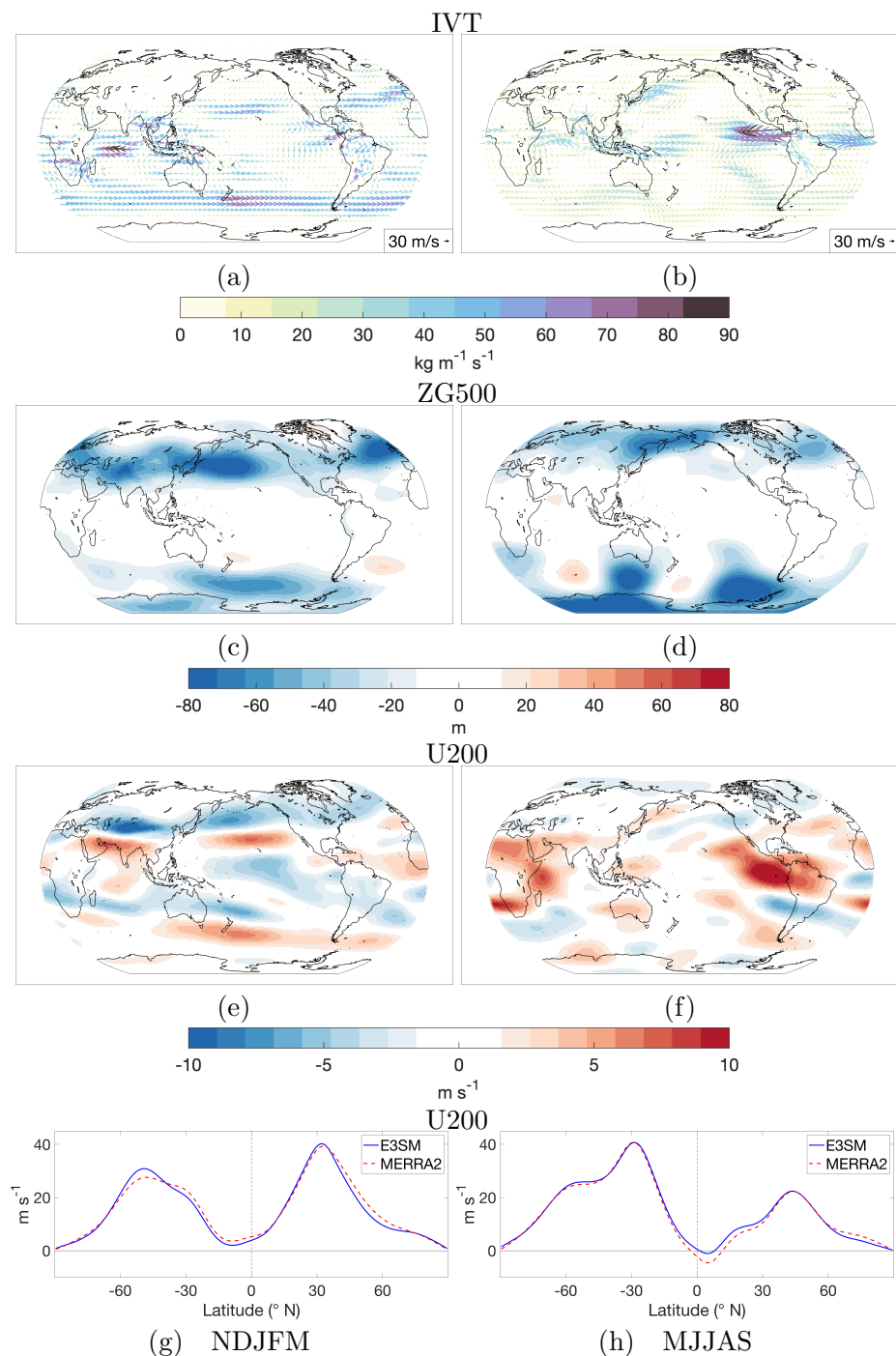
Figure 3.7: Seasonal differences between E3SM and MERRA2 (from top row to bottom row): IVT, geopotential height at 500 hPa, zonal wind at 200 hPa, and zonal means over the Pacific and Atlantic basins (100-360° E) of zonal wind at 200 hPa.

double-ITCZ bias feature enhanced central Pacific rainfall as a wet-get-wetter response, which increases the upper-tropospheric heating in the Pacific subtropics and the meridional temperature gradients, resulting in an accelerated upper-level north Pacific subtropical jet and a deepened and southeastward shifted Aleutian low, both leading to increased precipitation in the U.S. southwest. The latter on the Mediterranean basin drying is a result of future changes stemming from a present day weaker Atlantic Meridional Overturning Circulation (AMOC) that is energetically related to the double-ITCZ and models with weaker AMOC in the historical simulations tend to simulate a weaker AMOC response to warming. Given the double-ITCZ bias in E3SM, an analogy may be drawn between the implications of the double-ITCZ bias on the precipitation response to warming (i.e., difference between future and historical simulations) discussed by Dong et al., 2021 and the implications of the double-ITCZ bias on the precipitation bias in the historical simulations (i.e., difference between E3SM simulations and MERRA2), which is our focus. More specifically, we focus on if and how the aforementioned processes related to a double-ITCZ bias (stronger subtropical jet and weaker AMOC) influence AR biases in E3SM while also noting other large-scale biases.

In our study, the U.S. southwest and neighboring areas in E3SM feature positive AR biases during the NDJFM period (Fig. 3.1f). Although Dong et al., 2021 looked at future projections of large-scale circulation and precipitation changes, we find similarities to the above features in the large-scale circulation and precipitation biases which can explain the sources of some of the AR biases; the same processes arising from the double-ITCZ in future simulations can occur in present day simulations, although, the wet-get-wetter response for the future simulations likely enhances the effect. Over the central north Pacific, we find E3SM features a stronger, southward shifted north Pacific jet (Fig. 3.7e and 3.7g) and deepened geopotential heights during the winter compared to MERRA2 (Fig. 3.7c). These circulation biases are consistent with the double-ITCZ bias in E3SM through the aforementioned interconnected processes and contribute to enhanced moisture transport (Fig. 3.7a) and thus positive AR biases on the southern flank of the north Pacific storm track and landfalling regions (U.S. southwest). The coastal U.S. southwest also features an area of enhanced atmospheric moisture (not shown) which is likely a result of an underestimation of west coast, subtropical stratocumulus clouds (Golaz et al., 2019 Fig. 4c) leading to increased downward radiation and thus increased evaporation and moisture. While most of the stronger positive moisture transport anomalies are directed towards the U.S. west coast, the central Pacific low geopotential height anomalies also support weaker enhanced transport to Alaska/Siberia - an area of positive AR frequency bias. While the jet bias in the North Pacific may be partly explained by the double-ITCZ bias in E3SM, biases in the subtropical jet are also noticeable in other regions that may or may not be related to the double-ITCZ. For example, over India, another area with positive AR frequency biases during NDJFM, the subtropical jet is similarly stronger and southward shifted compared to MERRA2. With the subtropical jet aimed more south of the Himalayas and the Tibetan plateau, an enhanced trough develops over Central Asia (Fig. 3.7c) which weakens the offshore winter monsoon and generates positive moisture transport anomalies onshore during the winter (Fig. 3.7a).

During MJJAS, the austral winter, the southern hemisphere subtropical jet is slightly stronger and shifted equatorward (Fig. 3.7f and 3.7h). This strengthening and equatorward displacement is not as strong nor as coherent as the northern hemisphere jet shift. The strengthening and/or shift is most apparent around 20° S which is just south of the positive AR frequency biases over Australia, the south Pacific, and southern Africa (Fig. 3.1i). Moisture transport anomalies (Fig. 3.7b) at these locations are poleward and westerly; they are supported by low geopotential height anomalies to their south (Fig. 3.7d). For the northern hemisphere MJJAS, the westerlies in general are enhanced in E3SM equatorward of about 40° N until the tropics. In contrast to the NDJFM response, the MJJAS upper-level winds are strengthened over the north Atlantic stretching east all the way to east Asia. Over the northwestern Pacific, there are positive AR frequencies along the western boundary of the Pacific basin - a region associated with East Asian summer rainband. Enhanced summertime westerlies across the Tibetan plateau have been linked to an intensified pre-Meiyu rainband resulting from increased meridional stationary eddy circulation and moisture convergence downstream of the Tibetan Plateau in east Asia (Chiang et al., 2019). The E3SM anomalies show strengthened westerlies over the Tibetan Plateau along with increased moisture convergence east of the Tibetan Plateau and increased transport poleward at the location of the east Asian rainband. The enhanced transports reach up to Alaska, supported by the low geopotential height anomalies over Siberia and Alaska. Another region with positive AR anomalies is the Arabian Peninsula. Moisture flux anomalies over this region seem to be due, in part, to a weakened Somali Jet and redirected Indian monsoon moisture. The positive geopotential height anomaly in the Arabian Sea supports moisture transports towards the Arabian Peninsula.

Annually, regardless of the season (although stronger during MJJAS), Antarctica features positive biases just offshore. We find the E3SM southern hemisphere polar jet to exhibit more meridional movement than MERRA2 during MJJAS (Fig. 3.7f). This enhances the southwesterly moisture transports (Fig. 3.7b) towards Antarctica on the eastern side of the low anomalies. The same geopotential height anomalies that support the subtropical AR biases are also responsible for this variable jet movement. Additionally, Golaz et al., 2019 also reports fully-coupled historical simulation Southern Ocean net radiation to be higher and SSTs to be ∼2 degrees C higher than observations. We find higher atmospheric moisture in the southern hemisphere (up to 2 kg m^{-2}; not shown) from the subtropics to Antarctica given this warm SST bias during both seasons. Together, these biases may contribute to the higher AR frequencies near the Antarctic coast.

From examining the major AR biases and large-scale conditions in E3SM regionally and seasonally in the previous sections, we find these features to be most significant: i) the double-ITCZ bias, ii) a stronger and/or equatorward shifted subtropical jet during boreal and austral winter, and iii) stronger westerlies during the northern hemisphere summer. As previously mentioned, Dong et al., 2021 found that models with a double-ITCZ and associated wetting in the equatorial central Pacific to feature an enhanced subtropical jet and weaker mean-state AMOC under global warming. The large-scale anomalies we have uncovered suggest that the double-ITCZ bias in E3SM may play a large role in some large-scale circulation
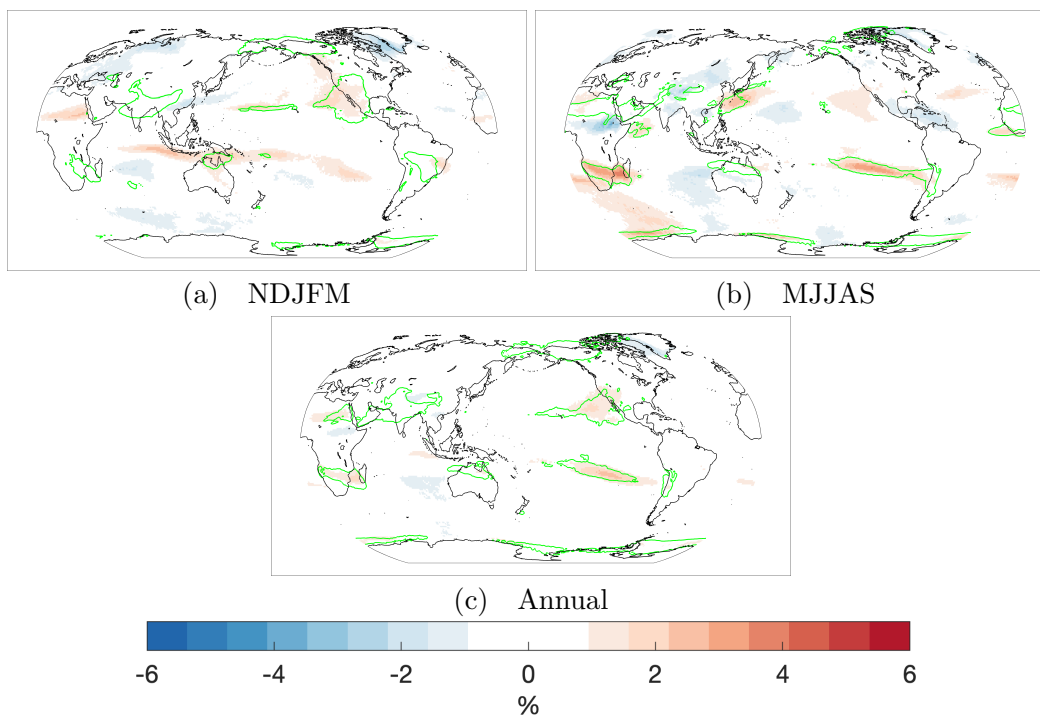
Figure 3.8: Historical ensemble (5 members) mean AR frequencies minus AMIP ensemble (3 members) mean AR frequencies. Contour lines for the seasonal and annual indicate the 2 % and 1.5 % positive AR frequency biases respectively from the corresponding biases in Fig. 3.1c, f, and i.

biases such as the subtropical jet bias in North Pacific that contribute to the E3SM AR biases. We look for further evidence by isolating biases in the atmospheric model using the AMIP (Atmospheric Model Intercomposion Project) simulations and comparing them to the fully-coupled model for ARs. While atmospheric models may exhibit weak double-ITCZ biases, such biases are severely exacerbated in fully-coupled models (G. J. Zhang et al., 2019). This holds true for E3SM as can be seen in Golaz et al., 2019 Fig. 6b and 6c where the fully-coupled simulation has a far stronger double-ITCZ bias. Thus, by comparing AMIP and coupled simulations we can determine which biases are common to both simulations - implicating the EAM - or unique to the fully-coupled, historical simulation - implicating a coupling response (specifically the double-ITCZ response) or other components (e.g. the ocean component or sea ice).

We first compare the ensemble AR frequencies. The AMIP ensemble consists of 3 members (compared to the 5 members for the fully-coupled ensemble). For context, the AMIP frequencies have slightly better correlations and MAEs (as expected) than the fully-coupled ensemble when compared to MERRA2 (e.g. annual ensemble frequency correlation is improved from 0.98 to 0.99 and annual MAE is improved from 0.60 % to 0.54 %). In Fig. 3.8, we

subtract the AMIP ensemble frequencies from the fully-coupled ensemble frequencies. Common biases to both ensemble simulations - i.e. regions in Fig. 3.8 without fully-coupled minus AMIP biases (shading) but with fully-coupled minus MERRA2 biases (contours) - are the positive AR biases near elevated topography, India/Arabian Peninsula, central South America, southeastern Africa, and Alaska/Siberia. This suggests that these biases likely arise from the EAM. Golaz et al., 2019 reported that both AMIP and the fully-coupled historical simulations have excessive precipitation over elevated terrain as well as other precipitation biases.

We also identify several biases that are unique to the fully-coupled simulations. Compared to AMIP, the fully-coupled simulations have positive AR frequency biases (∼3 %) over the Pacific basin and over Africa at subtropical latitudes during the winter season of each hemisphere suggesting that the wintertime subtropical jet is affected going from AMIP to fully-coupled simulations - particularly on the equatorward flank. During NDJFM, the southwest region of the U.S. and the central north Pacific are zones of enhanced AR frequencies. This is an aforementioned area where the double-ITCZ bias response in models deliver excessive moisture (Dong et al., 2021). For the southern hemisphere, positive AR frequencies are co-located with the double-ITCZ precipitation biases (see Fig. 3.5c). During MJJAS, the major biases are over the summer rainband region of east Asia, southern Africa, and the eastern subtropical Pacific in the southern hemisphere. Given the AR biases over the subtropics in the fully-coupled simulation compared to the AMIP simulation, we now examine the changes in the behavior of the subtropical jet between these two simulations.

In Fig. 3.9, we compare upper-level zonal winds (zonal wind at 200 hPa) globally for NDJFM and MJJAS. During NDJFM in the northern hemisphere, positive upper-level zonal wind anomalies in the fully-coupled simulation (Fig. 3.9a) generally match in location to the anomalies of E3SM compared to MERRA2 (Fig. 3.7e) while the negative anomalies, particularly over Asia, are weaker. This would suggest that coupling in E3SM is a major source of a stronger, slightly equatorward shifted, boreal winter subtropical jet. The zonal mean zonal winds (zonally averaged over the Pacific and Atlantic basin) show similar equatorward shifts when comparing the fully-coupled simulation to both MERRA2 and AMIP (Fig. 3.7g and Fig. 3.9c). The southern hemisphere differences are generally consistent with MERRA2 differences from the equator to the subtropics but the midlatitudes to the polar latitudes lack the southward shifted, enhanced westerlies over the southern ocean/Australia. The enhanced westerlies over this region are a bias common to both fully-coupled and AMIP simulations implicating the EAM.

The global MJJAS zonal wind (200 hPa) anomalies between the fully-coupled and AMIP simulations qualitatively matches the MJJAS anomalies when comparing to MERRA2 for most regions. A notable feature is the clear strengthening and southward shift of the subtropical jet seen over subtropical latitudes over much of the northern hemisphere - particularly from north Africa moving east to the Pacific basin. The enhanced westerlies over the Tibetan Plateau again correspond with increased AR activity downstream over the east Asian summer rainband region. West of and over southern Africa there is a band of enhanced westerlies in the fully-coupled simulation when comparing to both MERRA2 and AMIP (Fig.
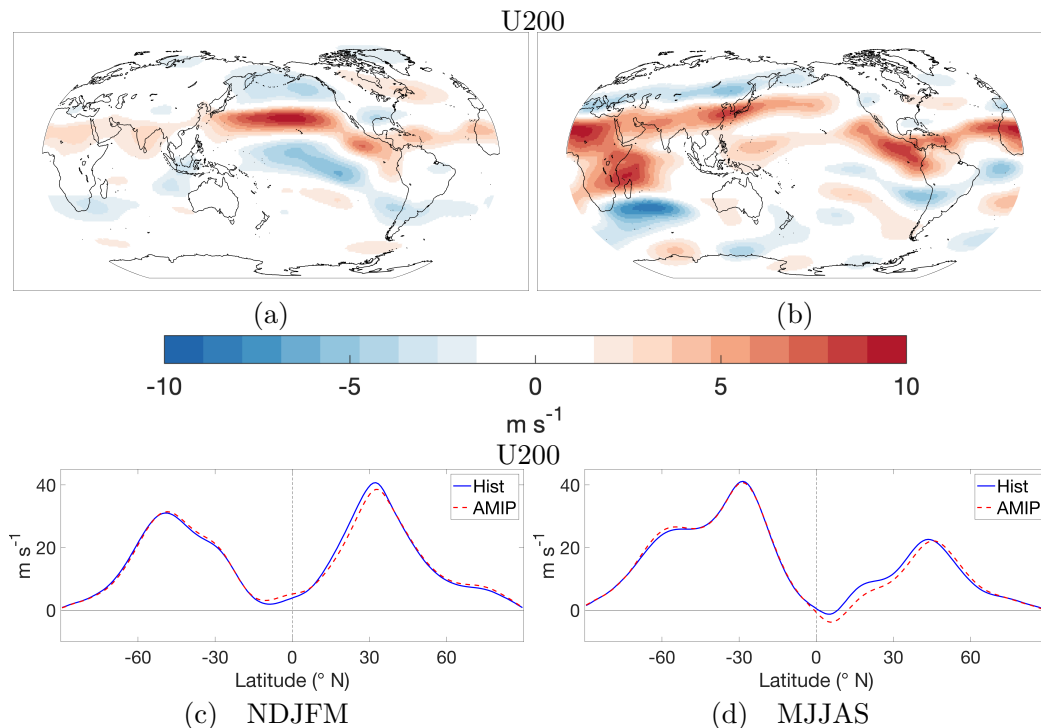
Figure 3.9: Seasonal differences between E3SM fully-coupled and AMIP: zonal wind at 200 hPa (top row) and zonal means over the Pacific and Atlantic basins (100-360° E) of zonal wind at 200 hPa (bottom row).

3.7f and Fig. 3.9b). For both of these regions, the evidence points to the biases arising from coupling.

Lastly, we explore what physically causes the jet behavior shifts between fully-coupled and AMIP simulations. For NDJFM, the most significant change is a strengthening of the subtropical jet over the north Pacific and for MJJAS, the enhanced westerlies throughout much of the northern hemisphere. Building off the work of Dong et al., 2021, the two significant responses to a double-ITCZ bias that the authors uncovered in models are a strengthened subtropical Pacific jet in projections and a weaker mean-state AMOC in present day. We look for evidence that these responses occur for E3SM going from the AMIP to the fully-coupled simulation using upper-troposphere (500-200 hPa) temperatures differences (Fig. 3.10). Dong et al., 2021 found that due to the double-ITCZ, enhanced precipitation over the southern Central Pacific generated subtropical changes induced by latent heat release. This leads to enhanced upper-tropospheric warming over the subtropics (Dong et al., 2021 Fig. 2b), which increases the meridional temperature gradient locally, accelerating the subtropical jet along with a southeastward shift of the Aleutian low in projections. We find a similar upper-tropospheric response in temperature over the North Pacific (Fig. 3.10a); a striking patch of warming occurs in the same area of the subtropical north Pacific with a correspond-

ing cool patch to the north. This enhances the north Pacific wintertime subtropical jet as seen in Fig. 3.7g.

Dong et al., 2021 also find evidence of weaker present-day AMOC in models with a double-ITCZ bias. While the authors focus on the implications for winter precipitation projections over the Mediterranean basin, in this study we examine whether a weaker mean state AMOC can enhance MJJAS westerlies. The MJJAS response is clearly different than that of the NDJFM response. Fig. 3.10b reveals widespread cold anomalies throughout the northern hemisphere contrasted with some warm anomalies throughout the southern hemisphere. The strongest cold anomalies are concentrated in a subtropical/midlatitude band over north Africa stretching east to east Asia. The strong upper-troposphere cold anomalies at these latitudes increase the meridional temperature gradient supporting an accelerated summertime subtropical jet. In fact, the band of cold anomalies sits just north of the enhanced subtropical jet anomalies over Africa, Europe, and Asia (Fig. 3.9b). The hemispheric temperature contrast of a warm southern hemisphere and a cold northern hemisphere is suggestive of a weaker AMOC (W. Liu et al., 2020); a weaker AMOC would deliver less cross-equatorial heat to the northern hemisphere causing the northern hemisphere to be cooler. The weaker AMOC and the double-ITCZ are related as a double-ITCZ attempts to counteract less northward heat transport with increased northward heat transport via a stronger southern hemisphere ITCZ (G. J. Zhang et al., 2019).

We also examine the surface air temperature to verify a weaker AMOC in the fully-coupled simulation. Specifically, we look for the classic AMOC "fingerprint" which consists primarily of a strong cold temperature anomaly over the subpolar Atlantic Ocean and to a lesser degree as a warm temperature anomaly over the Gulf Stream (Caesar et al., 2018). In Fig. B.4, we show surface temperature differences between the fully-coupled and AMIP simulations and find the AMOC "fingerprint" well defined along with a hemispheric contrast in temperature. W. Liu et al., 2020 isolated the global surface air temperature response to a weakened AMOC and find widespread northern hemisphere cooling and more modest southern hemisphere warming (W. Liu et al., 2020 Fig. 2E). This is consistent with Golaz et al., 2019 and A. Hu et al., 2020, both of which reported a weaker AMOC calculated directly from the ocean model output in the fully-coupled E3SM simulation when compared to observations.

3.4   Conclusions

In this study, we have evaluated E3SM v1.0 at standard resolution for its ability to simulate ARs globally. We compared the fully-coupled historical simulation to MERRA2 and began with an examination of global AR frequencies. We find that E3SM is able simulate ARs with very high degrees of correlation and low MAEs annually (annual correlation 0.98; MAE 0.60 %) and seasonally (NDJFM correlation 0.98; MAE 0.72 %; MJJAS correlation 0.97; MAE 0.82 %). Amongst historical ensemble members, we determined that the internal variability of AR frequencies is low with the 5-member SD under 0.5 % for nearly all grid points. There

Upper troposphere (500-200 hPa) temperature difference

(a)   NDJFM   (b)   MJJAS
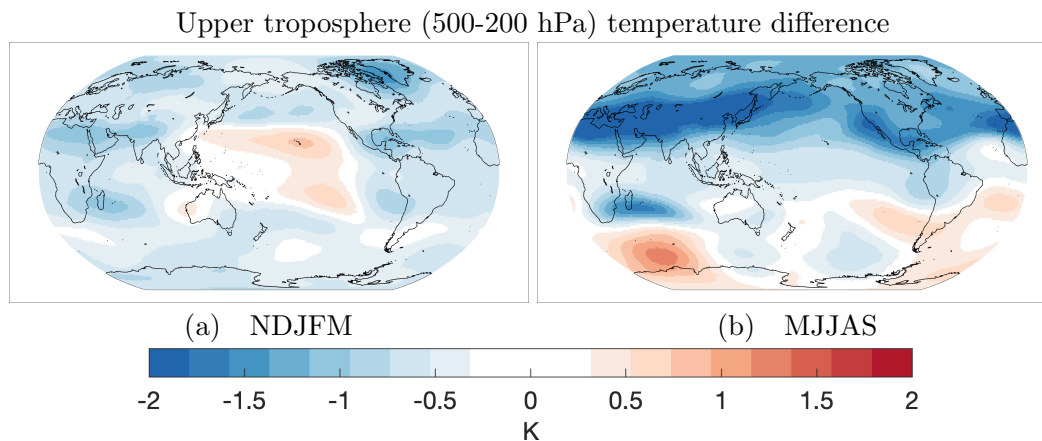
Figure 3.10: Seasonal differences between the fully-coupled E3SM and AMIP simulation for upper troposphere (500-200 hPa) temperature.

are however, some biases (most notable when looking at relative differences) such as: i) positive biases occurring near the tropic/subtropic edge during both northern and southern hemisphere winters, ii) enhanced AR activity over the Middle East, India, and the western boundary of the north Pacific basin during boreal summer, and iii) on the windward side of elevated terrain (e.g. Tibetan Plateau). AR characteristics are compared using probability distributions and we find the E3SM AR characteristics are generally consistent (shape and peak) with MERRA2. Some differences are that the median magnitude of mean AR IVT is higher and ARs tend to be slightly more zonal in E3SM. The generally higher IVT and stronger westerly jets in E3SM are likely the source of both characteristic differences. While a comprehensive comparison of AR representation in other models (such as those in CMIP5/6) has not yet been done, the expectation is that E3SM would compare favorably against other models as E3SM outperforms other models in simulating global and regional climate features (Golaz et al., 2019).

E3SM distributions of AR precipitation show good agreement with MERRA2 although there is a clear bias resembling the double-ITCZ bias and excessive maritime continent precipitation. This manifests as reduced AR precipitation along the equatorial Pacific and excessive AR precipitation just off the equator in the double-ITCZ regions. AR precipitation fractions reveal a bias in E3SM to attribute excessive precipitation just off coast of the western U.S. and western Chile as well as over the region near northern Africa/the Middle East/India.

An examination of the large-scale conditions relevant to ARs in E3SM reveals these features to be most significant in producing AR biases in E3SM: i) the double-ITCZ bias, ii) a stronger and/or equatorward shifted subtropical jet during boreal and austral winter, and iii) enhanced westerlies during the northern hemisphere summer. The work of Dong et al., 2021 showed there is a significant relationship in models with a present-day double-ITCZ

bias to have a stronger projected north Pacific subtropical jet as well as a weaker present day AMOC. Given the clear double-ITCZ bias in the fully-coupled E3SM, we investigated whether the interconnected processes of the North Pacific jet, Aleutian low, and AMOC with a double-ITCZ were present in the E3SM historical simulation and if they could explain AR biases. Analysis of the E3SM large-scale circulation biases identified biases in the subtropical jet during both NDJFM and MJJAS that could contribute to the AR precipitation biases. The strengthened and slightly equatorward-shifted North Pacific jet and the impact on AR precipitation in the U.S. Southwest is consistent with the signature identified by Dong et al., 2021 as related to the double-ITCZ during winter.

Motivated by the analysis of large-scale circulation biases and their general correspondence with the AR precipitation bias, we further compared the fully-coupled (strong double-ITCZ bias) and AMIP simulations (no to weak double-ITCZ bias) to isolate the changes that occur when moving from an atmosphere-only model to a fully-coupled model while specifically looking for evidence of a stronger subtropical jet and weaker AMOC. The analysis suggests that the AR frequency biases over elevated terrain, India/Arabian Peninsula, central South America, and Alaska/Siberia can be attributed to the EAM, as similar biases are found in both AMIP and coupled simulations. Biases arising from coupling or other model components include the positive AR frequencies over the north Pacific subtropics and U.S. southwest region during NDJFM and over the east Asia summer rainband region and the southern hemisphere eastern subtropical Pacific during MJJAS. These coupling biases suggest that the model responses to a double-ITCZ revealed in Dong et al., 2021 could be the source even in present-day simulations. We show evidence that the physical processes leading to a stronger north Pacific subtropical jet during NDJFM and enhanced northern hemisphere westerlies during MJJAS are consistent with Dong et al., 2021. The north Pacific subtropical jet is enhanced via increased, upper-troposphere temperature gradients generated through teleconnections induced by enhanced heat release in the equatorial Pacific Ocean related to the double-ITCZ.

On the other hand, the enhanced northern hemisphere westerlies during summer are due to a band of strong cold anomalies in the upper-troposphere stretching east from north Africa to east Asia. The upper-troposphere temperature differences reveal a hemispheric temperature contrast with a cool northern hemisphere and warm southern hemisphere bias - suggestive of a weaker AMOC. We find that the fully-coupled simulation does indeed have a weaker mean state AMOC evidenced by the AMOC "fingerprint" in surface temperature comparisons, which is consistent with the weak AMOC reported by Golaz et al., 2019 and A. Hu et al., 2020 based on analysis of the ocean circulation in the coupled simulations.

We note, however, that the cold bias in the northern hemisphere and the opposite bias in the southern hemisphere may also be contributed by the strong model response to aerosol forcings, as found by Golaz et al., 2019. Aerosol forcing is strongest over the northern hemisphere midlatitudes (Hansen et al., 1998; Ma et al., 2012; Friedman et al., 2013) during spring through summer and during MJJAS is indeed when we see the strongest signal in cold anomalies. Another contributing factor for the interhemispheric temperature contrast could be from the delayed warming - related to E3SM's strong aerosol forcing - in the cou-

pled historical simulation between 1960-1990 which keeps the global surface air temperature lower than observations until about 2010. The long period of delayed warming could reduce the interhemispheric temperature asymmetry signal from climate change which has amplified warming of the northern hemisphere (Friedman et al., 2013). The cool northern and warm southern hemisphere bias in the coupled E3SM simulation may also explain why the northern MJJAS hemisphere jet strengthening and shift is more significant than the southern hemisphere as the upper-level temperature gradients are increased and decreased over the subtropical latitudes for the North and South hemispheres respectively. More generally, biases in the subtropical jet in E3SM may be contributed by other sources of model biases besides the double-ITCZ and related weak AMOC. Future analysis including the high resolution E3SM simulation (Caldwell et al., 2019) may offer additional insights on AR and large-scale circulation biases, as AMOC is noticeably stronger at high resolution compared to the low resolution simulations analyzed here.

3.5 Acknowledgements

Chapter 4

Atmospheric River Core Structure Impacting Landfall Precipitation

4.1   Introduction

Atmospheric rivers (ARs) are responsible for transporting the majority of water vapor that crosses the mid-latitudes towards the poles and have significant regional impacts for society and environment (Zhu and Newell, 1998). When ARs make landfall, they can bring both beneficial and detrimental impacts to regions such as the western U.S.. One of the most significant dangers associated with ARs is extreme precipitation and flooding (F. M. Ralph et al., 2019) and we see evidence of these dangers already increasing in our warming climate (Michaelis et al., 2022).

A fundamental variable related to ARs is integrated water vapor transport (IVT) - the combination of moisture and winds. This field, both the intensity and duration, is used extensively for the detection, characterization, and impacts of ARs (F. Ralph et al., 2013; F. M. Ralph, Dettinger, Rutz, et al., 2020b; F. M. Ralph et al., 2019). Several studies, such as Neiman et al., 2008, have found that moisture transport is closely related with mountain precipitation - high moisture transports are necessary for heavy precipitation. Another study, F. Ralph et al., 2013 found storm-total water vapor transport directed up mountain slopes contribute 74% of the variance in storm-total rainfall. For ARs, moist-neutral conditions allow moist air to rise without resistance over topography and produce orographic precipitation (F. M. Ralph et al., 2005). However, this relationship between IVT and precipitation has a dependence on other condition. The strongest correlations of IVT and precipitation have been found to maximize near the top of the topography (Neiman et al., 2002; Backes et al., 2015). Additionally, Neiman et al., 2002 found that altitude of the low-level jet of an AR produced the strongest enhancements of upslope moisture transport while Backes et al., 2015 showed the importance of mid level moisture transport for precipitation over elevated terrain. While IVT is a dominant control, these studies suggest there may be other smaller, yet significant controls on an AR's orographic precipitation such as the

height of topography and the vertical structure of moisture transport. Other studies have looked into the importance of landfalling orientation and trajectories but as of yet, there is a lack of studies that examine how differences in the vertical structure of an AR can affect precipitation.

Recent studies (Cobb, Michaelis, et al., 2021; Cobb, Delle Monache, et al., 2021) have used dropsondes to define and better understand the vertical structure of the different sectors (core, cold sector, and warm sector) and surrounding environment of ARs. Cobb, Michaelis, et al., 2021 used observations from 33 ARs and defined the core of an AR as having 80% of the maximum integrated vapor transport across each transect while the cold sector and warm sector are defined as the areas poleward and equatorward outside the core respectively with IVT values above 250 kg m^{-1} s^{-1}. Using these definitions, their study showed that there are distinct characteristics for each sector with differences in occurrence of low-level jets, stability, and moisture transport vertical profiles for example. The core of the AR was found to have the strongest windspeeds and IVT compared to the other sectors and were associated with a LLJ 49% of the time. By identifying the sectors of an AR, we can better understand AR structure and processes while also informing AR observational campaign strategies and improving forecast diagnostics and model evaluations (Cobb, Michaelis, et al., 2021).

Building upon this observational sector work and the lack of studies examining AR precipitation and vertical structure, we investigate how the structure of an AR core influences precipitation at landfall and focus specifically on the height of the moisture flux maximum which we define as the AR core height. In this preliminary study, we choose to focus on the core of ARs as they contain the most significant moisture flux and are well associated with low-level jets but we acknowledge both the CS and WS require their own analyses. Given that previous research has shown the low-level jet altitude of an AR determines the height of the strongest upslope flow and the relationship between upslope flow and precipitation are most strongly correlated near mountain tops, we hypothesize that AR core heights are important for landfalling precipitation over complex terrain. We are interested in evaluating whether landfalling precipitation depends on core height using MERRA2 (Modern Era Retrospective analysis for Research and Applications, version 2). However, we need to first be able to identify core heights in MERRA2, and confirm that MERRA2 is doing a good job with core characteristics. Cobb, Michaelis, et al., 2021 and Cobb, Delle Monache, et al., 2021 examined core vertical structure with dropsondes, which gives us an observational target to evaluate MERRA2 against. Thus, we explore and expand the above relationships in 41 winter seasons (DJF) of reanalysis data for the western U.S.. This preliminary study: i) describes a newly developed sector identification algorithm and compares the results to dropsonde observations in Cobb, Michaelis, et al., 2021, ii) uses the core sector of ARs to analyze characteristic differences - including precipitation impacts - that arise from differences in the height of the moisture flux maximum, iii) examines how different terrain heights interact with ARs, and iv) determines historical trends in AR core height. The structure of this paper is as follows. In Section 4.2, the reanalysis data set and the AR sector identification algorithm are described. In Section 4.3, the sector characteristics from the algorithm

are directly compared with the observation-based characteristics in Cobb, Michaelis, et al., 2021 and evaluated for 41 years of reanalysis data. The influence of the moisture flux maximum on landfalling precipitation and terrain interactions are also presented in this section. Discussion and conclusions are presented in Section 4.4.

4.2   Data and Methods

4.2.1   Reanalysis Data Set

For this study, 6-hourly reanalysis data from Modern Era Retrospective analysis for Research and Applications, version 2 (MERRA2) (Gelaro et al., 2017) is analyzed for the period of 1980-2020 (41 years total) over the winter season (DJF). We use the native spatial resolution which is $\sim$50 km (or 0.5° x 0.625°; 361 latitude grids x 576 longitude grids) and 42 vertical levels from 1000 hPa to 0.1 hPa (vertical levels are at 25 hPa intervals from 1000 - 700 hPa then change to 50 hPa intervals until 100 hPa). MERRA2 improves upon MERRA (version 1) with specific developments to better represent the global water cycle and previous studies have demonstrated good agreement between MERRA2 against airborne and satellite observations (F. Ralph et al., 2012; Guan et al., 2018). The fields used from MERRA2 are: zonal winds, meridional winds, specific humidity, bias corrected total precipitation, and eastward/northward flux of atmospheric water vapor. While ARs detected in MERRA2 (detection algorithm is described in the following section) were found to closely match airborne observations in terms of key characteristics such as AR width and total IVT across AR width (Guan et al., 2018), we note that Cobb, Delle Monache, et al., 2021 found MERRA2 to have negative IVT biases compared to dropsonde observations at low levels dominated by weak winds and positive IVT biases above 700 hPa due to humidity.

4.2.2   AR Detection Algorithm

The sector identification algorithm relies on the output of tARget v3 - a commonly used global AR detection algorithm. Details are described in Guan and Waliser, 2015, Guan et al., 2018, and Guan and Waliser, 2019 with the latter describing tARget v3. As this algorithm is part of the Atmospheric River Tracking Method Intercomparison Project (ARTMIP) (Shields et al., 2018a), it has been evaluated comprehensively against other detection algorithms and is known to be relatively 'permissive' compared to other algorithms. This facilitates and enables global analyses by capturing inland-penetrating ARs and high-latitude ARs which can have much weaker IVT signatures compared to midlatitude ARs over the ocean (Shields et al., 2018a; Shields et al., 2019; T. A. O'Brien et al., 2020; Rutz et al., 2019). Guan et al., 2018 demonstrated how the ARs detected with this algorithm (both for a subset case study of 21 ARs and a larger set of >6000 ARs) were found to closely match observations from aerial campaigns in terms of key characteristics - such as AR width and total IVT across AR width. Since it was first introduced in Guan and Waliser, 2015, various refinements

and improvements - such as lifecycle tracking of events, sequential IVT thresholds, removal
of circular features, AR axis, and more - have been made to the algorithm to its current
version. While details can be found in the aforementioned paper, we provide a brief summary
of the algorithm. Using location- and season-specific IVT thresholds (85th percentile or
higher of the dataset) with a minimum IVT requirement of 100 kg m^{-1} s^{-1}, contiguous areas
(connected gridpoints) are extracted. These areas must then meet additional geometric and
directional requirements such as length, length/width ratio, and coherence of IVT. As part
of the output of the tARget v3 algorithm, masks of each AR are provided along with AR
axis information which will be important for sector identification (next section). Guan and
Waliser, 2019 defines the AR axis by: "tapping the previously unused information in IVT
direction. In doing so, the pixel with the maximum IVT within the entire AR is first located
and registered as the central axis pixel. Going "downstream" from there according to the
overall IVT direction in a neighborhood centered around that pixel (i.e., the pixels within
500 km that collectively account for 25% or less area of the AR), the next axis pixel is found
by locating the pixel with the maximum IVT among the few immediately neighboring pixels
that are downstream (i.e., within 45° of the IVT direction described above) of the previous
axis pixel. The iteration goes on until reaching the boundary of the AR. The other half of
the axis is similarly found by going "upstream" from the central axis pixel." This algorithm
also outputs the landfall location of ARs which we utilize to determine which ARs make
landfall in the western U.S.

4.2.3   AR Sector Identification Algorithm

For our sector identification algorithm, we build upon the work of Cobb, Michaelis, et al.,
2021 who identified AR sectors using transects of dropsonde observations. While Cobb,
Michaelis, et al., 2021 utilized an observational dataset, we generalize the methods used to
identify sectors from dropsondes to any gridded reanalysis product or climate model output
and focus just on the core, cold sector (CS), and warm sector (WS) (Cobb, Michaelis, et al.,
2021 additionally identified non-AR cold sectors and non-AR warm sectors but we do not).
Our method relies on using the output of tARget v3 so as a first step, it is required to
run tARget v3 on the dataset first for AR identification. Utilizing the AR masks and AR
axis information from the tARget output along with IVT data, we describe the steps in
determining each of the three sectors using a sample AR. Only ARs from the north Pacific
(AR centroid crosses into the domain 30-45N, 200-240E at some point in its lifecycle) that
have lifetimes of at least 12 hours (at least three 6-hour timesteps) are considered in this
study. The mask of the sample is shown in Fig. 4.1a.

For the CS and WS identification, we first split the AR by removing the pixels associated
with the AR axis (described in Section 4.2.2, the AR axis is part of the output of tARget
v3). This produces an AR roughly split in half down its AR axis (Fig. 4.1b). Using these
two halves, we determine which half is more southeastern. We only consider the lower half
of the AR - as defined as the grid points south of the AR centroid (IVT-weighted) - and
calculate the mean latitude and longitude of each (Fig. 4.1c). Comparing these values to

(a)   tARget v3 AR sample mask   (b)   AR axis removed   (c)   Area below AR centroid

(d)   Cold and warm sectors   (e)   All sectors
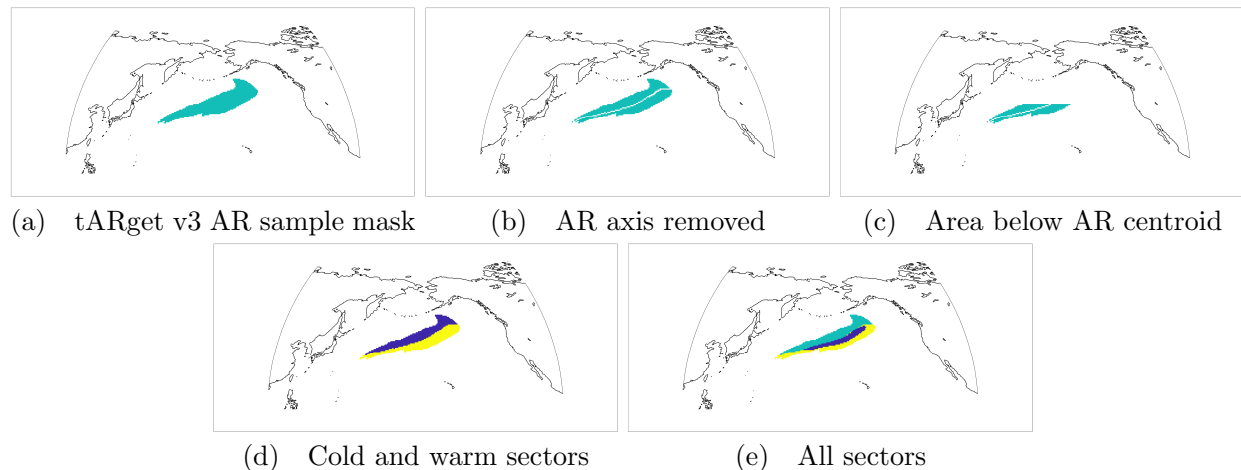
Figure 4.1: AR sector identification algorithm steps applied to a sample mask on MERRA2
Jan 26, 2000 00:00. Fig. 4.1e displays the core in dark blue, the cold sector in light blue,
and the warm sector in yellow.

the AR centroid, the half which is more southeastern is labeled as the WS while the other
northwestern half is labeled as the CS (Fig. 4.1d).

For the core identification, we begin by assessing the IVT values of all the grid points
that comprise of a given AR mask. The 80th percentile IVT (specific to the AR mask)
is calculated and all the AR grid points meeting or exceeding this threshold are identified.
From all of these high IVT grid points, we find the largest connected component and label
these as the core of the AR. Connected component in our study refers to 2-dimensional 4-
connected neighborhood (grid points are considered connected if there is at least one other
viable grid point directly up, down, left, or right of it.) The final result of assessing an AR
mask for its sectors is shown in Fig. 4.1e. An advantage of our geometric approach and IVT
thresholds that only rely on an individual event, is that it can be applied to ARs in any
climate scenario.

4.3   Results

4.3.1   Sector Characteristics Directly Compared to Observations

We first begin by evaluating the sector identification algorithm by directly comparing char-
acteristics of the identified core, CS, and WS sectors to the dropsonde observations of Cobb,
Michaelis, et al., 2021. In their study, wintertime AR dropsonde observations from 33 IOPs
(Intensive Observational Periods) from 2014-2020 (generally centered around 0000 UTC)
were evaluated. We ran the sector detection algorithm with the closest matching 6-hr
timestep in MERRA2 that corresponded with the time of each of the 33 IOPs in Cobb,

Michaelis, et al., 2021. Through manual verification, 3 IOP timesteps were not used due to the tARget v3 algorithm AR masks not corresponding to the AR observations and 1 timestep was not used for a sector mislabel.

(a)   Sector Identification Algorithm

(b)   Cobb et al. (2021b)
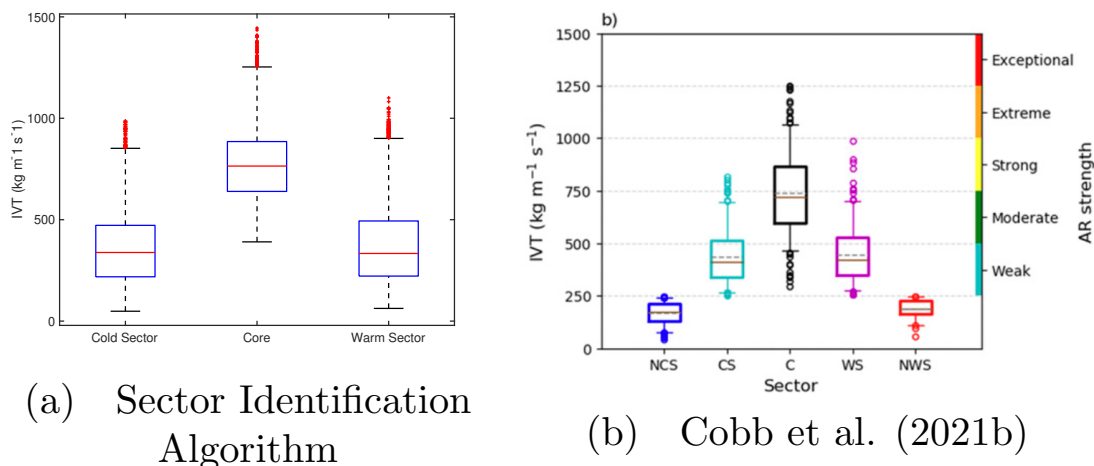
Figure 4.2: Box and whisker plots showing sector IVTs from ARs corresponding to the observations of Cobb, Michaelis, et al., 2021. The central red mark is the median, the box edges are the 25th and 75th percentile, and the red pluses are outliers defined as falling outside of 1.5 * interquartile range. The sector algorithm and Cobb, Michaelis, et al., 2021 results are shown in Fig. 4.2a and b respectively.

Fig. 4.2 shows the box and whisker plot of IVT from the output of the sector identification algorithm. Comparing to Fig. 3b of Cobb, Michaelis, et al., 2021, the medians are in good agreement for the AR core and are while for the CS and WS the values are lower. The box edges (25th and 75th percentile) are in agreement across all sectors. The core median IVT is 764 kg m^{-}1 s^{-}1 and the core mean IVT is 772 kg m^{-}1 s^{-}1 which is 32 kg m^{-}1 s^{-}1, or 4%, higher than in Cobb, Michaelis, et al., 2021. The CS (WS) median IVT is 338 kg m^{-}1 s^{-}1 (333 kg m^{-}1 s^{-}1) and the CS (WS) mean IVT is 358 kg m^{-}1 s^{-}1 (369 kg m^{-}1 s^{-}1) which is 78 kg m^{-}1 s^{-}1 (80 kg m^{-}1 s^{-}1), or 18% (18%), lower than in Cobb, Michaelis, et al., 2021. The CS having a slightly higher mean IVT than the WS is in agreement with Cobb, Michaelis, et al., 2021. However, the lower values in our study for the CS and WS are due to the fact that Cobb, Michaelis, et al., 2021 considered IVT values under 250 kg m^{-}1 s^{-}1 to be non-AR while the tARget v3 algorithm uses a location- and season-specific IVT thresholds. Examining the distribution of IVT values for the gridpoints in the CS and WS shows that there are values well under 250 kg m^{-}1 s^{-}1 which are considered part of the AR mask. For both the CS and WS, 32% of IVT gridpoints are under the 250 kg m^{-}1 s^{-}1 threshold. When removing the gridpoints below the threshold, the IVT means (relative differences) become 443 kg m^{-}1 s^{-}1 (1.6% higher) and 456 kg m^{-}1 s^{-}1 (1.5% higher) for

the CS and WS respectively which is in very good agreement with Cobb, Michaelis, et al.,
2021.

(a)   Moisture Flux Profile

(b)   Wind Speed Profile

(c)   Moisture Flux Profile

(d)   Wind Speed Profile

Figure 4.3: Vertical profiles of a) moisture flux and b) windspeed from ARs corresponding to
the observations of Cobb, Michaelis, et al., 2021. c) and d) are moisture flux and windspeed
from Cobb, Michaelis, et al., 2021.

We next examine how the vertical profiles of IVT and windspeed (Fig. 4.3) compare
to Cobb, Michaelis, et al., 2021 Fig. 13a and Fig. 4a. The structure of the moisture flux
profiles of the core, CS, and WS are in agreement with Cobb, Michaelis, et al., 2021 with
the core moisture flux maximum exceeding 200 g kg^{-1} m s^{-1} while the CS moisture flux
maximum is around 105 g kg^{-1} m s^{-1} and WS moisture flux maximum is around 130 g kg^{-1}
m s^{-1}. However, the CS and WS profiles in general are slightly lower than reported in Cobb,
Michaelis, et al., 2021 as was seen in the IVT values. As in Cobb, Michaelis, et al., 2021
the core moisture flux maximum is at a higher height than the CS and WS. The structure
of the windspeed profiles is also in agreement with Cobb, Michaelis, et al., 2021 but with
lower values for the CS and WS. In summary, the sector identification algorithm is able to

sufficiently capture the distinct IVT and windspeed characteristics for each AR sector found
in Cobb, Michaelis, et al., 2021 with reduced values for the CS and WS due to the threshold
difference explained above as well as MERRA2 having low windspeed biases in the lower
atmosphere compared to observations (Cobb, Delle Monache, et al., 2021).

4.3.2 Sector Characteristics in 41 years of MERRA2

With confirmation in the ability of the sector identification algorithm to reasonably capture
the distinct IVT and windspeed characteristics of each sector, we expand the analysis above
for 41 years of wintertime (DJF) MERRA2. Fig. 4.4 shows a box plot of the sector IVTs
again but this time including all the ARs (15014 AR samples total compared to 29 AR
samples in Section 4.3.1) found over 1980-2020 in the north Pacific. The core median and
mean IVT are 779 kg m^{-1} s^{-1} and 785 kg m^{-1} s^{-1} respectively. The mean core IVT is 6%
stronger than in Cobb, Michaelis, et al., 2021. The CS (WS) median IVT is 349 kg m^{-1} s^{-1}
(382kg m^{-1} s^{-1}) and the CS (WS) mean IVT is 373 kg m^{-1} s^{-1} (404 kg m^{-1} s^{-1}) which
is or 14% (10%), lower than in Cobb, Michaelis, et al., 2021. Removing the 250 kg m^{-1} s^{-1}
gridpoints brings the CS and WS means to 467 kg m^{-1} s^{-1} (6.6% higher) and 490 kg m^{-1}
s^{-1} (8.4% higher).
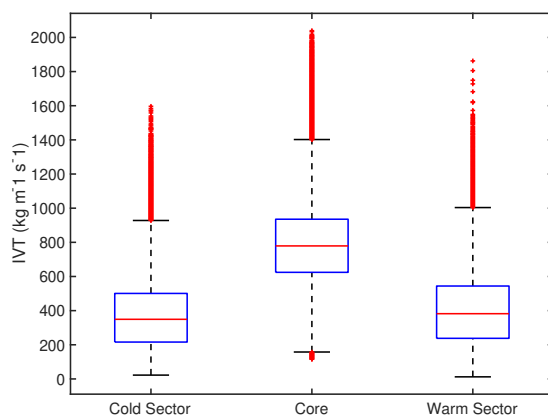
Figure 4.4: Box and whisker plots showing sector IVTs from ARs corresponding to the
observations of Cobb, Michaelis, et al., 2021. The central red mark is the median, the box
edges are the 25th and 75th percentile, and the red pluses are outliers defined as falling
outside of 1.5 * interquartile range.

Examining the vertical profiles in Fig. 4.5, the moisture flux profiles (Fig. 4.5b) structure
is well preserved with a few minor differences from Fig. 4.3b). The core profile has a slightly
reduced maximum moisture flux while the CS has a slightly higher maximum moisture flux.
Near the surface (∼1000 hPa), both the core and CS have increased moisture fluxes. The

windspeed vertical profiles do not exhibit any significant changes at any level. Increasing the analysis to the full reanalysis period shows the sectors are able to maintain characteristic differences for IVT and windspeed.

(a)   Moisture Flux Profile   (b)   Wind Speed Profile

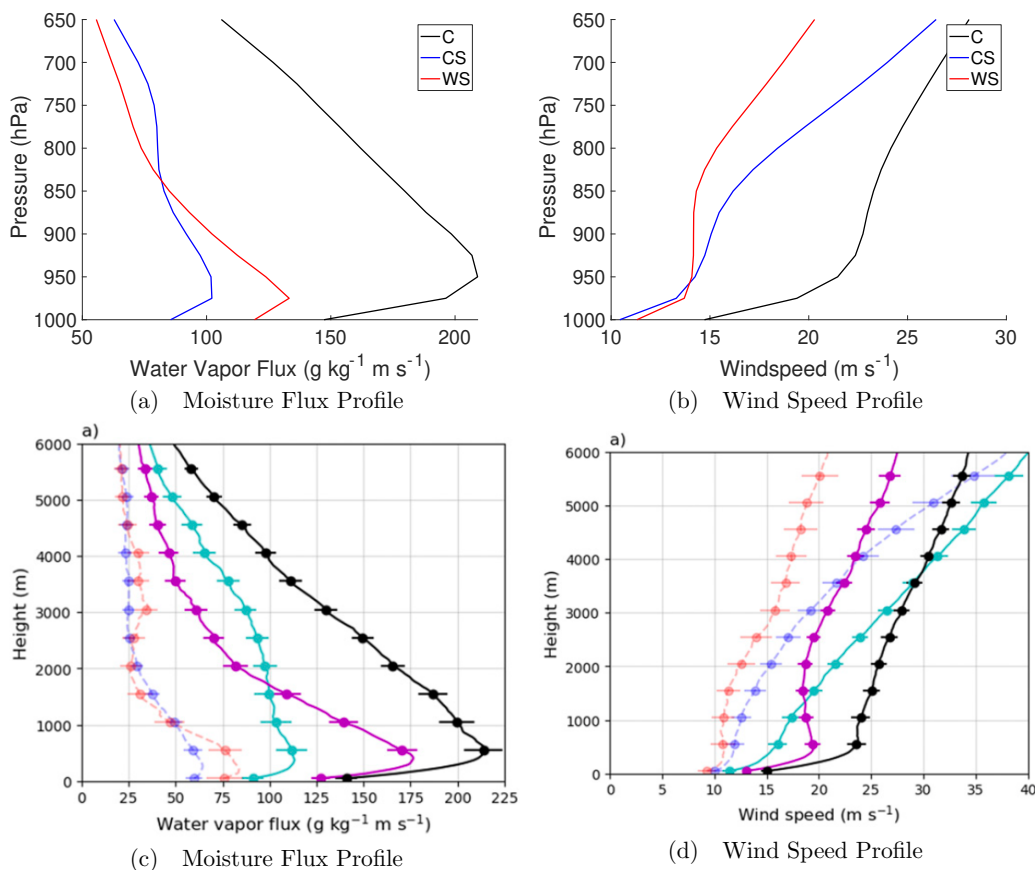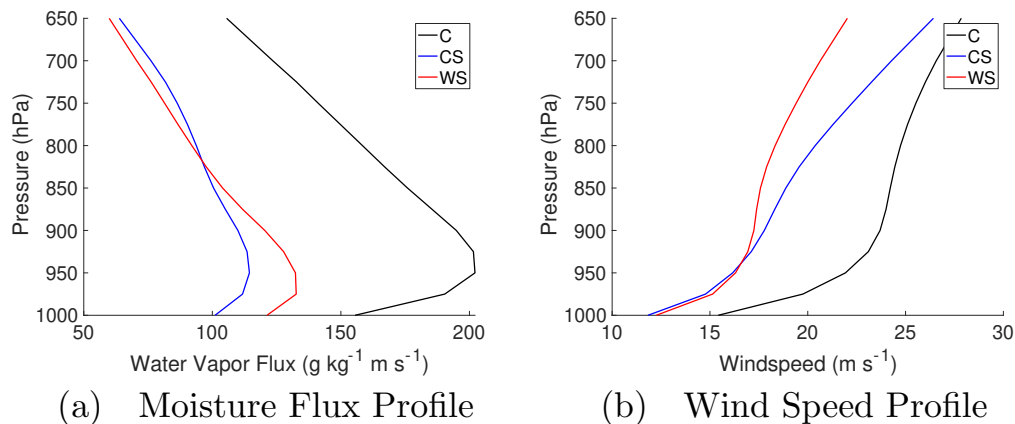Figure 4.5: Vertical profiles of a) moisture flux and b) windspeed from ARs corresponding to the observations of Cobb, Michaelis, et al., 2021.

4.3.3   AR Core Height Impacts on Precipitation

In this section, we demonstrate a use case of the sector identification algorithm by specifically analyzing characteristics of the core - we examine the relationship between AR core height at landfall and the resulting precipitation impacts. We define the AR core height as the height of the maximum moisture flux. Given that MERRA2's vertical resolution is too coarse for our analysis (25 hPa intervals in the lower levels of the atmosphere), we fit a cubic spline to the native MERRA2 moisture flux profile of each AR sample to determine with more accuracy the height of the moisture flux maximum. We take the derivative of our cubic spline, calculate the quadratic roots, determine the maximum, and finally locate the height (in hPa) of the maximum and assign it as the AR core height. Fig. 4.6 shows the distribution of landfalling U.S. west coast AR core heights. In total, 4549 individual ARs meet the location and landfalling criteria and have a mean core height of 931 hPa ($\sim$700 m in altitude) with a standard deviation of 55 hPa. The distribution peaks at 950-940 hPa and most ARs have core heights between 1000 - 850 hPa with a significant left tail. As AR core heights can vary significantly at landfall, we explore how these variations impact precipitation.

Numerous studies (e.g. F. M. Ralph, Dettinger, Rutz, et al., 2020a) have shown the strong relationship between AR IVT and precipitation. As we want to isolate the impact of AR core height on precipitation, we group ARs into weak and moderate categories based on the AR scale (F. M. Ralph et al., 2019). The weak category is for ARs with landfalling IVT
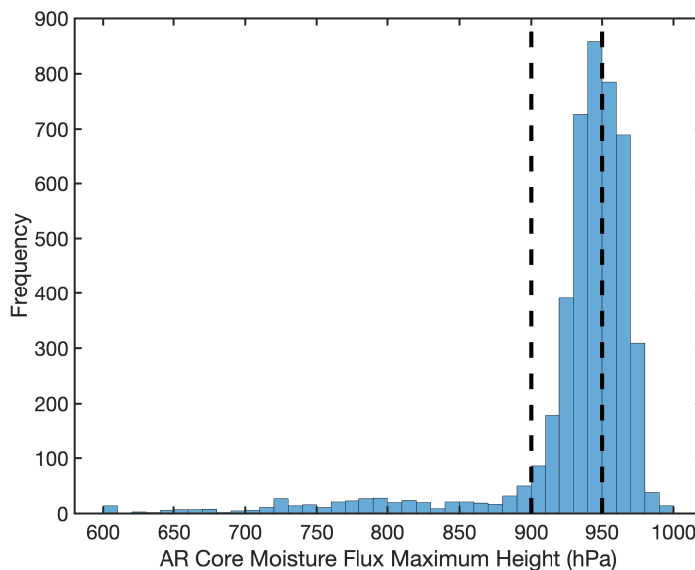
Figure 4.6: Distribution of AR core heights.

values greater than 250 and less than or equal to 500 kgm^-1s^-1 and the moderate category
has values greater than 500 and less than or equal to 750 kgm^-1s^-1. We use only these two
intensity categories which have 2093 and 1782 samples respectively and leave out the strong
category (750 - 1000 kgm^-1s^-1) and above as the number of samples is largely unbalanced.
Landfalling IVT in our study is based on tARget v3's output which records the IVT of an
AR intersecting the coastline using the maximum onshore IVT (Guan and Waliser, 2015).

In addition to the IVT categories, we also group ARs into low, medium, and high core
heights; these groups have AR core heights of 1000 - 950 hPa, 950 - 900 hPa, and less than 900
hPa respectively. Fig. 4.6 has two vertical lines to show the separation between the 3 groups
of AR core heights. We capture the main distribution with low (1836 samples) and medium
(2238 samples) heights and the left tail with the high height (475 samples). Using both the
IVT and AR core height categories, we examine how landfalling AR precipitation is affected
for the western U.S.. Fig. 4.7 shows the precipitation anomalies for each combination of
IVT strength and core height. For the anomalies, we subtract out the mean landfalling AR
precipitation that matches either the weak or moderate strength category. For example, Fig.
4.7a is generated by first calculating the precipitation mean using the moderate strength
ARs with specifically low core heights. This mean is subtracted by the moderate strength
landfalling AR precipitation mean (which includes low, medium, and high core heights)
to isolate the affect of the low core height while controlling for AR strength. Thus, the
anomalies shown, represent how much more or less precipitation falls from landfalling ARs
of a given height compared to all landfalling ARs of similar IVT strength.

For landfalling, low core height ARs (Fig. 4.7a and b), the coastal regions of the western

(a)   Moderate IVT, low height

(b)   Weak IVT, low height

(c)   Moderate IVT, medium height

(d)   Weak IVT, medium height

(e)   Moderate IVT, high height

(f)   Weak IVT, high height

Figure 4.7: Landfalling AR precipitation anomalies in mm/day. The rows are organized by
core heights (low, medium, and high from top to bottom) and the columns are organized by
landfalling IVT strength (moderate and weak from left to right).

U.S. receives positive precipitation anomalies (>3mm/day for some regions) for both weak
and moderate ARs. The positive anomalies are stronger for the moderate strength ARs
(Fig. 4.7a) compared to the weak strength ARs (Fig. 4.7b) but the distribution of positive
anomalies is consistent. The area of the strongest anomalies is just north of the California
bay area where the coastal ranges have a gap. This low topography area is an exception to
the rest of the west coast which has coastal mountain ranges.

Medium core height ARs (Fig. 4.7c and d) deliver relatively less precipitation compared
to other core heights. This is consistent between moderate and weak ARs with both showing
similar distributions of anomalies. The largest precipitation deficits are over areas of high
topography over the Sierra Nevada ranges and over northern California/Oregon. The deficits
persist into the interior of the U.S.

For high core heights (Fig. 4.7e and f), the precipitation anomalies are mostly positive
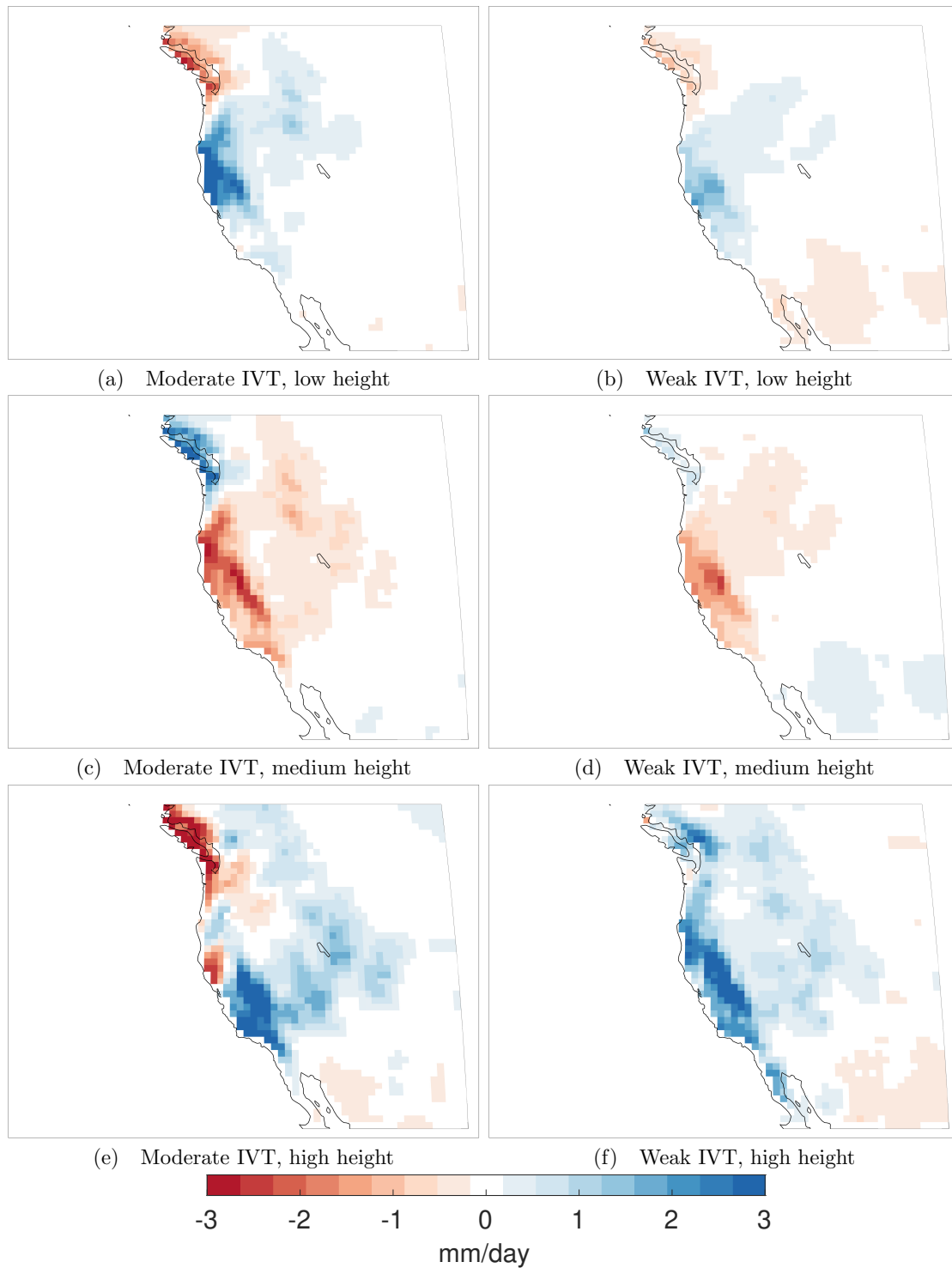with some differences between the moderate and weak strength ARs. While the weak, high
core ARs show positive anomalies throughout the western U.S., the moderate strength ARs
deliver less precipitation to low lying coastal areas. Consistent for both are the strong
positive anomalies (>3 mm/day) over the highest regions of the Sierra Nevada as well as the
interior of the western U.S..

In summary, for the western U.S. i) the low core height ARs tend to bring more precipi-
tation but especially so in the lower topography areas, ii) the medium core height ARs bring
less precipitation with the largest deficits over high topography, and iii) the high core height
ARs generally bring more precipitation to the west with a preference for high topography
areas and the interior of the western U.S.. Low core height ARs enable the most forced
ascent of moisture from orography, given their moisture flux maxima at near surface levels,
which is advantageous for generating precipitation. Many ARs with high core heights are
at the same altitude as most of the coastal mountain tops where the relationship between
moisture flux and orographic precipitation is maximized (Neiman et al., 2002) and some very
high core ARs are even at the altitude of the Sierra Nevadas. Medium core height ARs seem
to lack any orographic precipitation advantages, neither maximizing forced moisture ascent
nor are they at the optimal level of mountain tops.

4.3.4   AR Core Height and Terrain Interactions

As topography has mixed effects for AR precipitation from different core heights, we explore
if statistical relationships between AR precipitation and core heights differ for various terrain
heights. As our focus is on the western U.S., we split the terrain heights over California,
Oregon, and Washington into three categories: low = 10-500m, medium = 500-1250m, and
high = >1250m. For reference, the coastal ranges are typically 500-1500m and the Sierra
Nevada range peaks at heights above 4km. Fig. 4.8 shows the distribution of the three
height categories for our domain.

We first examine the distributions of precipitation over each of the terrain heights. Fig.
4.9 shows these distributions separated by AR core heights and also displays the mean line
for each core height. For all three terrain heights, the medium height ARs deliver the

(a) Topography   (b) Terrain Categories
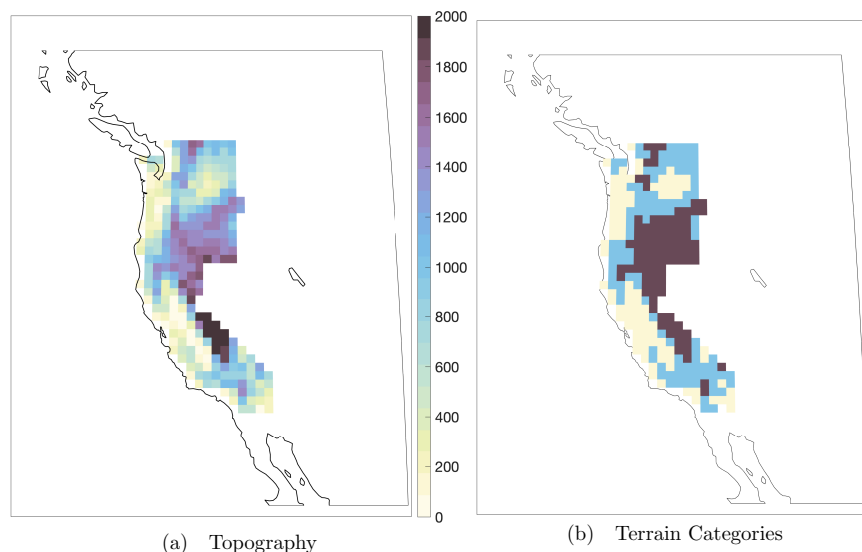
Figure 4.8: (a) Topography over California, Oregon, and Washington in meters. (b) Topography is split into three categories based on height with yellow, blue, and purple for low, medium, and high topography respectively.

least amount of precipitation while the low and high ARs deliver nearly the same amount. Using an ANOVA (analysis of variance), we confirm that the medium core AR height mean is significantly different (significance level at 0.01) than the low and high core AR height means across all terrain heights. The low and high core height means are not significantly for any terrain height.

(a) low   (b) medium   (c) high
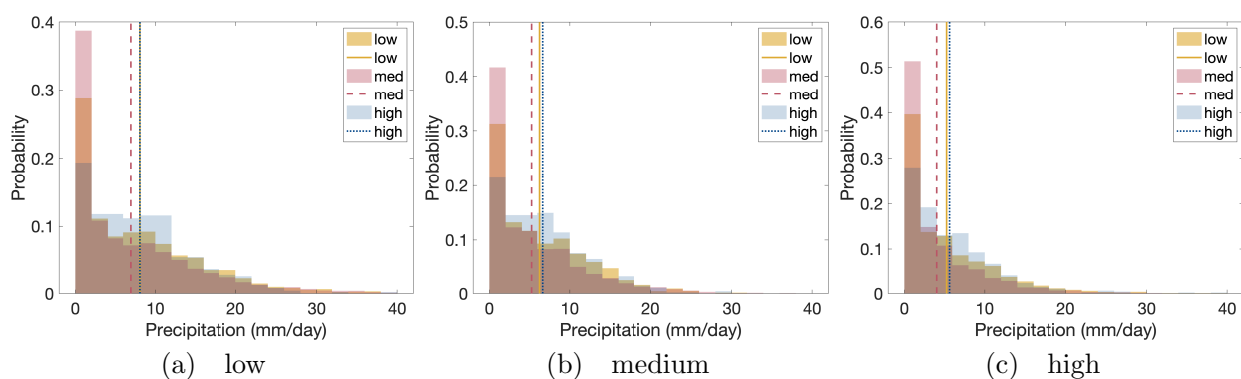
Figure 4.9: Distributions of precipitation for low (a), medium (b), and high (c) terrain. Each plot has three distributions from low (yellow), medium (red), and high (blue) AR core heights along with a vertical mean line.

Given that IVT has been shown to have a strong relationship with precipitation (Neiman

et al., 2002), we first take a linear regression of AR landfalling IVT with precipitation over
each of the terrain heights. For each landfalling AR in the U.S., we record the average precip-
itation over the entire low, medium, and high terrain categories separately. Fig. 4.10 shows
this relationship for precipitation over low, medium, and high topography. As expected,
higher landfalling IVTs tend to produce higher precipitation over all terrain heights but the
strongest relationship (highest R-squared) is over medium height terrain - corresponding
to the height of the coastal mountains where Neiman et al., 2002 also found the strongest
relationship.

(a)   low   (b)   medium   (c)   high
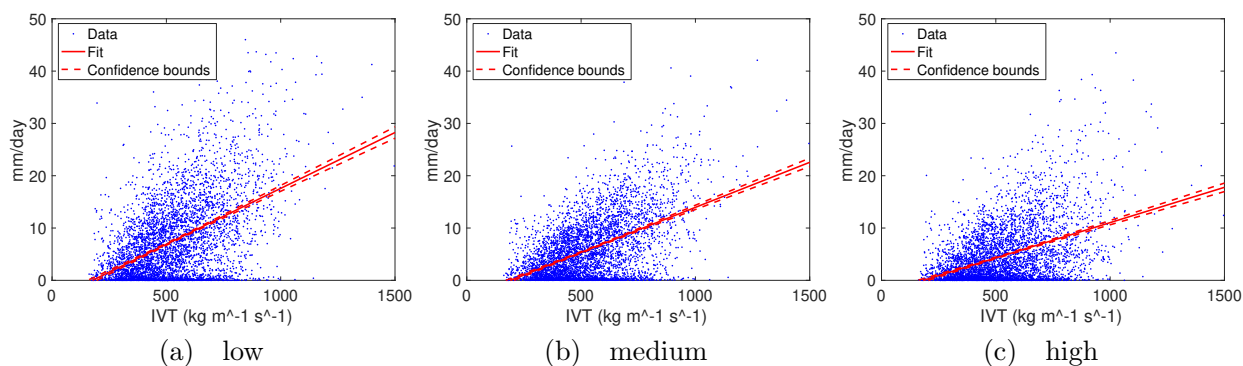
Figure 4.10: Linear regressions fit to landfalling IVT and precipitation over various terrain
heights.

(a)   low   (b)   medium   (c)   high
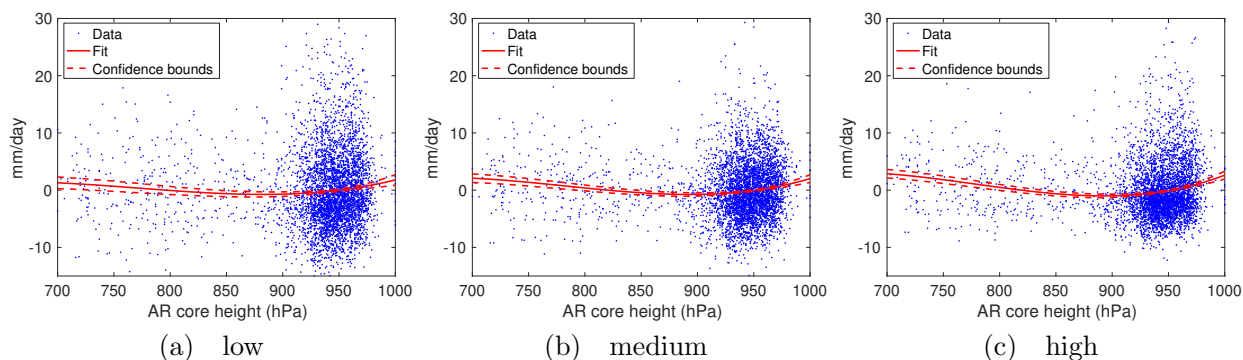
Figure 4.11: Cubic polynomial fit to the residuals from Fig. 4.10 and AR core heights over
terrain heights.

We take the residuals from Fig. 4.10 and look at relationship with AR core heights to
isolate how AR core heights impact precipitation without the impact of IVT. Fig. 4.11 shows
this relationship with a cubic polynomial fit. Across all terrain heights, precipitation effects
from AR core heights show a consistent relationship - near surface (> 950 hPa) and high AR

core heights (< 900 hPa) are able to produce more precipitation more effectively compared to medium height ARs (950-900). This relationship is strongest over high topography and weakest over low topography. Table 4.1 examines how precipitation over low, medium, and high terrain is expected to change given AR core heights of 1000, 900, and 800 hPa. These values corroborate the precipitation anomaly patterns seen in Fig. 4.7. For low AR core heights (1000 hPa), precipitation is enhanced across all terrain heights increasing from +1.78 mm/day to +2.63 mm/day from low to high terrain. Medium AR core heights (900 hPa) see reduced precipitation across all terrain heights going from -0.70 mm/day to -0.98 mm/day from low to high terrain. Lastly, for high AR core heights (800 hPa), there is a slight reduction of precipitation over low terrain at -0.05 mm/day but we see enhanced precipitation over medium and high terrain up to 0.48 mm/day. To note, these values capture precipitation across a wide domain (3 coastal states) but do not account for precipitation in the interior of the U.S. which high ARs (800 hPa) seem to enhance significantly.

	Low (10-500m)	Medium (500-1250m)	High (>1250m)
1000hPa	1.78	2	2.63
900hPa	-0.70	-0.74	-0.98
800hPa	-0.05	0.38	0.48

Table 4.1: Expected precipitation changes (mm/day) over low, medium, and high terrain due to differences in AR core height.

4.3.5 AR Core Height Trends

As different AR core heights can enhance or reduce the amount of precipitation for the western U.S., we examine what sort of trends there are for AR core heights through our study period. We look at the probability distribution of AR core heights in the first decade (1980-1989) of reanalysis and the last decade (2011-2020). Fig. 4.12 shows how the distribution has changed to favor low and high AR core heights. AR core heights from 970-920 hPa have reduced probability while AR core height probabilities outside that range either increase or stay nearly the same. The mean AR core height changes from 931.2 hPa to 927.6 hPa and the standard deviation changes from 43.7 hPa to 50.6 hPa. In general, AR core heights are trending to have larger variability around a slightly lower core mean.

4.4 Conclusion

In this preliminary study, we have sought to explore the relationship between AR core heights and precipitation over the western U.S.. To do so, we first developed a novel AR sector identification algorithm so that we could work specifically with the core of the AR. The algorithm works on the output of Guan and Waliser, 2019's tARget v3 and segments
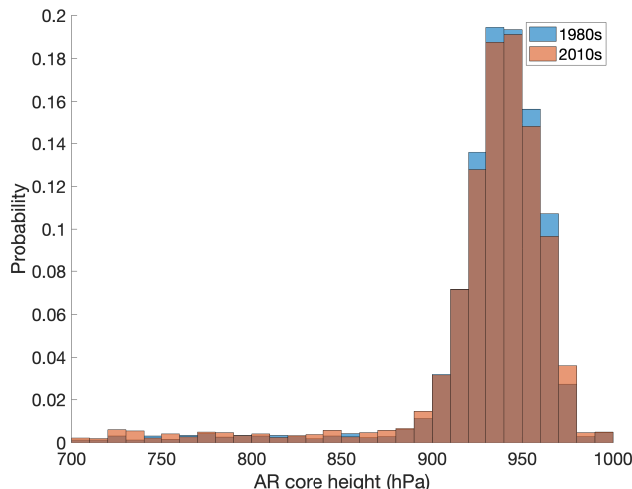
Figure 4.12: AR core height distributions for the first and last decade of reanalysis.

the core but also the CS, and WS of individual ARs. The characteristics of these identified sectors are able to generally capture the same distinct IVT and windspeed characteristics found using dropsonde observations in Cobb, Michaelis, et al., 2021. We first compared our sectors to Cobb, Michaelis, et al., 2021 using the same AR events as the observations - a total of 29 ARs from the IOPs - by time matching reanalysis data with the observations. We next used the full 41 years of wintertime (DJF) reanalysis period. The core is very well represented with both water vapor fluxes and wind speeds in agreement with Cobb, Michaelis, et al., 2021. In general, due to a difference in IVT thresholds for defining an AR (>250 kg m^{-1} s^{-1} versus relative threshold that allows values <250 kg m^{-1} s^{-1}), the CS and WS have smaller IVT means as well as reduced moisture fluxes at lower levels. When excluding the gridpoints <250 kg m^{-1} s^{-1}, the means for the CS and WS are improved significantly. Another factor for the lower moisture flux values can come from the lower wind speeds recorded using our algorithm. However, as noted in Section 4.1,Cobb, Delle Monache, et al., 2021's study found that MERRA2 tends to have weaker windspeeds at lower levels when comparing to dropsonde observations so this bias may also push the CS and WS fluxes and windspeeds down.

After demonstrating that the sector algorithm is able to accurately segment the core, we investigate what affect AR core heights have on landfalling AR precipitation for the western U.S.. We provide a control on IVT by separately grouping weak and moderate ARs then calculating precipitation anomalies for ARs with low, medium, and high core heights. ARs with different core heights interact with topography very differently producing distinct patterns of precipitation anomalies. The precipitation anomalies reveals that i) low core height ARs enhance precipitation over varied topography but particularly so over low topography, ii) medium core height ARs reduce precipitation throughout the U.S. west but particularly over elevated terrain, and iii) high core height ARs enhance precipitation over

high terrain and in the interior of the U.S.. While low core heights maximize the amount of orographic moisture ascent, high core heights are situated at an optimal height for the coastal and Sierra Nevada ranges.

To further explore this relationship we examined how different terrain heights interact with ARs. We categorized the coastal western U.S. (California, Oregon, Washington) topography into low, medium, and high terrain. Distributions of precipitation from the various core heights over each terrain height category further confirms that medium core height ARs produce less precipitation than low and high core heights across all terrain categories. After removing the effect of landfalling IVT from AR precipitation, we examined what statistical relationship AR core height has with AR precipitation at landfall. Fitting a cubic polynomial through the residuals and AR core heights reveals the same patterns seen in the precipitation anomalies. Low ARs enhance precipitation (+1.78 mm/day to +2.63 mm/day) at all terrain heights. To note, low core height ARs are the only ARs with enhanced precipitation at low altitudes. Medium core height ARs reduce precipitation across the U.S. west (-0.98 mm/day to -0.70 mm/day) and high core height ARs enhance precipitation in elevated terrain(+0.38 mm/day to 0.46 mm/day). AR core heights in general have a stronger affect on precipitation rates over elevated terrain. These findings are supported by the work of Neiman et al., 2002 and Backes et al., 2015 which found that the relationship between upslope moisture flow and rainrate is maximized at the top of elevated terrain. Their correlations are strongest at the mountain top and are reduced moving down in altitude which supports our finding that high ARs ($\sim$1000 m and up) enhance precipitation more effectively than the medium height ARs ($\sim$500 m to 1000m). Backes et al., 2015 also showed the importance of mid level jets associated with ARs (which would register as a high core AR) in delivering precipitation to the Sierra Nevadas. These higher ARs are also able to deliver more moisture to the interior of the western U.S.. Neiman, Ralph, et al., 2013 showed that moisture flux maximized at $\sim$2 km in altitude - which we consider a high core height AR - for an AR that brought flooding to Arizona.

Our study also finds that AR core heights have become more variable over time. When comparing the probability distribution of AR core heights from 1980-1989 and 2011-2020, AR core height means are slightly higher in altitude (931.2 hPa to 927.6 hPa) and have a significantly larger standard deviation (43.7 hPa to 50.6 hPa). In short, the trend for landfalling ARs is more low and high AR core heights and less medium AR core heights.

In the context of a warming climate, ARs are robustly projected to have more intense IVTs due to increased moisture but the dynamics and interactions with topography are still an area requiring further study (Payne et al., 2020). Over orography Siler and Roe, 2014 found that due to basic thermodynamics in a warming climate, the vertical structure of condensation shifts upward and results in precipitation shifts to the leeward side of mountains. Additionally, under warming, ARs are projected to have an increase vapor transport above the tops of mountains due to both increased moisture and an expanding Hadley cell (Payne et al., 2020). This increase in above crest vapor transport results in an increase in inland penetrating ARs. The trends we see for higher AR core heights may in part be explained by warming over the past 4 decades. Higher AR core height ARs delivering more precipita-

tion into the interior of the U.S. coupled with the fact that warming enhances leeward side precipitation, highlights how ARs and orography interactions are important in determining hydrological projections for the entire western U.S..

4.5 Acknowledgements

Chapter 5

Conclusion

5.1 Summary

Atmospheric rivers are increasingly recognized as critical players in global and regional hydrology with their impacts felt from pole to pole. As interest in ARs has grown over the past few decades, new methods, technology, and observations and have advanced AR science so that we now know ARs contribute a significant fraction of annual precipitation on the western side of continents and especially in the presence of elevated terrain. However, forecasts are still limited for ARs - determining where, when, and particularly how much precipitation will fall for landfalling ARs is still an open issue. This dissertation contributes to addressing this challenge by furthering our understanding of AR genesis, representation, and structure.

Chapter 2 examines the synoptic patterns that lead to AR genesis. These patterns vary in how often they occur and initiate ARs. A catalogue of 500 hPa geopotential height anomalies on days ARs form over the north Pacific is used in a SOM analysis and reveals that there are two distinct pairs of atmospheric patterns and associated climate modes that control AR lifetime characteristics. One pair of patterns matches up with the positive and negative modes of ENSO, PDO, PNA, and the NP pattern. The second pair of patterns matches up with the positive and negative modes of the AO, EPO, and WPO. We broadly call these groups the 'ENSO modes' and the 'jet modes' respectively. The ENSO modes, depending on whether they are positive or negative, control the longitude of genesis, the duration, the travel distance, speed, zonal displacement, and location of precipitation of ARs. The jet modes on the otherhand affect different characteristics: genesis latitude, track latitude, meridional displacement, IVT strength, and precipitation amount. Examining the large-scale circulation associated with all the patterns reveal that the position and the strength of the upper-level jet has a close relationship with AR genesis particularly in the western and central Pacific. The eastern Pacific AR characteristics are affected by southwesterly wind anomalies which may be related to Rossby wave breaking.

Chapter 3 evaluates E3SM - a new, state-of-the-science global climate model developed by the U.S. DOE with a particular emphasis on the water cycle processes. The goal is to reduce

uncertainties for researchers using this next generation model for their research. E3SM is specifically evaluated for its ability to accurately represent ARs globally by comparing to a widely-used reanalysis dataset. The global AR characteristics and AR precipitation show very high degrees of correlation and very low mean absolute errors annually, seasonally, and across different ensemble members. Biases, however, are found with the most significant biases related to the double-ITCZ issue. The double-ITCZ leads to the subtropical jet to be stronger and shifted more equatorward. These biases are attributed to model coupling or the atmospheric component of the model.

Chapter 4 explores the question of how the vertical structure of ARs can influence precipitation when they reach land. Using a novel AR sector algorithm, we focus specifically on the AR core and look at the relationship between the height of the AR core's maximum moisture flux and landfalling precipitation over a variety of terrain heights. Whilst controlling for IVT intensity (weak and moderate) we examined precipitation anomalies and find ARs with low core heights enhance precipitation (compared to all ARs of similar intensity) over the western U.S. regardless of terrain height, ARs with medium core heights depress precipitation but particularly so over elevated terrain, and high core ARs enhance precipitation over elevated terrain and into the interior of the U.S.. These precipitation patterns in low, medium, and high AR core heights are confirmed by examining precipitation probability distributions for each AR core height category across each terrain heights. Trends for AR core heights from the past four decades shows AR core heights are trending to be slightly higher in altitude with a growing proportion of ARs in the low and high category.

Overall, this dissertation has sought to advance AR understanding in key areas identified by the AR community. We advance our understanding of AR genesis and the associated synoptic conditions, the relationship between upper-level and low-level jets and ARs, and how the height of the AR core influences landfalling precipitation. We enable confidence in the community's use of a state-of-the-science climate model with a comprehensive evaluation of AR representation and have developed a novel sector identification algorithm. The hope is that this dissertation both moves AR science forward and also opens opportunities for new directions of research.

5.2 Future work

5.2.1 Extending AR forecasts

With the synoptic patterns associated with AR genesis established in Chapter 2, we ask what are the applications beyond basic understanding of genesis conditions? These results lay the groundwork for potential future directions and studies. For example, one potential study can utilize statistical downscaling to investigate whether these synoptic patterns can be used to determine the distribution and magnitude of wintertime precipitation. Given a winter season with different frequencies of each node's synoptic pattern, can we estimate how much and where AR precipitation will fall? Additionally, there are several possible directions

in the area of subseasonal-to-seasonal (S2S) forecasting - an area currently facing challenges but is critical for water management. As predictions of large-scale climate modes, such as ENSO, become more accurate and at much longer lead times, the phases of these modes can be exploited to gain understanding of the types of synoptic patterns that can result and thereby help estimate the wintertime precipitation. Previous studies have already found success with ARs using certain phases of MJO and QBO (Baggett et al., 2017). Another S2S related direction is to investigate the preconditions associated with each node. Benedict et al., 2019 examined precursors to landfalling ARs and found robust patterns with important connections to ARs over a week prior to landfall. The synoptic conditions identified in their study show promising similarities to nodes identified here. Lastly, future climates can be examined. In a warming climate, how do the frequencies of these synoptic conditions and the various climate modes change?

5.2.2 Improving AR representation

In Chapter 3, we provide a comprehensive, global overview of AR representation in the fully-coupled historical E3SM v1.0 simulation that should give users of E3SM confidence in its ability to realistically simulate ARs while still being aware of the model's biases. The most significant source of biases comes from the double-ITCZ issue. Evaluating AR frequency biases in other CMIP5/6 GCMs to reanalysis, such as those used in T. A. O'Brien et al., 2021, suggests that the AR biases associated with a double-ITCZ may be more general than found in E3SM alone. Reducing the double-ITCZ bias remains an open issue in modeling, but previous studies suggests that improvements to parameterizations of boundary-layer turbulence and convective schemes can reduce this bias (e.g. Song and Zhang, 2018; Lu et al., 2021) which in turn could improve the water vapor transport and AR biases seen in E3SM as well as other GCMs. Although we have framed this analysis through the lens of ARs, the biases in large-scale conditions are relevant to other phenomena and could also provide potential areas of improvement in the EAM and the fully-coupled simulations.

Additionally, analysis of a growing number of new high-resolution (e.g. 0.25° x 0.25°) simulations suggests that higher resolution models are better able to represent local geography and topography, AR characteristics, and AR precipitation globally including for the most extreme ARs (X. Liu et al., 2022; Wang et al., 2023; Shields et al., 2023); Guan and Waliser, 2017). Thus, the double-ITCZ bias (especially in context of future projections) and resolution impacts (both vertical and horizontal) are two significant areas deserving of more research and would improve understanding of current and projected AR impacts.

Lastly, Deep Learning (DL) methods are emerging for a wide range of applications for climate and weather. For ARs, there are new DL tracking methods being developed from the ClimateNet project that remove the need for engineered heuristics and instead relies on expert labels for pattern recognition training (Kashinath et al., 2021). For example, Fig. 5.1 shows ARs detected by training a DL model on the expert labels. DL methods have also shown improved performance compared to traditional heuristics which is becoming increasingly important with high-resolution models and large ensembles becoming more prevalent.
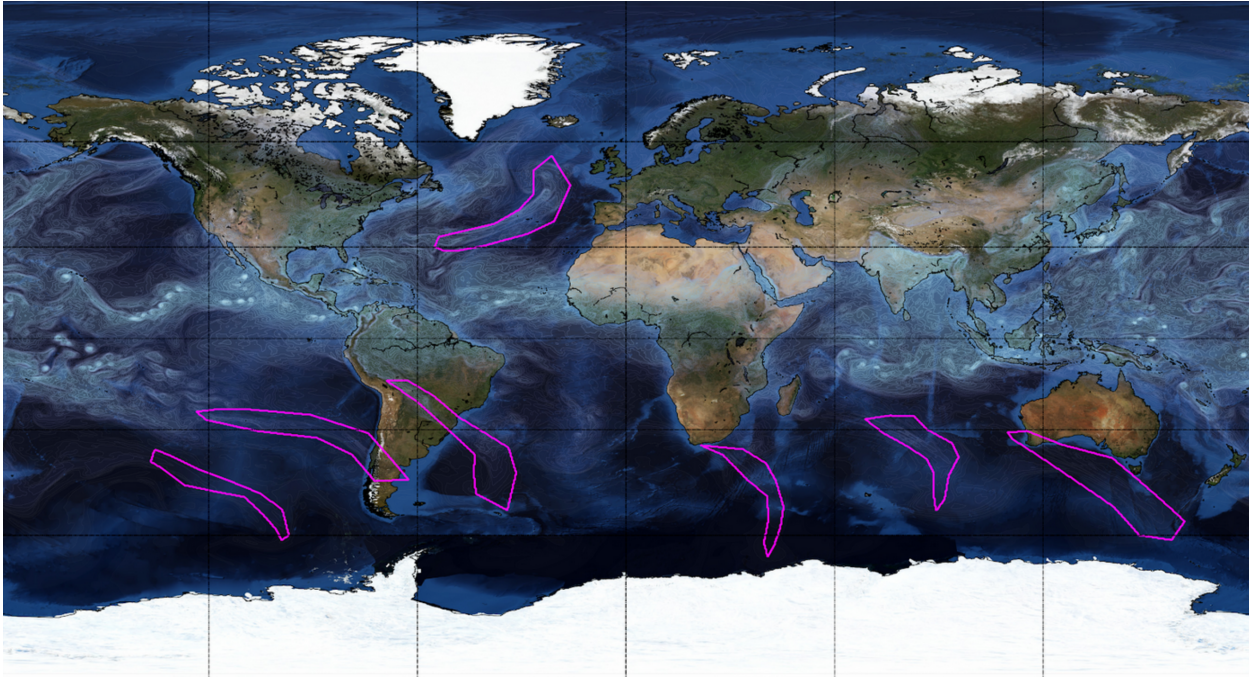
Figure 5.1: Labels of ARs (magenta) and tropical cyclones (yellow) predicted by the ClimateNet deep learning model (Kashinath et al., 2021).

More work on evaluating DL ARs is required especially within ARTMIP and across different models and resolutions.

5.2.3 Mechanisms affecting AR core heights

While we provided a preliminary study on AR cores heights interacting with complex terrain in Chapter 4, we hope to further analyze this relationship in future studies. Our analysis can be strengthened by taking into account differences in landfall latitude for ARs. While we isolate landfalling ARs in the U.S., our current analysis does not differentiate between an AR that hits southern California and one that hits the northern tip of Washington. The precipitation averaging over the entire low, medium, and high terrain heights is a related issue as an AR might interact mostly with one terrain type given its trajectory. These issues can largely be resolved by refining the analysis to the gridpoint level which we intend to do. Additionally, we have not comprehensively looked into the mechanisms that may cause varying AR heights to precipitate differently, especially the medium height ARs. We hypothesize that barrier jets, which are common along western U.S. topography, may influence AR core height and precipitation as has been seen in prior studies (Neiman et al., 2002; Smith et al., 2010; Neiman, Hughes, et al., 2013). We also would like to expand our study to comprehensively examine the CS and WS sectors of ARs. Dolan et al., 2022 for example

found the warm sector of ARs to contribute significantly to orographic precipitation in 4 observational case studies. Lastly, related to Section 5.2.2, we must consider the resolution - both horizontal and vertical - of our dataset. The current MERRA2 resolution may be to too rough to resolve topography over the complex terrain of the western U.S. and fail to capture finer details of AR features and precipitation.

Bibliography

Akinduko, A. A., Mirkes, E. M., & Gorban, A. N. (2016). Som: Stochastic initialization versus principal components. *Information Sciences*, *364*, 213–221.

AMS. (2023). Atmospheric river - glossary of meteorology. https://glossary.ametsoc.org/wiki/Atmospheric_river

Bação, F., Lobo, V., & Painho, M. (2005). Self-organizing maps as substitutes for k-means clustering. *International Conference on Computational Science*, 476–483.

Backes, T. M., Kaplan, M. L., Schumer, R., & Mejia, J. F. (2015). A climatology of the vertical structure of water vapor transport to the sierra nevada in cool season atmospheric river precipitation events. *Journal of Hydrometeorology*, *16*(3), 1029–1047.

Baggett, C. F., Barnes, E. A., Maloney, E. D., & Mundhenk, B. D. (2017). Advancing atmospheric river forecasts into subseasonal-to-seasonal time scales. *Geophysical Research Letters*, *44*(14), 7528–7536.

Benedict, J. J., Clement, A. C., & Medeiros, B. (2019). Atmospheric blocking and other large-scale precursor patterns of landfalling atmospheric rivers in the north pacific: A cesm2 study. *Journal of Geophysical Research: Atmospheres*, *124*(21), 11330–11353.

Caesar, L., Rahmstorf, S., Robinson, A., Feulner, G., & Saba, V. (2018). Observed fingerprint of a weakening atlantic ocean overturning circulation. *Nature*, *556*(7700), 191–196.

Caldwell, P. M., Mametjanov, A., Tang, Q., Van Roekel, L. P., Golaz, J.-C., Lin, W., Bader, D. C., Keen, N. D., Feng, Y., Jacob, R., et al. (2019). The doe e3sm coupled model version 1: Description and results at high resolution. *Journal of Advances in Modeling Earth Systems*, *11*(12), 4095–4146.

Chen, X., Leung, L. R., Wigmosta, M., & Richmond, M. (2019). Impact of atmospheric rivers on surface hydrological processes in western us watersheds. *Journal of Geophysical Research: Atmospheres*, *124*(16), 8896–8916.

Chiang, J. C., Fischer, J., Kong, W., & Herman, M. J. (2019). Intensification of the pre-meiyu rainband in the late 21st century. *Geophysical Research Letters*, *46*(13), 7536–7545.

Cobb, A., Michaelis, A., Iacobellis, S., Ralph, F., & Delle Monache, L. (2021). Atmospheric river sectors: Definition and characteristics observed using dropsondes from 2014–20 calwater and ar recon. *Monthly Weather Review*, *149*(3), 623–644.

Cobb, A., Delle Monache, L., Cannon, F., & Ralph, F. M. (2021). Representation of dropsonde-observed atmospheric river conditions in reanalyses. *Geophysical Research Letters*, *48*(15), e2021GL093357.

Corringham, T. W., Ralph, F. M., Gershunov, A., Cayan, D. R., & Talbot, C. A. (2019). Atmospheric rivers drive flood damages in the western united states. *Science advances*, *5*(12), eaax4631.

DeFlorio, M. J., Waliser, D. E., Guan, B., Ralph, F. M., & Vitart, F. (2019). Global evaluation of atmospheric river subseasonal prediction skill. *Climate Dynamics*, *52*(5), 3039–3060.

Dettinger, M. D., Ralph, F. M., Das, T., Neiman, P. J., & Cayan, D. R. (2011). Atmospheric rivers, floods and the water resources of california. *Water*, *3*(2), 445–478.

Dolan, B., Rutledge, S. A., & Rasmussen, K. L. (2022). Multiscale interactions contributing to enhanced orographic precipitation in landfalling frontal systems over the olympic peninsula. *Monthly Weather Review*, *150*(6), 1207–1231.

Dong, L., Leung, L. R., Lu, J., & Song, F. (2021). Double-itcz as an emergent constraint for future precipitation over mediterranean climate regions in the north hemisphere. *Geophysical Research Letters*, *48*(3), e2020GL091569.

Espinoza, V., Waliser, D. E., Guan, B., Lavers, D. A., & Ralph, F. M. (2018). Global analysis of climate change projection effects on atmospheric rivers. *Geophysical Research Letters*, *45*(9), 4299–4308.

Eyring, V., Bony, S., Meehl, G. A., Senior, C. A., Stevens, B., Stouffer, R. J., & Taylor, K. E. (2016). Overview of the coupled model intercomparison project phase 6 (cmip6) experimental design and organization. *Geoscientific Model Development*, *9*(5), 1937–1958.

Florsheim, J. L., & Dettinger, M. D. (2015). Promoting atmospheric-river and snowmelt-fueled biogeomorphic processes by restoring river-floodplain connectivity in california's central valley. In *Geomorphic approaches to integrated floodplain management of lowland fluvial systems in north america and europe* (pp. 119–141). Springer.

Friedman, A. R., Hwang, Y.-T., Chiang, J. C., & Frierson, D. M. (2013). Interhemispheric temperature asymmetry over the twentieth century and in future projections. *Journal of Climate*, *26*(15), 5419–5433.

Gelaro, R., McCarty, W., Suárez, M. J., Todling, R., Molod, A., Takacs, L., Randles, C. A., Darmenov, A., Bosilovich, M. G., Reichle, R., et al. (2017). The modern-era retrospective analysis for research and applications, version 2 (merra-2). *Journal of Climate*, *30*(14), 5419–5454.

Gibson, P. B., Perkins-Kirkpatrick, S. E., Uotila, P., Pepler, A. S., & Alexander, L. V. (2017). On the use of self-organizing maps for studying climate extremes. *Journal of Geophysical Research: Atmospheres*, *122*(7), 3891–3903.

Gimeno, L., Nieto, R., Vázquez, M., & Lavers, D. A. (2014). Atmospheric rivers: A mini-review. *Frontiers in Earth Science*, *2*, 2.

Golaz, J.-C., Caldwell, P. M., Van Roekel, L. P., Petersen, M. R., Tang, Q., Wolfe, J. D., Abeshu, G., Anantharaj, V., Asay-Davis, X. S., Bader, D. C., et al. (2019). The

doe e3sm coupled model version 1: Overview and evaluation at standard resolution. *Journal of Advances in Modeling Earth Systems*, *11*(7), 2089–2129.

Gonzales, K. R., Swain, D. L., Nardi, K. M., Barnes, E. A., & Diffenbaugh, N. S. (2019). Recent warming of landfalling atmospheric rivers along the west coast of the united states. *Journal of Geophysical Research: Atmospheres*, *124*(13), 6810–6826.

Guan, B., & Waliser, D. E. (2015). Detection of atmospheric rivers: Evaluation and application of an algorithm for global studies. *Journal of Geophysical Research: Atmospheres*, *120*(24), 12514–12535.

Guan, B., & Waliser, D. E. (2017). Atmospheric rivers in 20 year weather and climate simulations: A multimodel, global evaluation. *Journal of Geophysical Research: Atmospheres*, *122*(11), 5556–5581.

Guan, B., & Waliser, D. E. (2019). Tracking atmospheric rivers globally: Spatial distributions and temporal evolution of life cycle characteristics. *Journal of Geophysical Research: Atmospheres*.

Guan, B., Waliser, D. E., & Ralph, F. M. (2018). An intercomparison between reanalysis and dropsonde observations of the total water vapor transport in individual atmospheric rivers. *Journal of Hydrometeorology*, *19*(2), 321–337.

Guirguis, K., Gershunov, A., Shulgina, T., Clemesha, R. E., & Ralph, F. M. (2019). Atmospheric rivers impacting northern california and their modulation by a variable climate. *Climate dynamics*, *52*(11), 6569–6583.

Hagos, S. M., Leung, L. R., Yoon, J.-H., Lu, J., & Gao, Y. (2016). A projection of changes in landfalling atmospheric river frequency and extreme precipitation over western north america from the large ensemble cesm simulations. *Geophysical Research Letters*, *43*(3), 1357–1363.

Hansen, J. E., Sato, M., Lacis, A., Ruedy, R., Tegen, I., & Matthews, E. (1998). Climate forcings in the industrial era. *Proceedings of the National Academy of Sciences*, *95*(22), 12753–12758.

Hecht, C. W., & Cordeira, J. M. (2017). Characterizing the influence of atmospheric river orientation and intensity on precipitation distributions over north coastal california. *Geophysical Research Letters*, *44*(17), 9048–9058.

Hewitson, B., & Crane, R. G. (2002). Self-organizing maps: Applications to synoptic climatology. *Climate Research*, *22*(1), 13–26.

Hu, A., Van Roekel, L., Weijer, W., Garuba, O. A., Cheng, W., & Nadiga, B. T. (2020). Role of amoc in transient climate response to greenhouse gas forcing in two coupled models. *Journal of Climate*, *33*(14), 5845–5859.

Hu, H., Dominguez, F., Wang, Z., Lavers, D. A., Zhang, G., & Ralph, F. M. (2017). Linking atmospheric river hydrological impacts on the us west coast to rossby wave breaking. *Journal of Climate*, *30*(9), 3381–3399.

Huang, X., & Swain, D. L. (2022). Climate change is increasing the risk of a california megaflood. *Science advances*, *8*(31), eabq0995.

Hughes, M., Mahoney, K. M., Neiman, P. J., Moore, B. J., Alexander, M., & Ralph, F. M. (2014). The landfall and inland penetration of a flood-producing atmospheric river in

arizona. part ii: Sensitivity of modeled precipitation to terrain height and atmospheric river orientation. *Journal of Hydrometeorology*, *15*(5), 1954–1974.

Jiang, N., Luo, K., Beggs, P. J., Cheung, K., & Scorgie, Y. (2015). Insights into the implementation of synoptic weather-type classification using self-organizing maps: An australian case study. *International Journal of Climatology*, *35*(12), 3471–3485.

JISAO. (2020). Pacific decadal oscillation (pdo) index.

Kashinath, K., Mudigonda, M., Kim, S., Kapp-Schwoerer, L., Graubner, A., Karaismailoglu, E., Von Kleist, L., Kurth, T., Greiner, A., Mahesh, A., et al. (2021). Climatenet: An expert-labeled open dataset and deep learning architecture for enabling high-precision analyses of extreme weather. *Geoscientific Model Development*, *14*(1), 107–124.

Kohonen, T., Schroeder, M. R., & Huang, T. S. (2001). *Self-organizing maps* (3rd). Springer-Verlag.

Kohonen, T. (1982a). Self-organized formation of topologically correct feature maps. *Biological cybernetics*, *43*(1), 59–69.

Kohonen, T. (1982b). A simple paradigm for the self-organized formation of structured feature maps. In *Competition and cooperation in neural nets* (pp. 248–266). Springer.

Leung, L. R., Bader, D. C., Taylor, M. A., & McCoy, R. B. (2020). An introduction to the e3sm special collection: Goals, science drivers, development, and analysis. *Journal of Advances in Modeling Earth Systems*, *12*(11), e2019MS001821.

Li, G., & Xie, S.-P. (2012). Origins of tropical-wide sst biases in cmip multi-model ensembles. *Geophysical research letters*, *39*(22).

Li, G., & Xie, S.-P. (2014). Tropical biases in cmip5 multimodel ensemble: The excessive equatorial pacific cold tongue and double itcz problems. *Journal of Climate*, *27*(4), 1765–1780.

Liu, W., Fedorov, A. V., Xie, S.-P., & Hu, S. (2020). Climate impacts of a weakened atlantic meridional overturning circulation in a warming climate. *Science advances*, *6*(26), eaaz4876.

Liu, X., Chang, P., Fu, D., Saravanan, R., Wang, H., Rosenbloom, N., Zhang, S., & Wu, L. (2022). Improved simulations of atmospheric river climatology and variability in high-resolution cesm. *Journal of Advances in Modeling Earth Systems*, *14*(9), e2022MS003081.

Liu, Y., & Weisberg, R. H. (2011). A review of self-organizing map applications in meteorology and oceanography. *Self-Organizing Maps: Applications and Novel Algorithm Design*, 253–272.

Lu, Y., Wu, T., Li, Y., & Yang, B. (2021). Mitigation of the double itcz syndrome in bcc-csm2-mr through improving parameterizations of boundary-layer turbulence and shallow convection. *Geoscientific Model Development*, *14*(8), 5183–5204.

Ma, X., Yu, F., & Luo, G. (2012). Aerosol direct radiative forcing based on geos-chem-apm and uncertainties. *Atmospheric Chemistry and Physics*, *12*(12), 5563–5581.

Michaelis, A. C., Gershunov, A., Weyant, A., Fish, M. A., Shulgina, T., & Ralph, F. M. (2022). Atmospheric river precipitation enhanced by climate change: A case study of

the storm that contributed to california's oroville dam crisis. *Earth's Future*, *10*(3), e2021EF002537.

Mundhenk, B. D., Barnes, E. A., & Maloney, E. D. (2016). All-season climatology and variability of atmospheric river frequencies over the north pacific. *Journal of Climate*, *29*(13), 4885–4903.

Neiman, P. J., Hughes, M., Moore, B. J., Ralph, F. M., & Sukovich, E. M. (2013). Sierra barrier jets, atmospheric rivers, and precipitation characteristics in northern california: A composite perspective based on a network of wind profilers. *Monthly Weather Review*, *141*(12), 4211–4233.

Neiman, P. J., Ralph, F. M., Moore, B. J., Hughes, M., Mahoney, K. M., Cordeira, J. M., & Dettinger, M. D. (2013). The landfall and inland penetration of a flood-producing atmospheric river in arizona. part i: Observed synoptic-scale, orographic, and hydrometeorological characteristics. *Journal of Hydrometeorology*, *14*(2), 460–484.

Neiman, P. J., Ralph, F. M., White, A., Kingsmill, D., & Persson, P. (2002). The statistical relationship between upslope flow and rainfall in california's coastal mountains: Observations during caljet. *Monthly Weather Review*, *130*(6), 1468–1492.

Neiman, P. J., Ralph, F. M., Wick, G. A., Lundquist, J. D., & Dettinger, M. D. (2008). Meteorological characteristics and overland precipitation impacts of atmospheric rivers affecting the west coast of north america based on eight years of ssm/i satellite observations. *Journal of Hydrometeorology*, *9*(1), 22–47.

Neiman, P. J., Schick, L. J., Ralph, F. M., Hughes, M., & Wick, G. A. (2011). Flooding in western washington: The connection to atmospheric rivers. *Journal of Hydrometeorology*, *12*(6), 1337–1358.

NOAA. (2020a). Climate indices ftp.

NOAA. (2020b). Climate prediction center (cpc) oceanic nino index.

NOAA. (2020c). Daily climate timeseries: Epo.

NOAA. (2020d). Daily climate timeseries: Wpo.

O'Brien, T. A., Payne, A. E., Shields, C. A., Rutz, J., Brands, S., Castellano, C., Chen, J., Cleveland, W., DeFlorio, M. J., Goldenson, N., et al. (2020). Detection uncertainty matters for understanding atmospheric rivers. *Bulletin of the American Meteorological Society*, *101*(6), E790–E796.

O'Brien, T. A., Wehner, M. F., Payne, A. E., Shields, C. A., Rutz, J. J., Leung, L.-R., Ralph, F. M., Collow, A., Gorodetskaya, I., Guan, B., et al. (2021). Increases in future ar count and size: Overview of the artmip tier 2 cmip5/6 experiment. *Journal of Geophysical Research: Atmospheres*, e2021JD036013.

Payne, A. E., Demory, M.-E., Leung, L. R., Ramos, A. M., Shields, C. A., Rutz, J. J., Siler, N., Villarini, G., Hall, A., & Ralph, F. M. (2020). Responses and impacts of atmospheric rivers to climate change. *Nature Reviews Earth & Environment*, 1–15.

Payne, A. E., & Magnusdottir, G. (2014). Dynamics of landfalling atmospheric rivers over the north pacific in 30 years of merra reanalysis. *Journal of Climate*, *27*(18), 7133–7150.

Payne, A. E., & Magnusdottir, G. (2015). An evaluation of atmospheric rivers over the north pacific in cmip5 and their response to warming under rcp 8.5. *Journal of Geophysical Research: Atmospheres*, *120*(21), 11–173.

Porter, K., Wein, A., Alpers, C. N., Baez, A., Barnard, P. L., Carter, J., Corsi, A., Costner, J., Cox, D., Das, T., et al. (2011). *Overview of the arkstorm scenario* (tech. rep.). US Geological Survey.

Radić, V., Cannon, A. J., Menounos, B., & Gi, N. (2015). Future changes in autumn atmospheric river events in british columbia, canada, as projected by cmip5 global climate models. *Journal of Geophysical Research: Atmospheres*, *120*(18), 9279–9302.

Ralph, F. M., Cannon, F., Tallapragada, V., Davis, C. A., Doyle, J. D., Pappenberger, F., Subramanian, A., Wilson, A. M., Lavers, D. A., Reynolds, C. A., et al. (2020). West coast forecast challenges and development of atmospheric river reconnaissance. *Bulletin of the American Meteorological Society*, *101*(8), E1357–E1377.

Ralph, F. M., Dettinger, M., Lavers, D., Gorodetskaya, I. V., Martin, A., Viale, M., White, A. B., Oakley, N., Rutz, J., Spackman, J. R., et al. (2017). Atmospheric rivers emerge as a global science and applications focus. *Bulletin of the American Meteorological Society*, *98*(9), 1969–1973.

Ralph, F. M., Dettinger, M. D., Cairns, M. M., Galarneau, T. J., & Eylander, J. (2018). Defining "atmospheric river": How the glossary of meteorology helped resolve a debate. *Bulletin of the American Meteorological Society*, *99*(4), 837–839.

Ralph, F. M., Dettinger, M. D., Rutz, J. J., & Waliser, D. E. (2020a). *Atmospheric rivers* (Vol. 1). Springer.

Ralph, F. M., Dettinger, M. D., Rutz, J. J., & Waliser, D. E. (2020b). *Atmospheric rivers* (Vol. 1). Springer.

Ralph, F. M., Iacobellis, S., Neiman, P., Cordeira, J., Spackman, J., Waliser, D., Wick, G., White, A., & Fairall, C. (2017). Dropsonde observations of total integrated water vapor transport within north pacific atmospheric rivers. *Journal of Hydrometeorology*, *18*(9), 2577–2596.

Ralph, F. M., Neiman, P. J., & Rotunno, R. (2005). Dropsonde observations in low-level jets over the northeastern pacific ocean from caljet-1998 and pacjet-2001: Mean vertical-profile and atmospheric-river characteristics. *Monthly weather review*, *133*(4), 889–910.

Ralph, F. M., Neiman, P. J., & Wick, G. A. (2004). Satellite and caljet aircraft observations of atmospheric rivers over the eastern north pacific ocean during the winter of 1997/98. *Monthly Weather Review*, *132*(7), 1721–1745.

Ralph, F. M., Neiman, P. J., Wick, G. A., Gutman, S. I., Dettinger, M. D., Cayan, D. R., & White, A. B. (2006). Flooding on california's russian river: Role of atmospheric rivers. *Geophysical Research Letters*, *33*(13).

Ralph, F. M., Prather, K., Cayan, D., Spackman, J., DeMott, P., Dettinger, M., Fairall, C., Leung, R., Rosenfeld, D., Rutledge, S., et al. (2016). Calwater field studies designed to quantify the roles of atmospheric rivers and aerosols in modulating us west coast

precipitation in a changing climate. *Bulletin of the American Meteorological Society*, *97*(7), 1209–1228.

Ralph, F. M., Rutz, J. J., Cordeira, J. M., Dettinger, M., Anderson, M., Reynolds, D., Schick, L. J., & Smallcomb, C. (2019). A scale to characterize the strength and impacts of atmospheric rivers. *Bulletin of the American Meteorological Society*, *100*(2), 269–289.

Ralph, F., Coleman, T., Neiman, P., Zamora, R., & Dettinger, M. (2013). Observed impacts of duration and seasonality of atmospheric-river landfalls on soil moisture and runoff in coastal northern california. *Journal of Hydrometeorology*, *14*(2), 443–459.

Ralph, F., & Dettinger, M. (2011). Storms, floods, and the science of atmospheric rivers. *Eos, Transactions American Geophysical Union*, *92*(32), 265–266.

Ralph, F., & Dettinger, M. (2012). Historical and national perspectives on extreme west coast precipitation associated with atmospheric rivers during december 2010. *Bulletin of the American Meteorological Society*, *93*(6), 783–790.

Ralph, F., Wick, G., Neiman, P., Moore, B., Spackman, J., Hughes, M., Yong, F., & Hock, T. (2012). Atmospheric rivers in reanalysis products: A six-event comparison with aircraft observations of water vapor transport. *Extended abstracts, wcrp reanalysis conf., silver spring, md.*

Rasch, P., Xie, S., Ma, P.-L., Lin, W., Wang, H., Tang, Q., Burrows, S., Caldwell, P., Zhang, K., Easter, R., et al. (2019). An overview of the atmospheric component of the energy exascale earth system model. *Journal of Advances in Modeling Earth Systems*, *11*(8), 2377–2411.

Rhoades, A. M., Risser, M. D., Stone, D. A., Wehner, M. F., & Jones, A. D. (2021). Implications of warming on western united states landfalling atmospheric rivers and their flood damages. *Weather and Climate Extremes*, *32*, 100326.

Rivière, G. (2010). Role of rossby wave breaking in the west pacific teleconnection. *Geophysical research letters*, *37*(11).

Rutz, J. J., Shields, C. A., Lora, J. M., Payne, A. E., Guan, B., Ullrich, P., O'Brien, T., Leung, L. R., Ralph, F. M., Wehner, M., et al. (2019). The atmospheric river tracking method intercomparison project (artmip): Quantifying uncertainties in atmospheric river climatology. *Journal of Geophysical Research: Atmospheres*.

Rutz, J. J., Steenburgh, W. J., & Ralph, F. M. (2014). Climatological characteristics of atmospheric rivers and their inland penetration over the western united states. *Monthly Weather Review*, *142*(2), 905–921.

Ryoo, J.-M., Kaspi, Y., Waugh, D. W., Kiladis, G. N., Waliser, D. E., Fetzer, E. J., & Kim, J. (2013). Impact of rossby wave breaking on us west coast winter precipitation during enso events. *Journal of Climate*, *26*(17), 6360–6382.

Ryoo, J.-M., Waliser, D. E., Waugh, D. W., Wong, S., Fetzer, E. J., & Fung, I. (2015). Classification of atmospheric river events on the us west coast using a trajectory model. *Journal of Geophysical Research: Atmospheres*, *120*(8), 3007–3028.

Schlef, K. E., Moradkhani, H., & Lall, U. (2019). Atmospheric circulation patterns associated with extreme united states floods identified via machine learning. *Scientific reports*, *9*(1), 1–12.

Sellars, S., Kawzenuk, B., Nguyen, P., Ralph, F., & Sorooshian, S. (2017). Genesis, pathways, and terminations of intense global water vapor transport in association with large-scale climate patterns. *Geophysical Research Letters*, *44*(24), 12–465.

Sheridan, S. C., & Lee, C. C. (2011). The self-organizing map in synoptic climatological research. *Progress in Physical Geography*, *35*(1), 109–119.

Shields, C. A., Rutz, J. J., Leung, L.-Y., Ralph, F. M., Wehner, M., Kawzenuk, B., Lora, J. M., McClenny, E., Osborne, T., Payne, A. E., Ullrich, P., Gershunov, A., Goldenson, N., Guan, B., Qian, Y., Ramos, A. M., Sarangi, C., Sellars, S., Gorodetskaya, I., . . . Nguyen, P. (2018a). Atmospheric river tracking method intercomparison project (artmip): Project goals and experimental design. *Geoscientific Model Development Discussions*, *2018*, 1–55. https://doi.org/10.5194/gmd-2017-295

Shields, C. A., Rutz, J. J., Leung, L.-Y., Ralph, F. M., Wehner, M., Kawzenuk, B., Lora, J. M., McClenny, E., Osborne, T., Payne, A. E., Ullrich, P., Gershunov, A., Goldenson, N., Guan, B., Qian, Y., Ramos, A. M., Sarangi, C., Sellars, S., Gorodetskaya, I., . . . Nguyen, P. (2018b). Atmospheric river tracking method intercomparison project (ARTMIP): Project goals and experimental design. *Geoscientific Model Development*, *11*(6), 2455–2474. https://doi.org/10.5194/gmd-11-2455-2018

Shields, C. A., & Kiehl, J. T. (2016). Atmospheric river landfall-latitude changes in future climate simulations. *Geophysical Research Letters*, *43*(16), 8775–8782.

Shields, C. A., Payne, A. E., Shearer, E. J., Wehner, M. F., O'Brien, T. A., Rutz, J. J., Leung, L. R., Ralph, F. M., Marquardt Collow, A. B., Ullrich, P. A., et al. (2023). Future atmospheric rivers and impacts on precipitation: Overview of the artmip tier 2 high-resolution global warming experiment. *Geophysical Research Letters*, *50*(6), e2022GL102091.

Shields, C. A., Rutz, J. J., Leung, L. R., Ralph, F. M., Wehner, M., O'Brien, T., & Pierce, R. (2019). Defining uncertainties through comparison of atmospheric river tracking methods. *Bulletin of the American Meteorological Society*, *100*(2), ES93–ES96.

Siler, N., & Roe, G. (2014). How will orographic precipitation respond to surface warming? an idealized thermodynamic perspective. *Geophysical Research Letters*, *41*(7), 2606–2613.

Skific, N., & Francis, J. (2012). Self-organizing maps: A powerful tool for the atmospheric sciences. *Applications of Self-Organizing Maps*, 251–268.

Smith, B. L., Yuter, S. E., Neiman, P. J., & Kingsmill, D. (2010). Water vapor fluxes and orographic precipitation over northern california associated with a landfalling atmospheric river. *Monthly weather review*, *138*(1), 74–100.

Song, X., & Zhang, G. J. (2018). The roles of convection parameterization in the formation of double itcz syndrome in the ncar cesm: I. atmospheric processes. *Journal of Advances in Modeling Earth Systems*, *10*(3), 842–866.

Swain, D. L., Langenbrunner, B., Neelin, J. D., & Hall, A. (2018). Increasing precipitation volatility in twenty-first-century california. *Nature Climate Change*, *8*(5), 427–433.

Swales, D., Alexander, M., & Hughes, M. (2016). Examining moisture pathways and extreme precipitation in the us intermountain west using self-organizing maps. *Geophysical Research Letters*, *43*(4), 1727–1735.

UCAR. (2020). North pacific (np) index.

Vettigli, G. (2020). Minisom [[Online; accessed 26-March-2020]].

Wahl, E. R., Zorita, E., Trouet, V., & Taylor, A. H. (2019). Jet stream dynamics, hydroclimate, and fire in california from 1600 ce to present. *Proceedings of the National Academy of Sciences*, *116*(12), 5393–5398.

Waliser, D., & Guan, B. (2017). Extreme winds and precipitation during landfall of atmospheric rivers. *Nature Geoscience*, *10*(3), 179–183.

Wang, S., Ma, X., Zhou, S., Wu, L., Wang, H., Tang, Z., Xu, G., Jing, Z., Chen, Z., & Gan, B. (2023). Extreme atmospheric rivers in a warming climate. *Nature Communications*, *14*(1), 3219.

Warner, M. D., Mass, C. F., & Salathe Jr, E. P. (2015). Changes in winter atmospheric rivers along the north american west coast in cmip5 climate models. *Journal of Hydrometeorology*, *16*(1), 118–128.

Wing, I. S., Rose, A. Z., & Wein, A. M. (2016). Economic consequence analysis of the arkstorm scenario. *Natural Hazards Review*, *17*(4), A4015002.

Zhang, G. J., Song, X., & Wang, Y. (2019). The double itcz syndrome in gcms: A coupled feedback problem among convection, clouds, atmospheric and ocean circulations. *Atmospheric Research*, *229*, 255–268.

Zhang, W., & Villarini, G. (2018). Uncovering the role of the east asian jet stream and heterogeneities in atmospheric rivers affecting the western united states. *Proceedings of the National Academy of Sciences*, *115*(5), 891–896.

Zhang, X., Lin, W., & Zhang, M. (2007). Toward understanding the double intertropical convergence zone pathology in coupled ocean-atmosphere general circulation models. *Journal of Geophysical Research: Atmospheres*, *112*(D12).

Zhou, Y., & Kim, H. (2019). Impact of distinct origin locations on the life cycles of landfalling atmospheric rivers over the us west coast. *Journal of Geophysical Research: Atmospheres*, *124*(22), 11897–11909.

Zhou, Y., Kim, H., & Guan, B. (2018). Life cycle of atmospheric rivers: Identification and climatological characteristics. *Journal of Geophysical Research: Atmospheres*, *123*(22), 12–715.

Zhu, Y., & Newell, R. E. (1998). A proposed algorithm for moisture fluxes from atmospheric rivers. *Monthly weather review*, *126*(3), 725–735.

Appendix A

Appendix to Chapter 2

A.1 SOM description and parameters

We briefly outline how a SOM is trained iteratively: Each node is a vector containing weights for each grid in our spatial domain. We randomly initialize each node in the SOM by randomly sampling from our data. We then begin randomly sampling geopotential height anomaly data and determine the node that has the minimum Euclidean distance from this sample. Adjust this minimum distance node, or the 'winning' node, to more closely match the sample (depends on learning rate). In addition, adjust the neighbors of the winning node (depends on learning rate and neighborhood radius and function). Choose the next random sample and repeat.

For this study a SOM of order 3x3 (9 total nodes) is trained on AR genesis day samples. We use standardized geopotential height anomalies at 500mb as our variable of interest and weight the grid points by grid cell area. The SOM order of 3x3 was chosen over other configurations as the smaller size is easier to interpret, the corners are consistent when using larger orders, and the quality of the map is not significantly reduced. The SOM is implemented with python based software called MiniSom (Vettigli, 2020). The node vectors are randomly initialized as it has been shown to perform best for non-linear datasets (Akinduko et al., 2016). We perform training in two rounds as suggested in Hewitson and Crane, 2002, Gibson et al., 2017, and Jiang et al., 2015. Gibson et al., 2017 and Jiang et al., 2015 found that reducing the radius so that only the winning node is updated (which is equivalent to k-means (Bação et al., 2005)) for the 2nd round of training produced more realistic and distinct synoptic patterns although topological ordering can become reduced. The first round is the ordering phase with a large neighborhood radius and learning rate which allows the map's structure to develop. The second round is the convergent phase with a smaller radius and learning rate where the finer details can develop. During the first phase, the initial neighborhood radius and learning rate decay exponentially and run through 51350 (50x the sample size of 1027 ARs) iterations total. The second phase holds the radius constant so only the winning node will be updated. The learning rate also decays in this

second phase and runs through 51350 iterations. The decay function used in MiniSom is:

$$val\_t = \frac{val\_0}{1 + \frac{t}{\left(\frac{max\_iter}{2}\right)}}, \tag{A.1}$$

where val_t is the value of the neighborhood radius or learning rate at iteration t, val_0 is either the initial radius or learning rate, t is the current iteration, and max_iter is the total number of iterations in a training phase. We use an initial radius of 2 (1) and a learning rate of 0.1 (0.05) during the ordering phase (convergent phase). After training the SOM, each AR event is classified into one of the nine nodes based on best match as determined by Euclidean distance of gridded features between genesis day and SOM node; this winning node is sometimes referred to as the "best matching unit" (BMU). We then create composites for each node based on all of the genesis days of the AR events associated with that node.

A.2   Differences in GW19

Here we discuss differences between the SOMs trained on the Gonzalez and GW19 AR catalogues. Nodes 3, 5, and 7 show the most significant differences. Node 3's synoptic conditions in the Gonzalez SOM supports moisture transport along a poleward tilted jet with a coastal low anomaly bringing moisture to the US west coast. In contrast, node 3's synoptic conditions in the GW19 SOM are more favorable for moisture transport to Canada in particular but also to the California Baja Peninsula and features a slightly less eastward extended jet (Fig. A.8 and Fig. A.6). While both feature high pressure anomalies throughout the north Pacific basin, for ARs to make landfall in on the US west coast, the high pressure anomaly in the eastern Pacific needs to remain at lower latitudes else the moisture will be transported north of the US western states. Because the high pressure in the GW19 SOM reaches higher latitudes near Alaska, the positive EPO mean in the Gonzalez SOM for node 3 turns to a negative mean for EPO. It is one of 3 node and climate index pairs in all of the nodes and indices considered that changes phase (the NP (AO) node 2 (node 5) is slightly positive (negative) with the Gonzalez data and becomes slightly negative (positive) in GW19).

For node 5, the Gonzalez synoptic conditions, in particular, favor a more eastward extended jet due to the low geopotential height anomaly in the central north Pacific compared to the high anomaly in the GW19 synoptic conditions.

The GW19 node 7 synoptic conditions favor moisture transport to Canada as opposed to the Gonzalez synoptic conditions which favor transport to Oregon and Washington (seen most clearly in the lower level winds shown in Fig. A.7 and Fig. A.8). Both feature a low geopotential height anomaly in the central north Pacific but have differing locations for the high latitude ridge - the GW19 positive height anomalies are over the Pacific northwest while the Gonzalez height anomalies are stronger and over Siberia and Alaska.

As for differences in lifecycle characteristics, in the GW19 SOM, the positive ENSO node (Node 1) has, on average, AR genesis occurring >10 degrees more east, longer AR durations,

travel farther distances, faster velocities, and the most stark contrast in the ratio between zonal and meridional displacement throughout the AR lifecycle compared to the negative ENSO node (Node 9). These characteristics are consistent with the Gonzalez dataset. As for the jet modes, both genesis latitude and average latitude are further north for the positive node (Node 3) compared to the negative node (Node 7) which is also consistent with the Gonzalez dataset. The negative mode is also exhibits more meridional displacement although this difference between positive and negative jet nodes is much smaller with GW19.
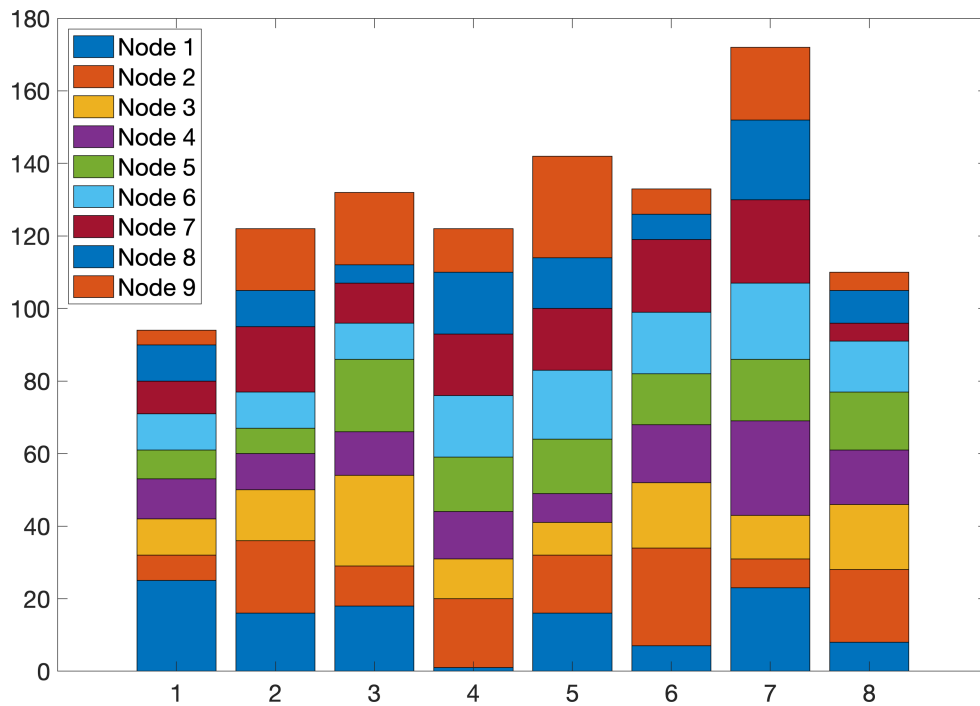
Figure A.1: MJO phase frequency distributions per node. Bars represent how often genesis day samples assigned to each node occurred during MJO phases 1-8.
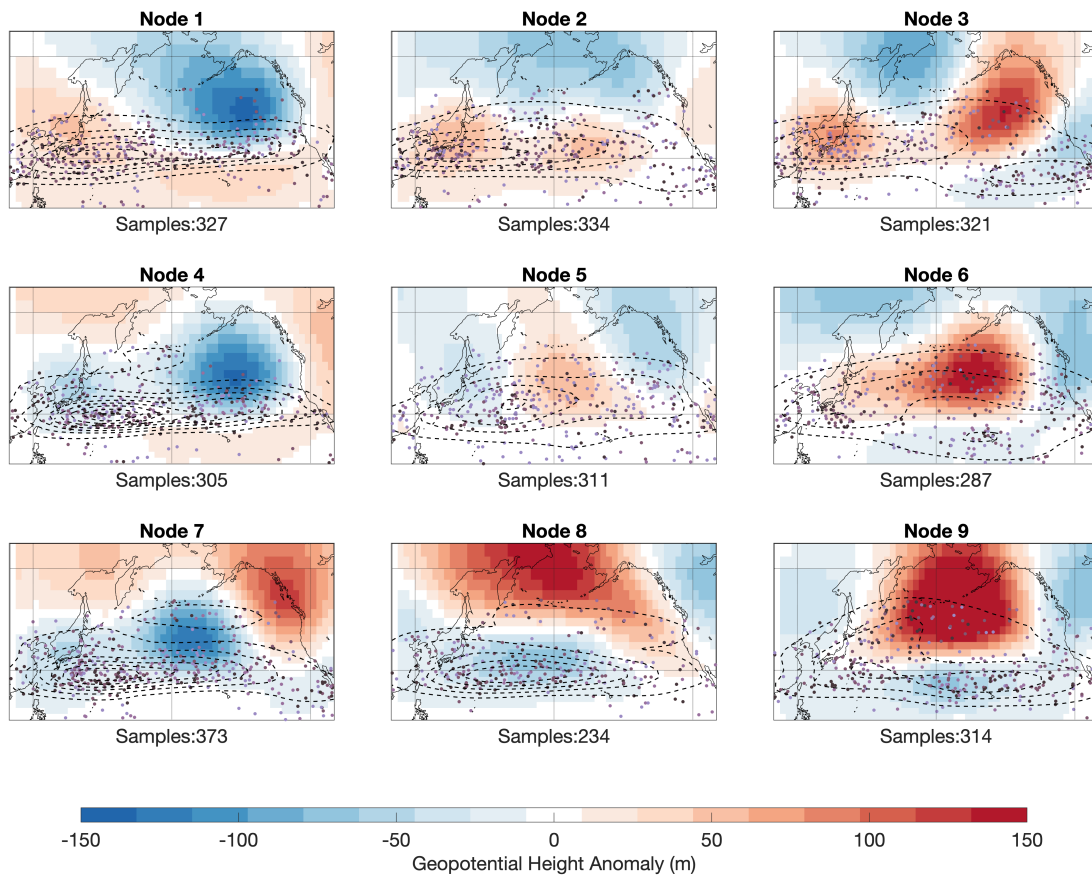
Figure A.2: Same as in Fig. 2.2 but trained on the Guan and Waliser catalogue which contains all ARs (landfalling and non-landfalling) in the north Pacific. Termination points and tracks are excluded. Instead, probability density estimate contours of genesis points are included. Contours levels are at 0.00015.
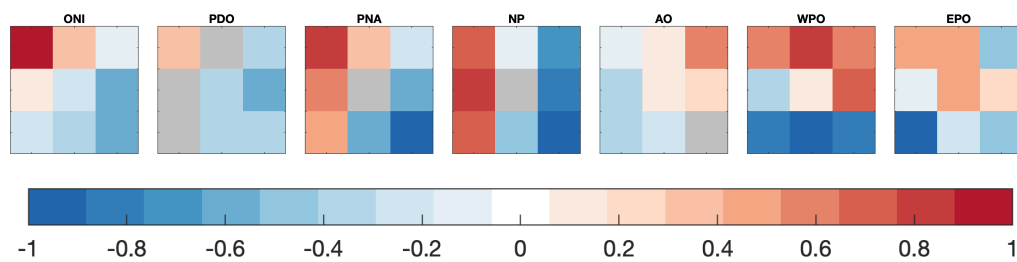

Figure A.3: Same as in Fig. 2.3 but corresponding with the SOM in Fig. A.2.

Node #	Genesis	Landfall	Dur(hr)	Dist(km)	Vel(km/hr)	Lat	Lon	Merid	Zonal	Aspect
1	31.6N,171.2E	NA	69.4	4852	69.9	35.9N	194.3E	8.7	36.4	4.2
2	32.5N,175.2E	NA	69.4	4689	67.6	38.1N	196.5E	9.6	35.2	3.7
3	31.4N,177.4E	NA	69.3	4680	67.5	38.1N	199.3E	10.5	26.6	2.5
4	31.2N,173.3E	NA	69.8	4812	69.0	35.8N	196.4E	9.2	32.9	3.6
5	31.9N,181.4E	NA	62.2	4188	67.3	38.1N	199.3E	8.4	28.4	3.4
6	32.1N,181.7E	NA	59.3	3927	66.2	37.5N	196.9E	7.4	22.4	3.0
7	30.4N,175.6E	NA	70.7	5008	70.8	36.2N	196.0E	11.1	31.8	2.8
8	32.0N,174.6E	NA	69.4	4515	65.1	36.9N	196.6E	10.4	28.7	2.8
9	31.6N,182.0E	NA	62.0	3889	62.7	37.6N	197.7E	9.5	14.3	1.5

Table A.1: Summary of various AR characteristics associated with each node of the SOM.
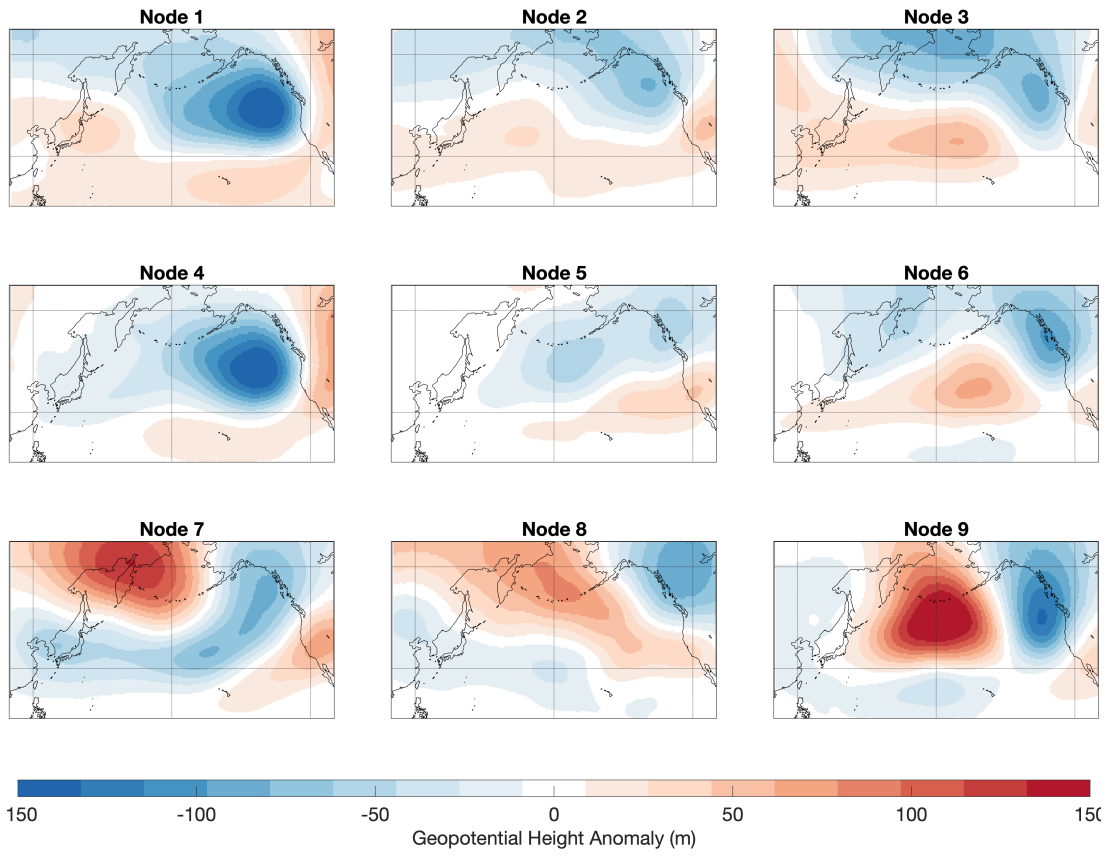
Figure A.4: Landfalling 500 hPa geopotential height anomalies.
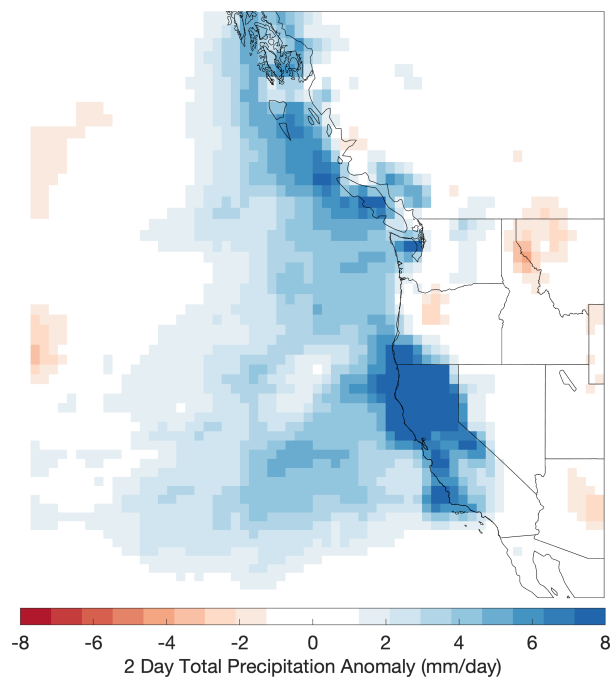
Figure A.5: Landfall precipitation anomaly differences for the most El Niño node (Node 1) and the most La Niña node (Node 6).
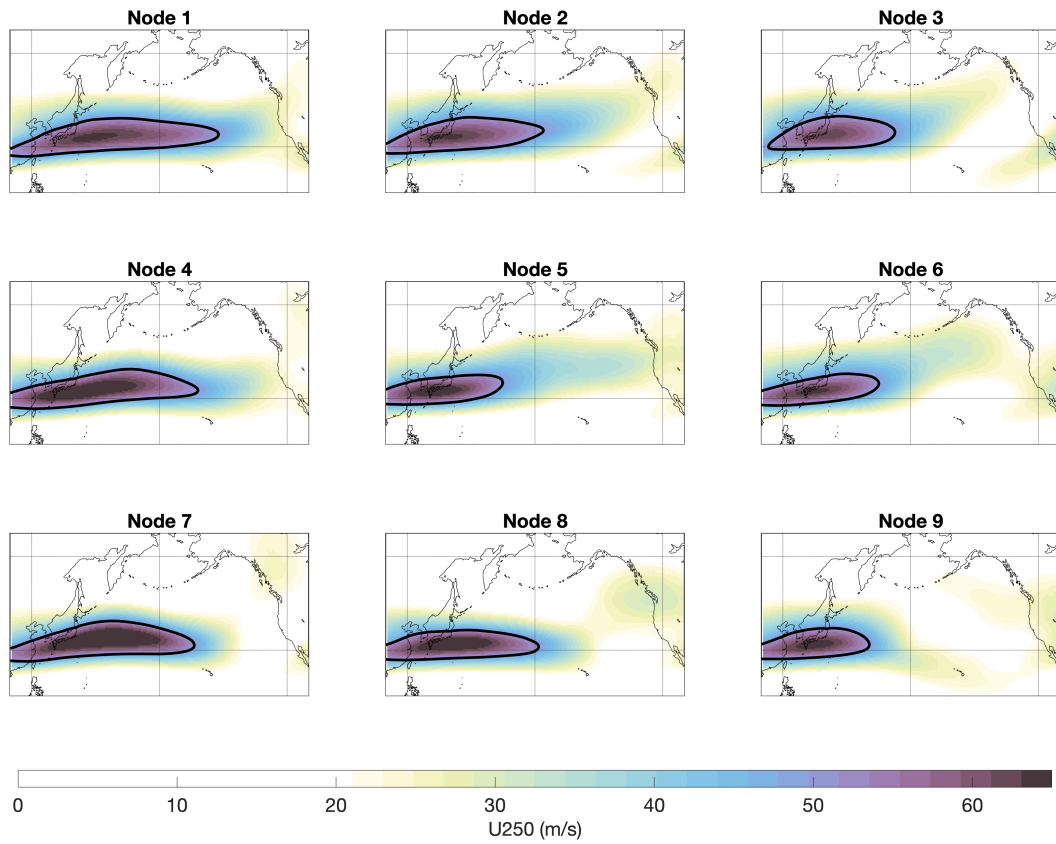
Figure A.6: Composites of the 250 hPa zonal wind on genesis day for the GW19 dataset.
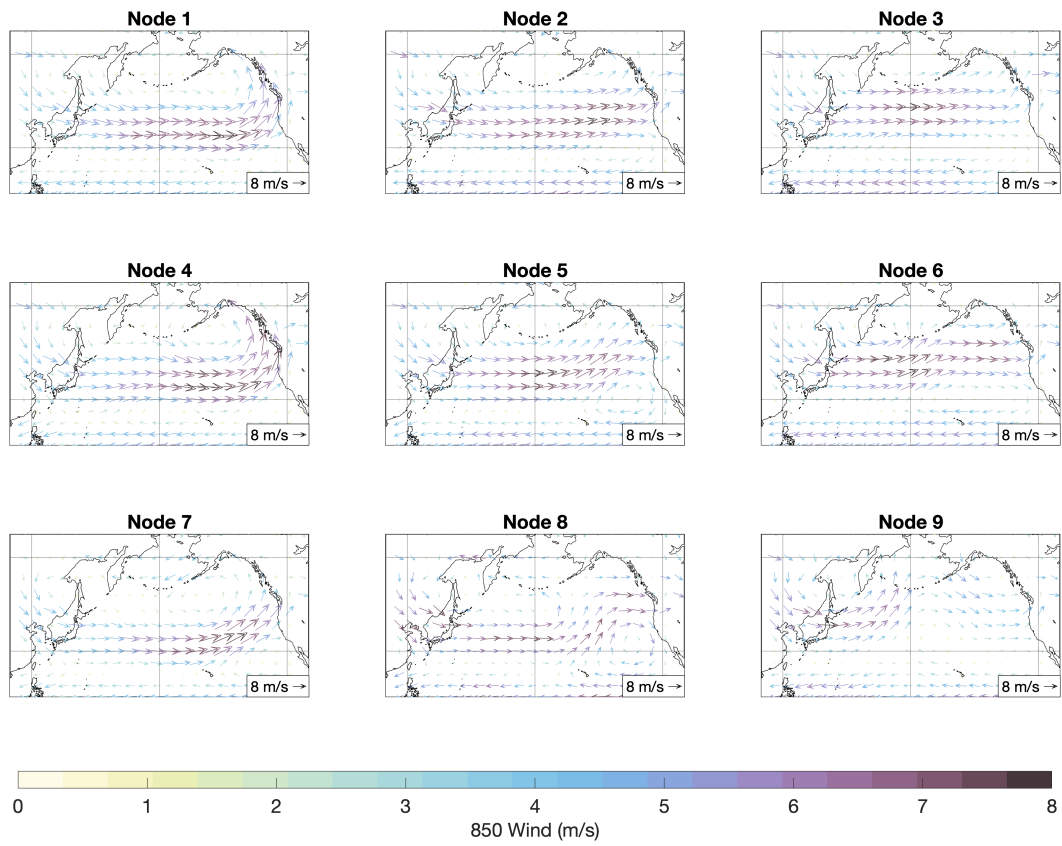
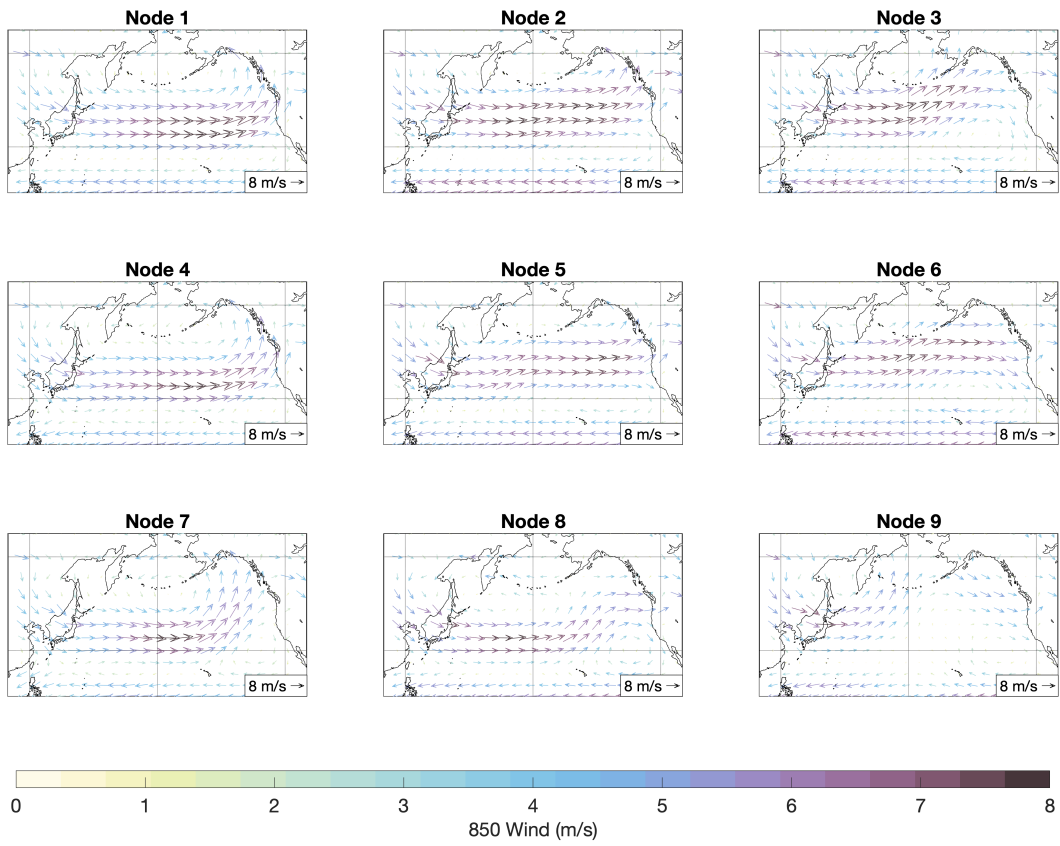Figure A.7: Composites of the 850 hPa wind on genesis day (not anomalies).

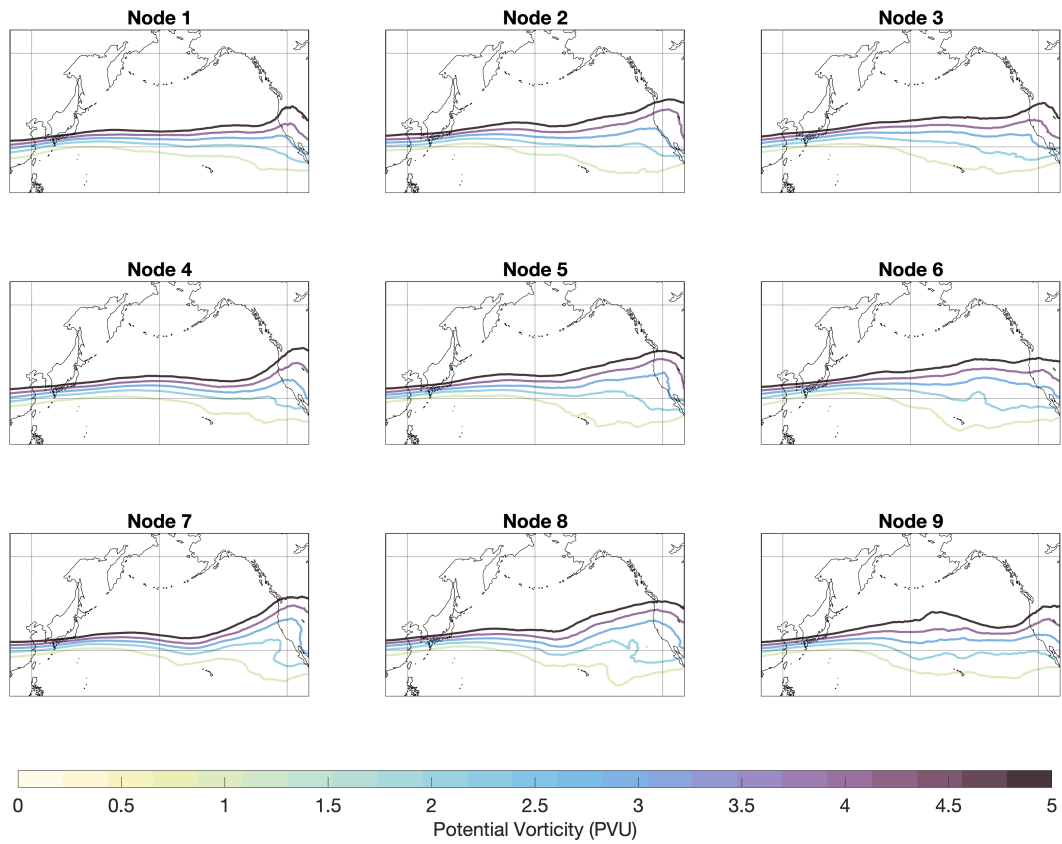Figure A.8: Same as Fig. A.7 but for the GW19 dataset.

Figure A.9: PV200 composites on AR landfall day.
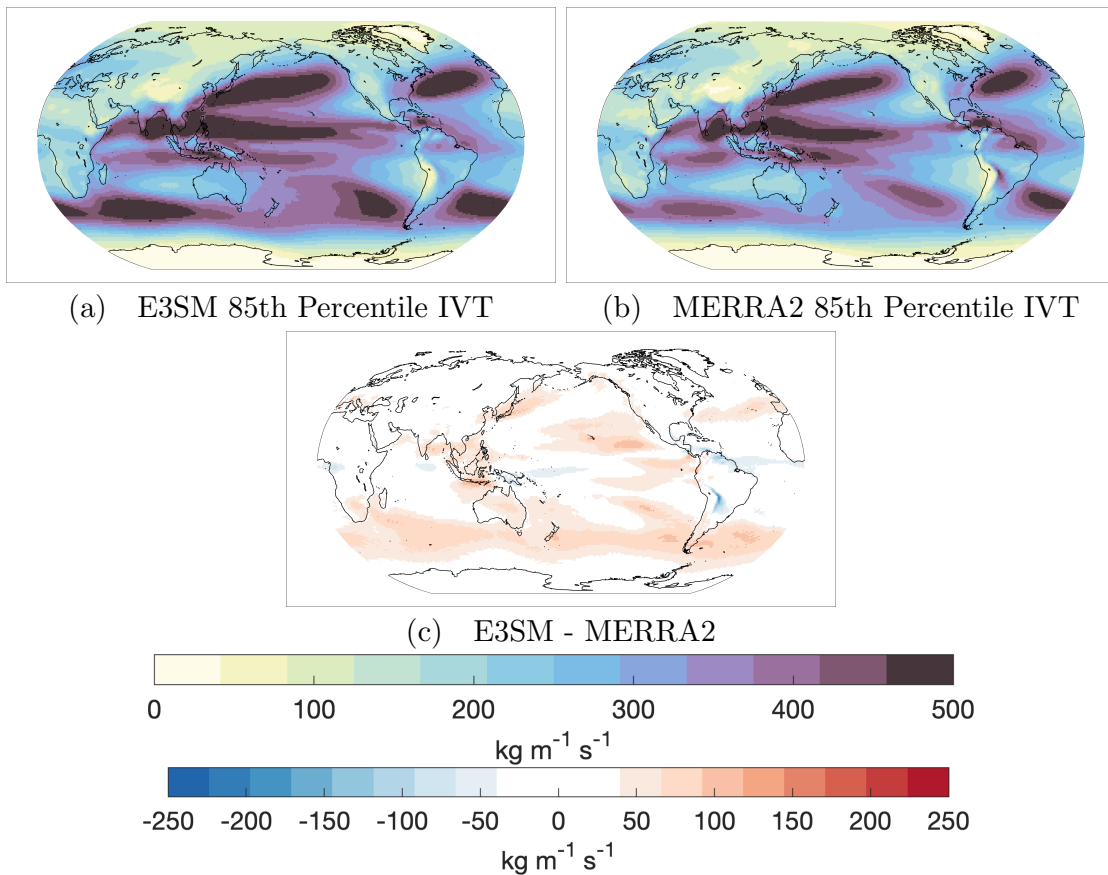
Appendix B

Appendix to Chapter 3

(a)   E3SM 85th Percentile IVT   (b)   MERRA2 85th Percentile IVT

(c)   E3SM - MERRA2

Figure B.1: Annual mean 85th percentile IVT for (a) E3SM and (b) MERRA2. The difference (E3SM minus MERRA2) is shown in (c).
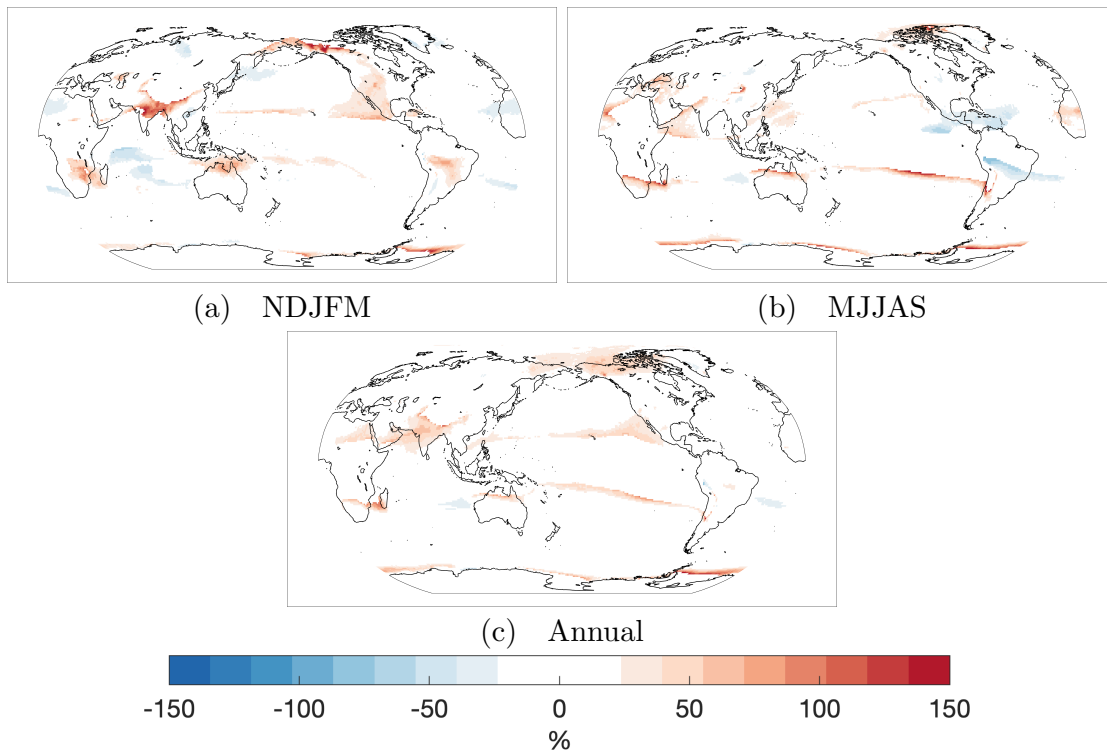
(a) NDJFM (b) MJJAS

(c) Annual

Figure B.2: AR relative frequency differences (as opposed to absolute frequency differences) by percentage corresponding with Fig. 3.1c, f, and i. Only gridpoints with MERRA2 AR frequencies (absolute) of at least 3% are shown (regions with very low AR frequencies can show relative differences of 100% due to a single extra timestep).
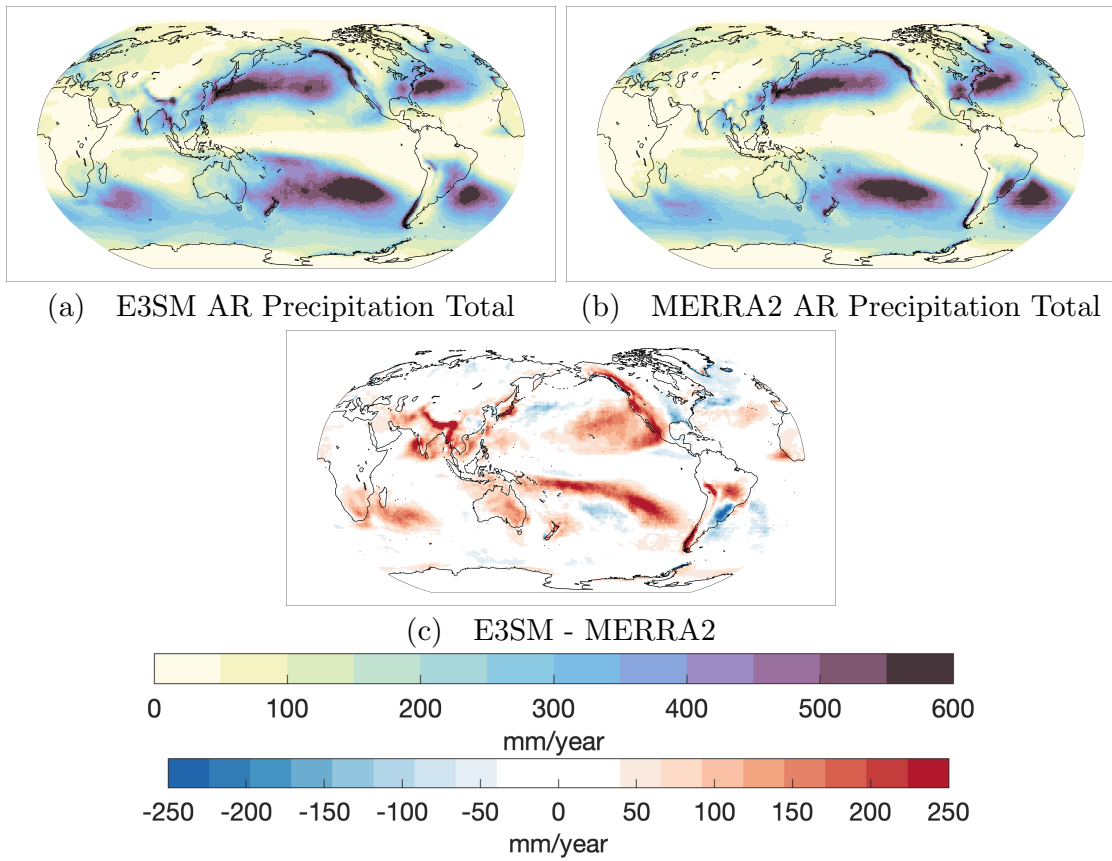
Figure B.3: Mean annual total AR precipitation for (a) E3SM and (b) MERRA2. The difference is shown in (c).
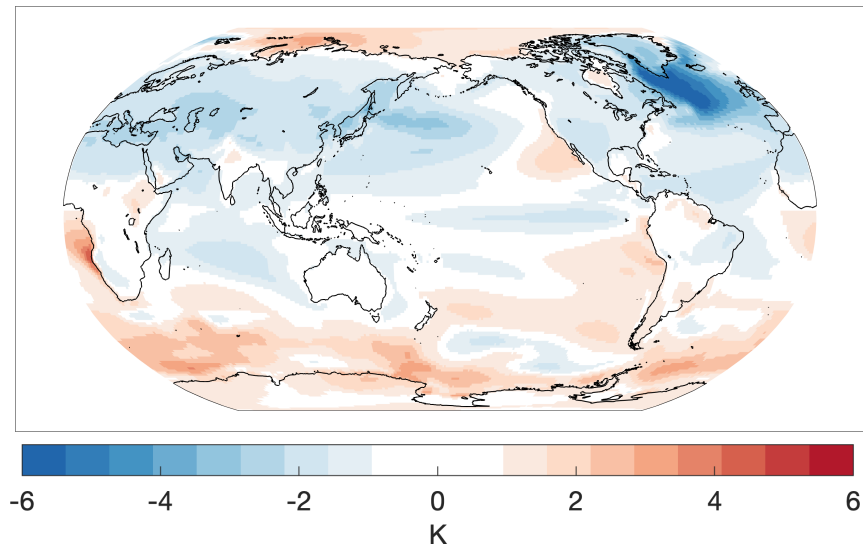
Figure B.4: Annual surface temperature differences between the fully-coupled E3SM simulation and the AMIP E3SM simulation.